2002

Experimental and analytical studies of a CO2 laser-based flexible fabrication method for dies and molds

Wenping Jiang
Iowa State University

INFORMATION TO USERS

This manuscript has been reproduced from the microfilm master. UMI films the text directly from the original or copy submitted. Thus, some thesis and dissertation copies are in typewriter face, while others may be from any type of computer printer.

The quality of this reproduction is dependent upon the quality of the copy submitted. Broken or indistinct print, colored or poor quality illustrations and photographs, print bleedthrough, substandard margins, and improper alignment can adversely affect reproduction.

In the unlikely event that the author did not send UMI a complete manuscript and there are missing pages, these will be noted. Also, if unauthorized copyright material had to be removed, a note will indicate the deletion.

Oversize materials (e.g., maps, drawings, charts) are reproduced by sectioning the original, beginning at the upper left-hand corner and continuing from left to right in equal sections with small overlaps.

ProQuest Information and Learning
300 North Zeeb Road, Ann Arbor, MI 48106-1346 USA
800-521-0600

Experimental and analytical studies of a CO_2 laser-based flexible fabrication method for dies and molds

by

Wenping Jiang

A dissertation submitted to the graduate faculty

in partial fulfillment of the requirements for the degree of

DOCTOR OF PHILOSOPHY

Major: Mechanical Engineering

Program of Study Committee:
Palaniappa A. Molian (Major Professor)
Daniel Bullen
Abhijit Chandra
Ranga Narayanaswami
Frank Peters

Iowa State University

Ames, Iowa

2002

UMI Number: 3061838

UMI Microform 3061838

ProQuest Information and Learning Company
300 North Zeeb Road
P.O. Box 1346
Ann Arbor, MI 48106-1346

Graduate College

Iowa State University

This is to certify that the doctoral dissertation of

Wenping Jiang

has met the dissertation requirements of Iowa State University

Signature was redacted for privacy.

Major Professor

Signature was redacted for privacy.

For the Major Program

To my wife, Hong Qin, and my son, Kyle S. Jiang

TABLE OF CONTENTS

LIST OF FIGURES

LIST OF TABLES

ACKNOWLEDGEMENTS

I would like to express my thanks to my major professor, Dr. Molian, for his unstinting help and support during my Ph.D. study. He has been an example of integrity, patience, and straight talk that I hope to live up to. I would also like to thank Dr. Bullen, Dr. Chandra, Dr. Peters, and Dr. Ranga for accepting to serve on my committee, and providing advices for the successful completion of my dissertation.

My special thoughts of gratitude go to my parents-in-law for their devotions in taking care of my baby and their encouragement. My gratitude also goes to my parents and my sister. Their hopes and aspirations helped me set my goals higher than I would have ever done. I would also like to thank the various technicians and researchers who helped me with my research at various points. Special thanks to Larry Couture for his input in my research and assistance in providing materials and post-processing, to Jim Dautremont and Chris Lassen for their assistance in troubleshooting problems with the various equipment in the research laboratory, and to Mr. Straszheim for his assistance in helping me with my SEM work.

ABSTRACT

Laser-based flexible fabrication (LBFF), a solid freeform fabrication (SFF) method based on laser-cladding process, was developed as an alternative to conventional machining methods for producing dies and molds. LBFF is similar to processes such as LENS with additional features including shaped beam profile, quasi-coaxial powder delivery, and functionally graded materials. It uses a high-power continuous wave (CW) CO_2 laser to fabricate functional tooling, dies and molds, of low surface roughness and high dimensional uniformity. It offers flexibility in designing parts with tailored materials, and in producing parts of complicated geometry.

Functionally graded molds of TiC/Ni-alloy and TiC/Ni-alloy/H13, and functional dies of H13 steel were built up by use of LBFF. Test studies on mold relief ability, strength, and dimensional stability at elevated temperatures were conducted and compared with bench mark H13 mold in gravity casting, in injection molding, and in thermal fatigue environment, respectively. Dies were also tested in aluminum extrusion under laboratory conditions. Results showed that dies and molds fabricated by LBFF had nearly full density, smooth surface ($R_a < 25$ μm), and improved performance; the functionally graded molds had gradual change in elemental compositions in the transitional regions between distinct layers. In addition to experiments, analytical and finite element modeling of temperature distributions was performed to justify the use of shaped beam profiles in LBFF.

CHAPTER 1. INTRODUCTION

The purpose of this systematic research is to investigate a CO_2 laser-based flexible fabrication (LBFF) technology for processing functionally graded molds and dies. Dies and molds find extensive uses in manufacturing processes such as injection molding, die-casting, stamping, extrusion and forging. Dies and molds are made of alloy steels such as H-13 (hot work tool steel, chromium type) and P20 (mold steel, chromium type), which exhibit high hardness (40~60 HRC) and toughness. Consequently, fabrication of dies and molds, achieved by CNC milling and electrical discharge machining (EDM), is a slow process accompanied by significant tooling costs and substantial material waste. Solid freeform fabrication (SFF) has been proven as a cost-effective technology in low volume tooling industry. In contrast to conventional subtractive machining, SFF is flexible to fabricate physical models of complicated geometry, with little or no material wastage. The versatility of laser cladding is pushing this technology further close to functional parts or components.

This body of investigation with the central theme of a CO_2 laser-based flexible fabrication (LBFF) of functionally graded molds and dies includes four sections: 1) development of an innovative laser-assisted coating process for extending service life of metal casting dies; 2) design of powder delivery system, and experimental investigations of LBFF processing technology for fabricating rectangular and circular dies and molds with functionally graded composition and microstructures, and of evaluation techniques for characterizing and testing these components; 3) computation of processing parameters for H13 powder deposition using an energy balance model, and production of extrusion dies by use of the obtained parameters and a designed quasi-axial nozzle; and 4) formulation of an analytical model in determination of nominal dimensions of molten pool of a moving laser

beam, and simulation of surface thermal gradients of circular and shaped beam profiles to justify the application of shaped beam in the deposition of TiC. The general findings of this study infer that LBFF, though there is still room for further improvement in surface finish, is superb in producing fully dense, functional parts in creating flexible tool geometry.

Dissertation organization

The dissertation is organized into seven chapters and three appendices. Chapter 1 (this chapter) states the objectives of the research and provides a brief summary of the studies that are presented in latter chapters. Chapter 2 provides background information on the previous research and recent development of solid freeform fabrication, lasers for rapid prototyping, dies and molds, and functionally graded materials. Chapter 3, a paper published in Surface and Coating Technology, reports the experimental investigations of an innovative laser coating process for extending lifetime of dies and molds using surface roughness and defects as justification criteria. In this paper, a review of the die failure modes, die material requirement, previous studies on surface coating processes, effect of laser glazing, laser surface alloying with micro- and nano-sized TiC powder, and tempering on hardness, corrosion and erosion resistance of H13 steel are discussed. Test results on corrosion/erosion resistance of processed samples in a simulating environment of aluminum casting are presented. Chapter 4, a paper to be published in the International Journal of Advanced Manufacturing Technology, reviews the current status of die and mold making processes, and laser-cladding based solid freeform fabrication technology. It presents experimental studies of LBFF processing technology for producing functionally graded molds and dies of rectangular and circular shapes using TiC powder and Ni/Cr alloy powder, and of mechanical

property evaluation techniques for testing the functional components. Chapter 5, a paper to be published in North America Manufacturing Conference (2002), deals with the production of circular extrusion dies in micro-scale H13 powder using LBFF with a designed quasi-axial nozzle for powder delivery. The processing parameters are computed by use of a lumped heat capacity model based on heat balance. The fabricated parts are evaluated using laboratory aluminum extrusion practice. Chapter 6, a paper to be submitted to ASME Journal of Manufacturing Science and Engineering, includes a solution of non-linear heat conduction equation (with temperature-dependent physical properties) using ANSYS for surface thermal gradients of circular beam and shaped beam profiles, and cooling rates. The application of shaped beam in the deposition of TiC powder is justified. And the microstructure formation is discussed. In addition, design of functionally graded die and mold inserts through the combination of selected materials is briefly described. Chapter 7 summarizes the general conclusions drawn from this body of research, and suggests future work that could yield better understanding of the other mechanical properties of functionally graded dies and molds.

Three appendices are attached. Appendix A describes the design of powder delivery system, powder delivery rate calibration, together with detailed uncertainty estimation analysis. Continuous and uniform powder transport is of great importance for the success of LBFF. Appendix B presents the design drawings of blocks to bridge the fabricated mold inserts and injection-molding machine for plastic injection. Appendix C is a formulation and a solution of a 3-D analytical model, based on the superposition of discrete Gaussian beam source, for moving laser beam depositing pre-placed powder to determine nominal

dimensions of molten pool and cooling rate by means of a high order recursive adaptive quadrature in Matlab.

CHAPTER 2. BACKGROUND

Solid freeform fabrication (SFF), or rapid prototyping (RP) and manufacturing, is a technology that generates physical models directly from graphical computer data [1]. Currently, SFF is entering a new phase where modern materials and manufacturing are used to produce functional geometry that is difficult in traditional manufacturing. This technology fits well in tool industry of small /medium-sized tools such as injection molding molds and dies casting dies [2]. While modest engineering progress has been made in this field since 1990, work on materials, processing, mechanical properties, and quality issues associated with these layer-wise additive processes remains to be addressed. Laser-based flexible fabrication (LBFF) is a SFF process we have designed to fabricate functionally graded molds and dies with efforts in solving the above problems. Following sections provide an introduction to the development of solid freeform fabrication, lasers for rapid prototyping, dies and molds, and functionally graded materials.

Solid freeform fabrication

SFF or RP enables speeding up of iterative product development processes. Layer-by-layer manufacturing, the core concept of RP technology, allows fabrication of three-dimensional parts by the addition of materials rather than by the subtraction of material (as in machining) [3,4]. In this layer-wise additive manufacturing process, a computer representation of a designed part is decomposed into slices that provide 2-D dimensional information (Figure 2.1). Although RP can be achieved by use of CNC machining, the term, however, is generally used in the context of fabricating parts by adding materials. The benefits of RP include: 1) quick tools for visualization and for concept verification due to its

capability of producing physical models of designed concept in short time to allow rapid evaluation of manufacturability and design effectiveness; 2) ability to fabricate complex structures that are difficult to be built with traditional techniques; 3) flexibility in automation in process planning and manufacturing; and 4) functional tooling in a short lead-time.

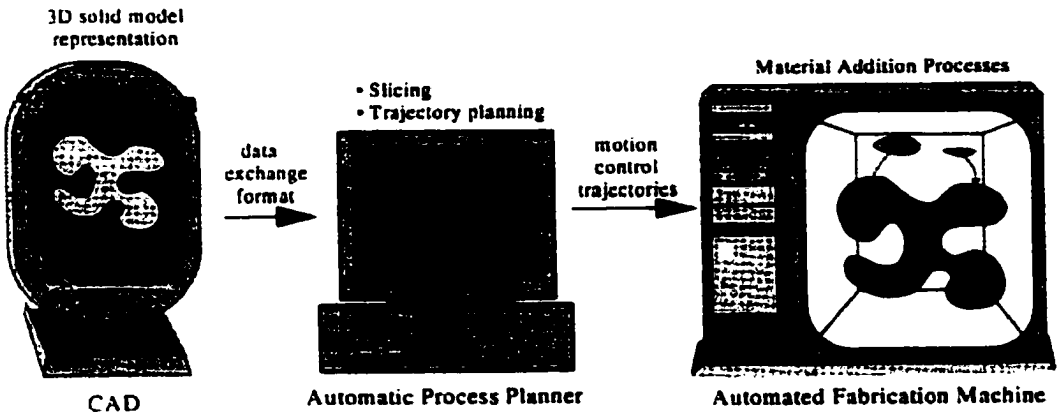

Figure 2.1. Schematic showing a 3-D model representation, slicing and process planning, and material additive process in SFF [5]

Rapid fabrication of near net shapes (NNS) is attributed to the absence of fixtures and tooling, the ability to work directly from computer geometric data, and the reduction of number of process steps [6]. It is gaining popularity as a means to significantly reduce the time to market [7]. Since the first RP technology, stereolithography, or three-dimensional printing, was introduced by 3D systems in 1982, more than 20 different rapid prototyping technologies are available, some of them enjoy commercial success. In terms of the initial form of the materials used, all RP systems can be categorized into liquid-based, powder-

based, and solid-based additive manufacturing processes. An overview of the RP systems is shown in Table 2.1.

Table 2.1. A list of additive manufacturing processes (RP) [1-4]

	Process	Configuration	Materials and Process Characteristics
Liquid	Stereo-lithography (SL)	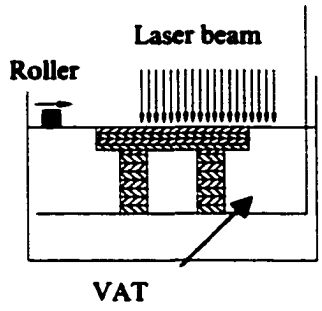	– Photo polymers; – Photo-polymerization by laser illumination; – Hazardous effect; – Concept model and virtual rapid prototyping (VRP).
	Fused Deposition Modeling (FDM)	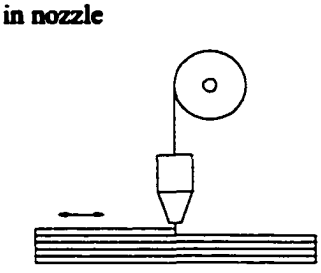	– Polymers, wax, metals with binder, and ceramic with binder; – Solidification by cooling; – Concept model, VRP, and limited functional uses.

Table 2.1 (continued)

Liquid	Ink Jet Printing (IJP)	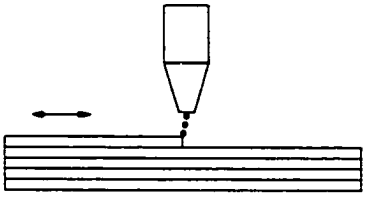	– Polymers, wax; – Solidification by cooling; – Concept model, VRP, and limited functional use.
Powder	Three Dimensional Printing (3D-P)	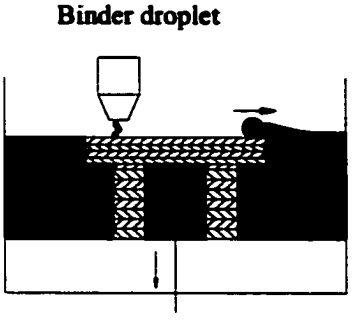	– Ceramic, metals, polymer, and binder; – No phase change; – Concept model, VRP, and limited functional applications.
	Selective Laser Sintering (SLS)	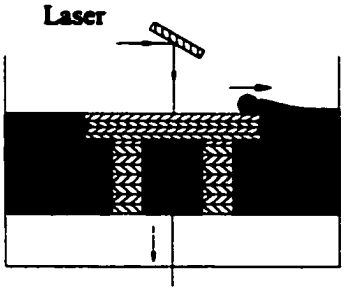	– Polymers, filled polymers, metals with binder; – Laser sintering; – Concept model, VRP, and partially functional use.
	Laser Cladding (LC)	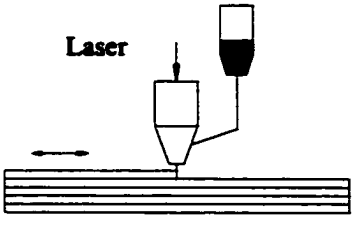	– Metallic powders of micro-scale; – Laser melting and solidification by cooling; – Functional applications.

Table 2.1 (continued)

Solid	Laminated Object Manufacture (LOM)	Laser 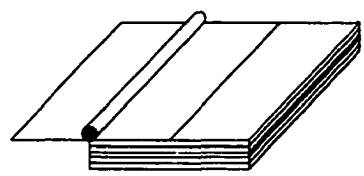	– Paper, polymer, polymer foam, ceramics, and metals; – Laser cutting, knife cutting, and heated wire cutting; – No phase change, alignment problem, and material wastage; – Concept model, VRP, functional applications.

Design for SFF affects not only the part surface integrity but also the strength. It is especially important when an over-hanged structure is desired because a viable design can greatly simplify the process with the least requirement of supporting structures and further post processing. Limited work has been done in this area. Functionality, surface roughness, minimal supporting structures and post processing will be the control variables for SFF design. Surrogate materials such as photo-polymers, powders, paper, wax, and plastics, and functionally metallic powders are the two major choices for RP. There are some RP systems beginning to build parts on structural materials, although many of the existing RP systems are still using surrogate materials. The functions of prototypes vary significantly depending on the RP process and the materials used for that process. The major application sectors of RP are in 1) design and analysis; 2) engineering and planning, and 3) tooling and

manufacturing (dies and molds). The industries benefiting from RP include, but not limited to, aerospace, automotive, electronics, biomedical, and appliance [8].

RP technology has been used to fabricate concept models, prototypes, and tooling for manufacturing dies and molds [9,10]. However, a significant limitation of RP systems is the use of surrogate materials rather than structural materials to construct prototypes, which are good only for the concept verification, visual prototyping, and limited functional applications. The physical, mechanical, and chemical properties of these surrogates do not allow them to be used for functional prototypes or tooling applications.

Selective laser sintering (SLS) of powder materials initially seemed to have potential for producing functional prototypes and even for direct tooling fabrication. However, it requires polymer binders or low-melting compounds to become feasible [11-14]. Because SLS just "wets" rather than really melts powder, drawbacks of shrinkage, porosity, and low density exist in components. These drawbacks prevent SLS from competing against conventional CNC milling and EDM for mold and die fabrication, and seriously limit the real-world applications of this process. Recently, RP systems based on laser-cladding (LC) technology have appeared to correct these deficiencies. LC is a surface engineering technology that creates surfaces of enhanced hardness, wear resistance, or corrosion resistance with minimal dilution. LC technology has been around for some 20 years and mainly been used for modifying surface properties or repairing damaged surfaces. It basically consists of pneumatically injecting fine powders through a nozzle into a localized molten pool created by a laser on the substrate surface. Subsequent solidification of the powder on the substrate produces strong, bonded layer. The benefits of LC are 1) fully dense and homogeneous microstructures; 2) low thermal damage to the underlying substrate, 3)

reduced grain growth and distortion; 4) non-equilibrium and amorphous structures, and 5) extension of solid solubility of alloying elements. These benefits, in turn, strengthen the tribological and mechanical properties including hardness, strength, wear resistance, corrosion resistance, and toughness. In addition, this process has the potential to remedy the surface defects on die and mold surfaces by re-melting. The commonly used powders are Co- and Ni-based alloys and carbides in micro-size. LC can be used to fabricate 3-D geometry if layers of overlapped-track are built continuously.

LC technology was applied to RP systems [15,16]. Several LC-based RP systems having minor variations were reported. These include 1) laser-engineered net shaping (LENS) from Sandia National Laboratory [17]; 2) direct light fabrication (DLF) from Los Alamos National Laboratory [18,19]; 3) direct metal deposition (DMD) at University of Michigan [20]; 4) shape deposition manufacturing (SDM) at Stanford University [21]; 5) laser direct casting (LDC) at the University of Liverpool [22]; and 6) the high-power, laser-based freeform fabrication process from the Pennsylvania State University [22]. Among all these versions, LENS is the only one having reached sufficient maturity to enter the commercial market (Optomec™ LENS Model 750). It uses a continuous wave (CW) Nd:YAG laser of high power (750 W) to melt an area on the surface of a metal substrate while a nozzle, being concentric with laser beam, simultaneously delivers metal powder to the molten pool. Layers are built in a direction perpendicular to the substrate, to increase the part height. The most common application of LENS is the direct fabrication of injection molds [17].

LC-based RP technologies offer flexibility to design with tailored materials and potential in producing components of high performance. However, none of the LC-based RP

systems has produced functional parts that are acceptable for industrial applications in terms of relevant standards due to rough surfaces (R_a, higher than 50 μm), low degree of dimensional accuracy (up to one millimeter offset from designed dimensions), and residual stresses existing in the components built by use of existing RP systems. In addition, issues such as design for SFF, material compatibility for complicated multi-materials construction, point-wise deposition of one or more materials to fabricate novel microstructural and macrostructural features, and process modeling remain to be addressed before these new techniques are technically and economically practical for widespread industrial use.

In this work, we have developed a technique, laser-based flexible fabrication (LBFF), to assist in solving these problems. It could be effectively used in creating parts (dies and molds, direct metal prototypes) with configurations such as graded interfaces, designed microstructures, and conformal cooling channels. It could also be used in other industrial applications including die and mold repairing, surface modification, and coatings. LBFF uses shaped laser beams, functionally graded materials, a CW CO_2 laser of 1500 W in rated power, and a computer integrated CNC control system. The shaped beams can fabricate layers of improved surface finish, dimensional tolerance, and reduced dilution among overlapped gradient layers. The shaped beam profiles produce more uniform temperature gradient than circular beam, and also stretch beam trailing edges to preheat the powders.

Lasers for rapid prototyping

Many RP systems use lasers and beam steering devices in one way or the other to expose photopolymers, to cut non-photosensitive materials, to sinter particulates, or to melt powder materials [1]. Lasers are stimulated emission devices that generate narrow, intense

beams of coherent light in wavelength ranging from ultraviolet to infrared regions. The first industrial laser was introduced in the late 1960s [23]. Lasers, the versatile industrial tools, find wide applications in manufacturing ranging from machining (cutting, drilling, milling, scribing, and marking) and joining (welding, brazing, and soldering) to materials processing (powder synthesis, thin films, and heat treatment) due to their advantages in precision, productivity, flexibility, and automation.

A variety of lasers including solid, liquid, and gas are available. Each specific type of laser is normally identified by the medium that produces the light emission. The basic characteristics of laser beams are 1) energy density (power density), 2) wavelength, 3) coherence, 4) mode and beam diameter, and 5) polarization. Energy density is of great importance in materials processing. Excessive energy density may evaporate materials and create molten surface of high roughness; too low energy density may not melt materials fully and result in insufficient bonding. Wavelength affects the laser beam size and the absorption of a given material. Usually a beam of short wavelength and small divergence produces small spot size. Materials tend to absorb laser beam of short wavelength more efficiently.

The lasers most widely used in industry for material processing are solid-state neodymium-doped yttrium-aluminum-garnet (Nd:YAG) lasers, gas carbon dioxide (CO_2) lasers, and gas excimer lasers, because they have the ability to produce high power outputs and flexibility in controlling laser parameters such as pulse width, power, and wavelength. Nd:YAG laser is the most common member of solid-state lasers with wavelength of 1.06 μm. It can generate CW beams with power ranging from a few milliwatts to over a kilowatt, pulsed beams of average power up to several kilowatts with reasonable efficiency. Nd:YAG laser operates on optical pumping, raising Nd atoms to an excited energy level by means of

light from external sources. The major industrial uses of Nd:YAG laser are in metal drilling, spot welding, marking and resistor trimming. Because of its high peak power and short wavelength, and easiness for beam delivery by means of optical fibers, Nd:YAG laser has also found applications in medical field. Carbon dioxide laser, with wavelength ranging from 9 to 11 μm, is one of the most versatile gas lasers. It is called as industrial work horse because of its ruggedness and reliability. It can run in both CW mode and pulsed mode. In CW mode, CO_2 laser is capable of producing beam power from well under one watt to several tens kilowatts, while in pulsed mode, it can generate pulses of nanoseconds to milliseconds. Carbon dioxide lasers are pumped by use of electrical discharge, and mainly find applications in cutting, welding, and heat treatment.

Laser power, beam profile and dimensions, and traverse speed are important parameters for materials processing. Beam profiles can be varied using diffractive optics. Usually power density, dwell time, and sometimes also laser wavelength define the processing ranges for specific applications as shown in Figure 2.2.

The availability of computer controlled positioning stages, computer aided design techniques, and laser technology advances the development of RP systems. The integration of these technologies has already impacted the fabrication of shaped structural materials. The laser-associated RP technology is changing the traditional material removal manufacturing and will eventually be a replacement for subtractive processes to generate functional components such as dies and molds.

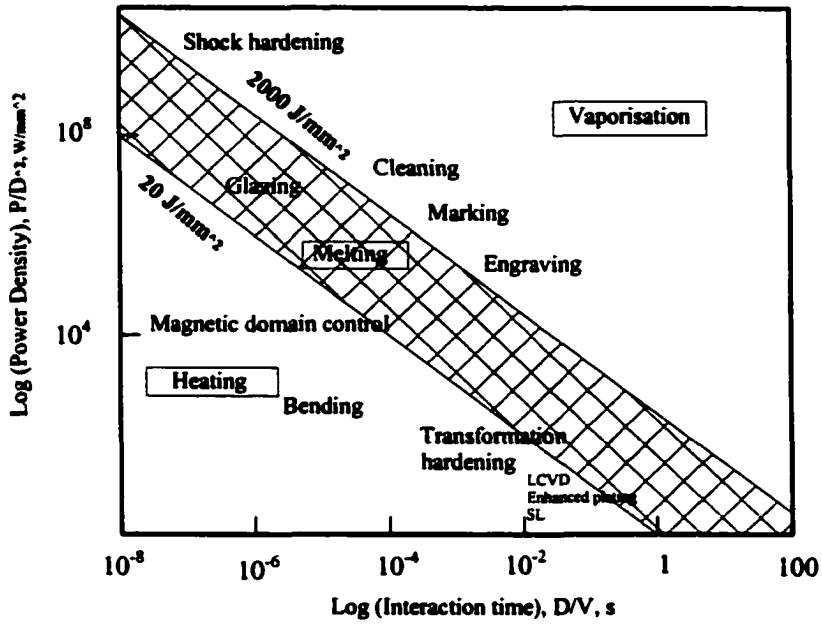

Figure 2.2. Window of laser power density and interaction time suitable for material processing applications [24]

Dies and molds

Dies and molds are important tooling in non-ferrous casting (aluminum, zinc, magnesium, and etc.), plastic injection molding, and forming (cold extrusion and hot extrusion, stamping, and forging) industries. The global market for dies and molds is estimated at 65 billion US dollars [25]. Dies and molds constitute a major portion of costs associated with manufacturing operations such as injection molding, die-casting, stamping, extrusion, and forging. For a company or an industry to survive in today's fiercely competitive market, modern materials and fabrication technologies must be used to shorten the product time to market and produce products of high quality and cost-effectiveness. Dies and molds are becoming standardized to construct easily and to reduce cost [26]. Often dies and molds are composed of supporting and functional components [25,26]. Parts with square

or round shape, which are readily designed and made, usually serve as bases or supporting blocks for immediate use. The other supporting components are used for alignment, part ejection, and heating or cooling. Functional components, which include die cavity, core insert, and punch, have to be designed specifically to tailor for different applications. The cavity and core inserts for injection molding and die-casting are usually made out of solid blocks of alloy steels Occasionally, forging dies and injection molds are manufactured by cold or hot hobbing. The widely used materials for dies and molds are hot work tool steel H series (chromium type), mold steel P series (chromium type), among which H13 and P20 are the two mostly often used [27]. The general requirements for die and mold materials are (1) strength and toughness at elevated temperature, (2) mechanical and thermal shock resistance, (3) hardness, and (4) wear resistance [26-28].

Design of dies and molds is generally an iterative process though various CAD/CAM and virtual prototyping (VR) technologies are available to assist or speed up the process. Die and mold design must be closely interactive with processes because design models have to be updated accordingly after any modification to the prototypes. When methods are chosen for manufacturing mold and die parts, important criteria of feasibility, cost, productivity and quality have to be considered [26]. Usually the conventional fabrication of dies and molds starts with rough machining followed by finishing and tryout processes. Currently milling (CNC, high speed milling) and electrical discharge machining (EDM) are the two major methods used to make most of dies and molds out of wrought tool steel blocks [25,26]. They are classified as subtractive processes. The sequential steps of processing used in traditional die and mold manufacturing are shown in Figure 2.3.

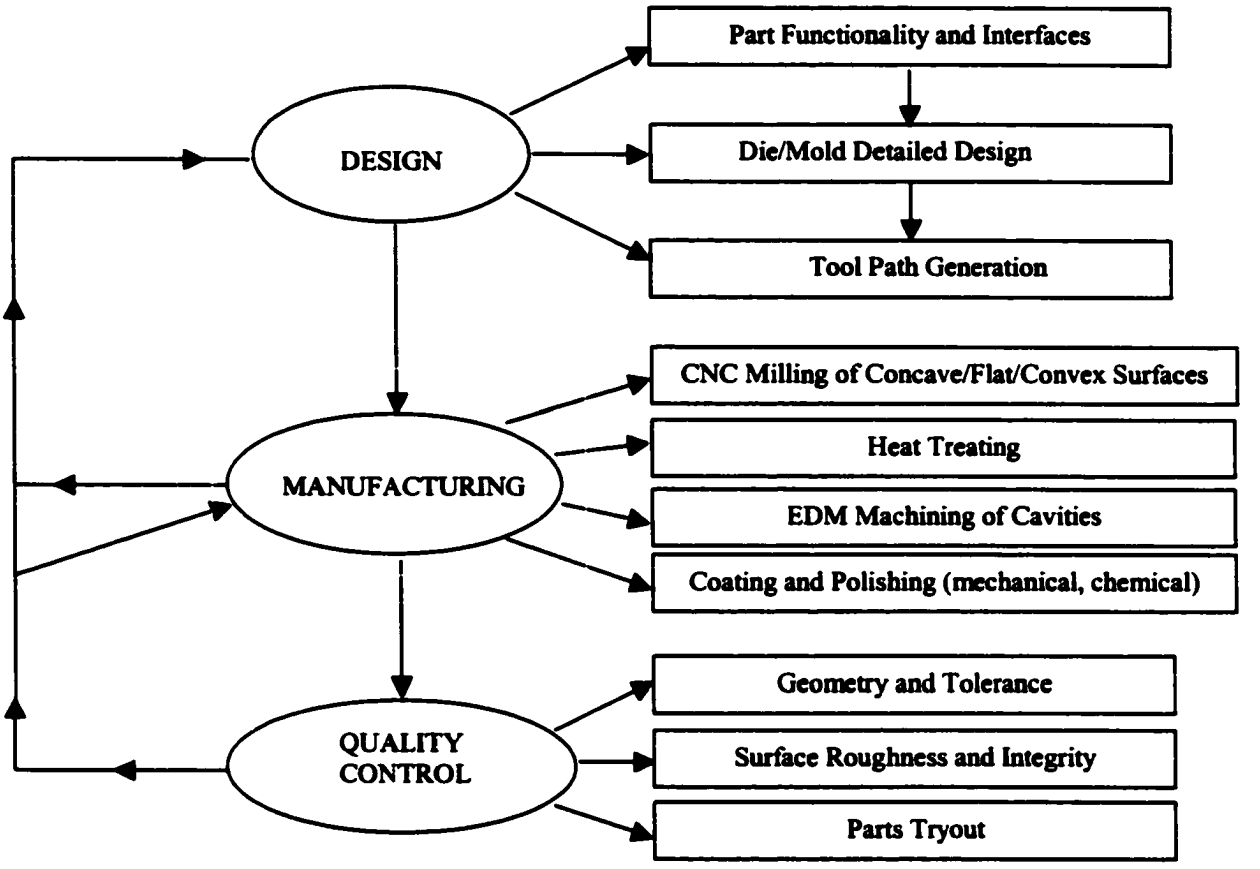

Figure 2.3. A flow chart showing the process plan for conventional manufacturing of dies and molds

Die and mold machining is a costly and time-consuming process, in which a significant portion of material is wasted. Also, machining does not allow for flexibility in obtaining the desired tool geometry. For example, conformal cooling channels and holes, which could increase product throughput by some 25% or more, are difficult to produce in traditional machining [29]. In addition, the machined mold often has to be subsequently heat-treated, surface treated or coated to impart the desired microstructure and properties. The

heat treatment, if improperly treated, causes dimensional instability and generates residual stresses. Study has showed that more than 70% of die failures are attributed to the improper heat-treatment of the steels [30]. Post-treatment operations such as grinding and EDM may damage the surface integrity if not carefully executed because these operations can easily result in tempered layers and soften the surface materials [26]. Alternatives to machining are powder consolidation processes such as hot isostatic pressing (HIP), which uses rapidly solidified powders to produce dies and molds that outperform cast and machined tools. However, the high cost and long lead-time of these processes limit their applications [31].

Functionally graded materials

A functionally graded material (FGM) is a combination of two or more materials in which a gradual transition among compositions and microstructures across the interface exists rather than the distinct junction found in laminated composites or coatings. In a FGM, there is no "gap" of material properties due to its composition and structure gradually changing over volume. Design of FGMs is to ascertain required properties that one material normally does not have by varied combinations of constituent materials. It is usually represented by the geometry of a FGM with the spatial distribution of its constituent materials, microstructures and properties. Besides functional requirements of properties, compatibility between materials, residual stresses, and component element diffusion at elevated temperatures are also of great concerns in designing a FGM. Quantitative microstructural analysis methods are helpful in understanding the fundamental relationships between structures and properties. Rules of mixtures, variational approach, micromechanical methods, and empirical approach are usually used to estimate the properties [32].

A variety of processing techniques are available for fabricating of FGMs. These processing methods include powder metallurgy, physical and chemical vapor deposition, plasma spraying, self-propagating high temperature synthesis (SHS), galvanoforming, and the most recently solid freeform fabrication. Basically, most of these methods work on either constructive processing or mass transport mechanism. Constructive processing starts with addition of thin slice of materials on a substrate; and mass transport is closely related to the flow of fluids, the diffusion of molecules or atoms, or the conduction of heat. Usually different processing techniques and conditions result in FGMs exhibiting significantly different microstructures and properties. The characterization of FGMs includes the evaluation of their local microstructures and properties. Determination of size, orientation, and phases of local microstructures can be achieved by means of optical microscopes, scanning electron microscope (SEM), and chemical analysis; and evaluation of properties such as microhardness, thermal conductivity, fatigue behavior, and so on may be measured by use of standardized technique or designed experiment.

The FGM concept has been demonstrated in many engineering applications, including cutting tools, machine parts, and engine components. Typical examples of FGMs are SiC/C, WC/Co, and FeAl/SS. One SFF technique, extrusion freeform fabrication (EFF) with multiple extruders, has been developed to produce prototype of alumina/NiAl, alumina/stainless steel, and WC/NiAl [33].

References

1. P.F. Jacobs, Rapid Prototyping & Manufacturing: Fundamentals of StereLithography, Society of Manufacturing Engineers, Dearborn, MI 48121-0930, 1992.
2. K.W. Dalgarno, Production Grade Tooling via Layer Manufacture, Rapid Prototyping Journal, 7(4), 2001, pp203-206.
3. J.P. Kruth, Material Ingress Manufacturing by Rapid Prototyping Techniques, Annals of the CIRP, 42(2), pp603-614, 1991.
4. J.P. Kruth, M.C. Leu, and T. Nakagawa, Progress in Additive Manufacturing and Rapid Prototyping, 42, (2), pp525-540, 1998.
5. J.J. Beaman, J.W. Barlow, D.L. Bourell, R.H. Crawford, H.L. Marcus, and K.P. McAlea, Solid Freeform Fabrication, Kluwer Academic Publishers, Boston, 1997.
6. M. Burns, Automated Fabrication: Improving Productivity in Manufacturing, Prentice-Hall, Englewood Cliffs, NJ, 1993.
7. N.B. Dahotre (ed.), Lasers in Surface Engineering, ASM International, Materials Park, OH 44073-0002, 1998.
8. Chee-Kai Chua and Kah-Fai Leong, Rapid Prototyping: Principles & Applications in Manufacturing, John Wiley & Sons (Asia) Pte Ltd, Singapore 128909, 1997.
9. C. Hull, M. Feygin, Y. Baron, R. Sanders, E. Sachs, A. Lightman, and T. Wohlers, Rapid Prototyping: Current Technology and Future Potential, Rapid Prototyping Journal, 1(1), pp11-19, 1995.
10. A. Kochan, Rapid Prototyping Trends, Rapid Prototyping Journal, 3(4), pp150-152, 1997.

11. M. Agarwala, D. Bourell, J. Beaman, H. Marcus, and J. Barlow, Direct Selective Laser Sintering of Metals, 1(1), pp26-36, 1995.

12. K. Subramanian, N. Vail, J. Barlow, and H. Marcus, Selective Laser Sintering of Alumina with Polymer Binders, Rapid Prototyping Journal, 1(2), pp24-35, 1995.

13. F. Klocke, T. Celiker, and Y, -A. Song, Rapid Metal Tooling, Rapid Prototyping Journal, 1(3), pp32-42, 1995.

14. I. Gibson, D. –P. Shi, Material Properties and Fabrication Parameters in Selective Laser Sintering Process, Rapid Prototyping Journal, 3(4), pp129-136, 1997.

15. J. Gerken, H. Haferkamp, and H. Schmidt, Rapid Prototyping/Manufacturing of Metal Components by Laser Cladding, Proceedings of the 27th International Symposium on Automotive Technology and Automation, Oct 31-Nov 4, Aachen, Germany, pp 85-90, 1994.

16. J.Y. Jeng, S.C. Peng, and C.J. Chou, Application of Selective Laser Cladding in Rapid Prototype, Proceedings of the 27th International Symposium on Automotive Technology and Automation, Oct 31-Nov 4, Aachen, Germany, pp272-279, 1994.

17. D.M. Keicher, W.D. Miller, LENS™ Moves Beyond RP to Direct Fabrication, Metal Powder Report, 53(12), pp26-28, 1998.

18. J. Milewski, G.K. Lewis, D.J. Thoma, G.I. Keel, and R.B. Nemec, Direct Light Fabrication of a Solid Metal Hemisphere Using 5-axis Powder Deposition, Journal of Material Processing Technology, 75, pp165-172, 1998.

19. J. Milewski, G.K. Lewis, J. Fonseca, and R.B. Nemec, Laser Powder Deposition of a Near Net Shape Injection Mold Core-A Case Study, Materials and Manufacturing Processes, 15(2), pp247-258, 2000.

20. J. Mazumder, J. Choi, K. Nagarathnam, J. Koch, and D. Hetzner, The Direct Metal Deposition of H13 Tool Steel for 3-D Components, Journal of Metals, pp55-60, May, 1997.

21. G.R. Link, J. Fessler, A. Nickel, and F. Prinz, Rapid Tooling Die Casting Inserts Using Shaped Deposition Manufacturing, Materials and Manufacturing Process, 13(2), pp263-274, 1998.

22. R. Irving, Taking a Powder, Mechanical Engineering, pp55-59, September, 1999.

23. A.G. Grigoryants, Basics of Laser Material Processing, Mir Publishers, Moscow, 1994.

24. J. Mazumder, O. Conde, R. Villar, and W. Steen (ed.), Laser Processing: Surface Treatment and Film Deposition, Kluwer Academic Publishers, Dordrecht, 1996.

25. T. Altan, P. Fallbohmer, and C. Ridriguez, HSM Research-On the Edges of Technology, online article, http://www.modernmachine-shop.com/articles/hsm-9801.html, April 10, 2002.

26. K. Stoekhert (ed.), Mold-Making Handbook: For the Plastics Engineer, Hanser Publishers, New York, 1983.

27. E.A. Herman, Die Casting Dies: Designing, Society of Die Casting Engineers Inc., Detroit, MI 48253,1979.

28. S. Kalpakjian and S.R. Schimid, Manufacturing Engineering and Technology, Prentice Hall, Inc., Upper Saddle River, New Jersey 07485, fourth edition, 2001.

29. P.F. Jacobs, New Frontiers in Mold Construction, NASA Tech Briefs, 23(3), 1999.

30. P. Pullen and V. Merchant, Lasers in the Die and Mold Industry, Industrial Laser Review, pp13-16, April, 1996.

31. M. Agarwala, D. Bourell, J. Beaman, H. Marcus, and J. Barlow, Direct Selective Laser Sintering of Metals, Rapid Prototyping Journal, 1(1), 1995, pp26-36.

32. Y. Miyamoto, W.A. Kaysser, B.H. Rabin, A. Kawasaki, and R.G. Ford, Functionally Graded Materials: Design, Processing and Applications, Kluwer Academic Publishers, Boston/Dordrecht/London, 1999.

33. G. Hilma, Innovative Techniques for Rapid Prototyping Parts of Polymers, Metals, Ceramics, Composites and Functionally Graded Materials, Materials Technology, 11(6), pp226-228, 1996.

CHAPTER 3. NANOCRYSTALLINE TiC POWDER ALLOYING AND GLAZING OF H13 STEEL USING A CO_2 LASER FOR IMPROVED LIFE OF DIE-CASTING DIES

A paper published in Surface and Coatings Technology (2001)

Wenping Jiang and Pal Molian

ABSTRACT

Premature failures of die-casting dies used in the metal casting industry occur because of the damages caused by thermal fatigue, erosion, stress corrosion, and soldering on die surfaces. In this work, the effects of two laser-surface-treatment methods for the prevention of die failures were investigated. A 1500 W CO_2 laser with round and line beam shapes was employed to glaze the H-13 steel substrate or alloy the substrate with TiC of various particle sizes (30 μm, 2 μm, and 300 nm). Laser parameters for the glazing and surface alloying processes were optimized, the criteria being a specified surface finish and surface integrity. The corrosion and erosion properties of laser treated samples in aggressive casting conditions were evaluated by testing them in molten aluminum alloy A390.

Laser glazed and alloyed specimens with micron-sized particles exhibited hardness 30% to 100% higher than that of heat-treated H-13 steel substrates. However, hardness of specimens that were laser-alloyed with 300 nm particles was lower, approximately 25% of that of the substrate. The anomalous effects of nanocrystalline powder alloying could not be explained satisfactorily by the evidence of microstructures obtained by use of optical microscopy, scanning electron microscopy, and X-ray diffraction. However, it is hypothesized that some titanium dissolves in steel, promoting formation of ferrite in preference to austenite at high temperatures and thereby decreasing the hardness. Laser

glazing and alloying improved resistance of H-13 steels to both corrosion and erosion, but marked improvement occurred in the specimens alloyed with nanocrystalline powders. The beneficial effects of nanocrystalline alloying are attributed to smooth, crack-free, and tough surface layers as well as uniform and homogeneous microstructures. Laser surface processing of nanocrystalline materials is potentially important in the casting industry for improving die life and reducing downtime.

INTRODUCTION

Die-casting processes are increasingly used to produce metal castings because of their high quality, low cost, and short lead-time. However, premature failures from the damages of thermal fatigue, erosion, stress corrosion, and soldering on die surfaces significantly degrade the quality and increase the cost of castings [1]. Research has indicated that surface treatment and coating could be an effective way in protecting die surfaces from thermal fatigue and extending die life by reducing the damage at contact surfaces [2]. Surface heat treatment and shot peening processes prolong die life by changing the state of residual stress at the surface from tension to compression. Coatings can reduce die wear even more because they offer improved hardness, toughness, and corrosion and oxidation resistance in addition to possibly favorable compressive residual stresses.

For a coating to be effective, it must meet the requirements of: 1) excellent bonding; 2) adequate thickness; 3) absence of flaws; 4) suitable Mechanical properties (strength and toughness); 5) thermal shock resistance; and 6) high-temperature stability [3]. Thermal spraying, physical and chemical vapor deposition (PVD and CVD), ion implantation and ion-assisted coatings were employed to produce coatings of the types SiC, TiN, TiB_2, TiAlN,

CrN for enhancing die life [4]. However, the coatings produced by these processes are not capable of ensuring long-term protection to die surfaces, because they do not meet all the requirements listed above. For example, plasma-sprayed coatings are porous and weakly bonded to the base metal, while PVD coatings (sputtering, vacuum evaporation, and ion-plating) are too thin and promote heat checking through the crack initiation at the interface between the coating and substrate. CVD is a high-temperature process that degrades the heat-treated properties of the die substrate. Other surface coating processes currently being used for dies are thermal diffusion [5], plasma spray process [6], and electrodeposition [7]. Some PVD coatings provide significant corrosion and erosion resistance to molten aluminum [8]. Among the various PVD (TiN, TiAlN, CrN) coatings tested on H13 steel dies [9], TiN coating resulted in the least improvement because of poor heat checking resistance. Ion implantation of steel and tungsten carbide tools with nitrogen increased the resistance to abrasive wear [10].

Lasers have been recognized as potential means of surface treatment and coating. They provide unique opportunities for tailoring novel engineering surfaces without changing the bulk properties and producing of non-equilibrium structures unattainable by conventional processes. Typical laser surface processing techniques include transformation hardening, melting, cladding, alloying, and annealing [11-17]. The benefits of laser surface processing include: 1) fine-grained and homogeneous microstructures; 2) low thermal damage to the underlying substrate; 3) reduced grain growth and distortion; 4) non-equilibrium and amorphous structures; and 5) extension of solid solubility of alloying elements [18,19]. These benefits in turn enhance the tribological and mechanical properties, including hardness, strength, wear resistance, corrosion resistance, and toughness.

Two processes readily applicable to die-casting dies are laser glazing and alloying. In laser glazing (LG), a very thin layer (< 0.5 mm) is melted and "self-quenched" at a rapid cooling rate, leading to fine grain structures that contain metastable and supersaturated phases and increased homogeneity. For example, laser glazing of 440C stainless steel produced a surface layer of fine carbides in tempered martensite that enhanced the impact resistance of heavily loaded bearings [2]. For some alloys, it is even possible to obtain nanocrystalline or amorphous structures. In addition, laser glazing has the potential to seal the heat checks formed on the die surfaces and allow relaxation of surface stresses.

Laser surface alloying (LSA) has characteristics similar to those of LG but, in addition, changes the chemical composition of surface layers. Both processes use high power density and short interaction time of the laser beam so that the heating effect is concentrated in thin regions. This leads to development of extremely high thermal gradients, which promote rapid solidification of the melt (cooling rates can reach 10^6 K/sec). With continued cooling, the solidification front starts at the melt layer/substrate interface and progressively moves toward the surface.

In this work, we report a detailed investigation of laser glazing of H-13 die steel and laser surface alloying of micro and nanocrystalline TiC powders onto H-13 die steel. The effects of LG and LSA on surface finish, hardness, microstructure, corrosion, and erosion of the die steel are presented. These two processes are advantageous over other laser processes with respect to operational simplicity, enhancement of corrosion and wear resistance, and surface finish and dimensional tolerance. The two processes can also be effectively used to overlay at the corners of the die to repair erosion damages and cracks.

MATERIALS AND PROCEDURES

The die material used was premium grade H-13 steel, heat-treated to the specifications of NADCA. Table 3.1 specifies the chemical composition of the steel. Hot-rolled bars of H-13 die steel obtained from Uddeholm were cut into small blocks of nominal size 60 mm× 30 mm × 12 mm. The edges were rounded off to remove or reduce the stress rising points, and samples were then subjected to a heat treatment cycle (Figure 3.1). The final hardness after heat treatment was 46 to 48 HRC.

Table 3.1. Nominal chemical composition of H-13 steel

Element	C	Mn	Si	Cr	V	Mo
Weight %	0.4	0.4	1.1	5.0	1.1	1.0

TiC was chosen as a coating material because it is one of the most commonly used die-coating materials and has excellent physical properties (Table 3.2). TiC was obtained in the form of powders with three particle sizes: 30 μm, 2 μm and 300 nm. Because of commercial availability, the micron-sized powders were procured directly from commercial vendors (30 μm powders from Atlantic Equipment, New Jersey, and 2 μm from Johnson Matthey). However, nanocrystalline powder production is still in the research stage and is available only in small quantities. A few grams of nanocrytsalline TiC powders, synthesized at ambient temperatures by mechano-chemical processing [20], were received from the University of Idaho. To produce nanocrystalline TiC powders, researchers at the University

of Idaho had used mechanical milling to initiate and complete the following chemical reaction inside a Spex 8000 milling vial:

$$TiCl_4 + 2\,CaC_2 \longrightarrow TiC + 2\,CaCl_2 + 3\,C + \Delta H$$

The exothermic reaction started after 12 minutes of milling. The by-product $CaCl_2$ is leached out sequentially by dilute formic acid and de-oxygenated water, with the aid of an ultrasonic vibrator to enhance salt dissolution and a centrifuge to settle the leached fine powder in the leaching liquid.

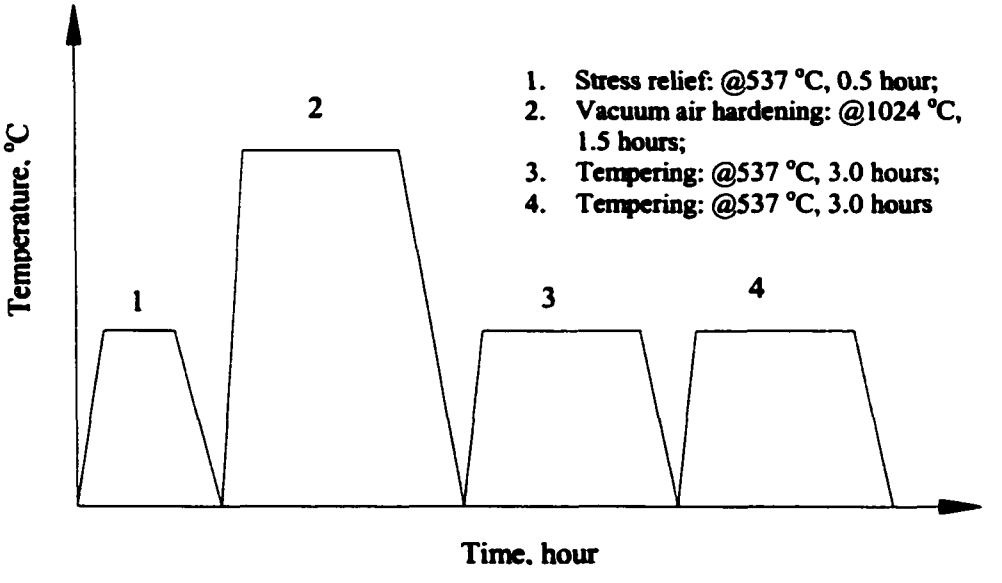

Figure 3.1. Heat treatment of H-13 steel

Nanocrystalline powders produced by this method have barely detectable oxygen contents, which provide improved particle-wetting characteristics. The as-received nanocrystalline TiC powder was characterized by X-ray diffraction (XRD) and transmission electron microscopy (TEM). The XRD pattern (Figure 3.2(A)) showed several peaks

corresponding to the presence of single phase TiC. Detailed examination of the fine crystals by TEM (Figure 3.2(B)) revealed their size to be in the range of 20 to 500 nm, with a nominal size of 300 nm.

Table 3.2. Physical properties of TiC powder

Melting point (°C)	3140
Boiling point (°C)	4820
Hv Hardness (kg/mm^2)	3200
Density (g/cm^3)	4.93
Crystal structure	Cubic
Electrical resistivity ($\mu\Omega$-cm)	180-250

A CO_2 laser was used to conduct LG and LSA because of its high power and Gaussian beam profile that can focus beam to a small spot size. Figure 3.3 shows the schematic of experimental setup. All experiments were performed with the Model 820 Rofin-Sinar® continuous wave (CW) CO_2 laser, which has a rated power output of 1500 W. The beam was delivered to the sample through a focusing lens with focal length of 127 mm and diameter 28 mm.

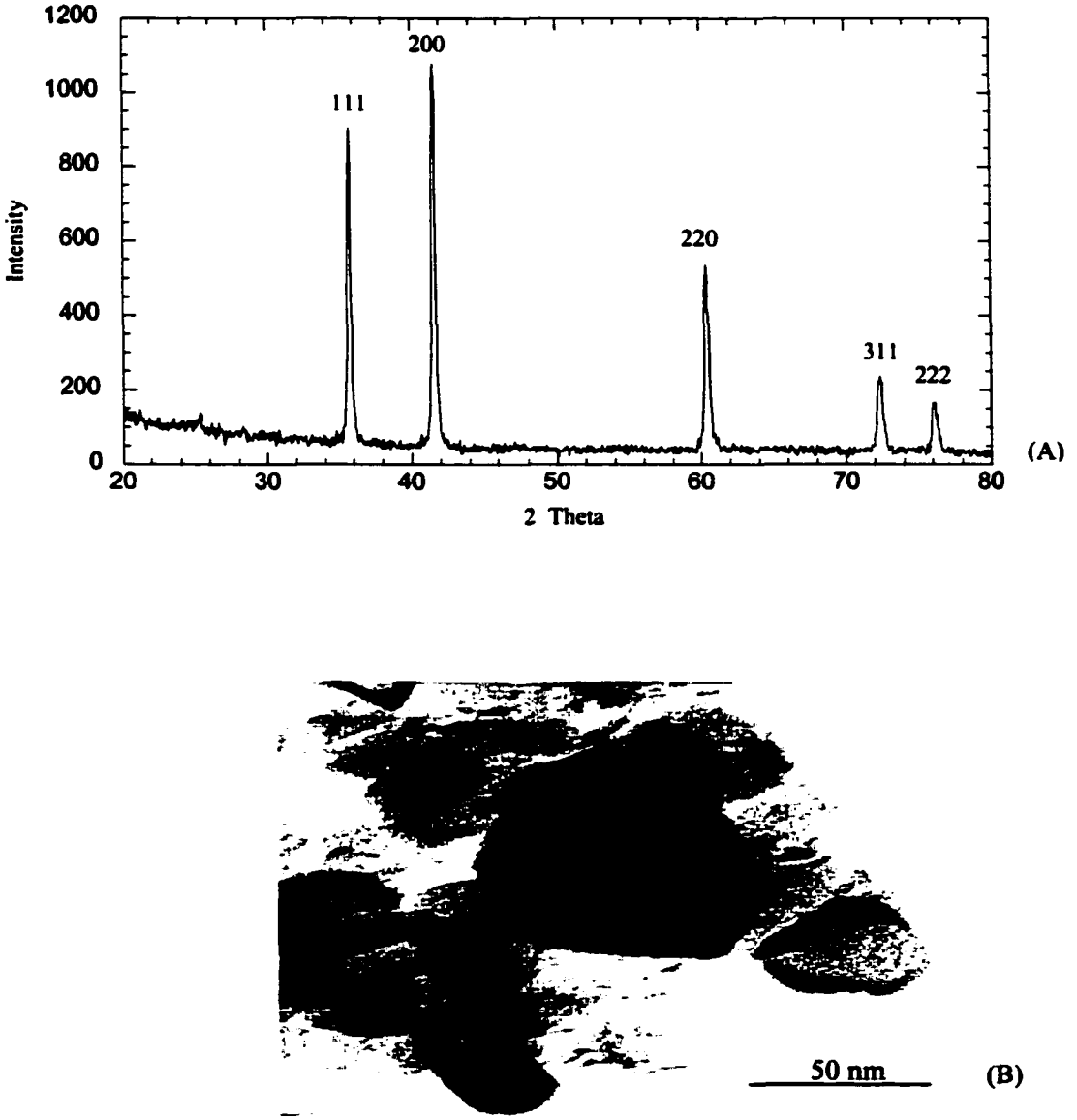

Figure 3.2. (A) X-ray diffraction pattern of nanocrystalline powders of TiC; and (B) TEM micrograph of TiC powders

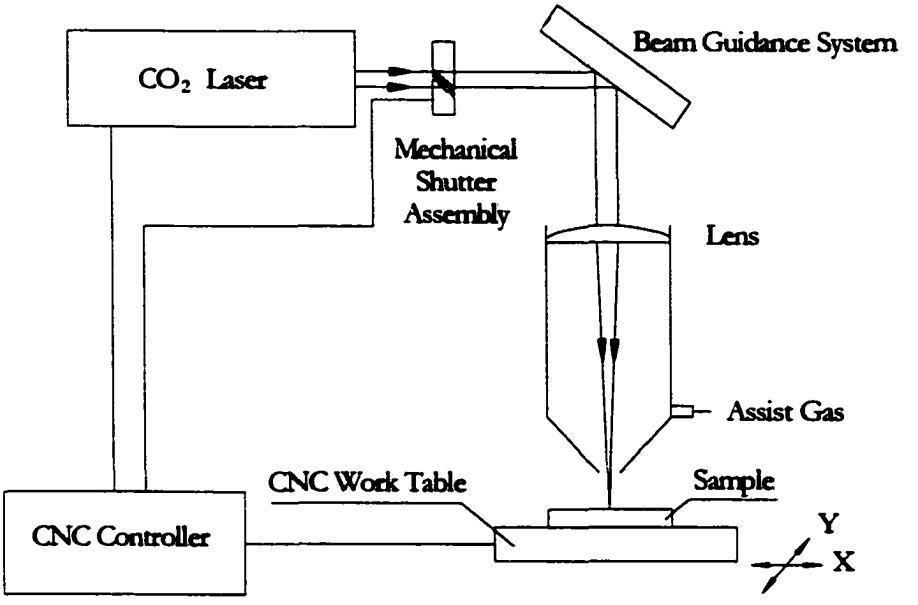

Figure 3.3. Schematic showing the laser setup for surface processing

Laser experiments were conducted with the power varying from 500 W to 1500 W, and with the traverse speeds of the samples in the range of 17 mm/sec to 254 mm/sec. The laser beam profile was shaped from round to line by use of a combined cylindrical/spherical lens. The effects of a linear beam profile were compared with the effects of the round beam profile. The samples were mounted on the worktable, and the focus position was adjusted from the surface to 10-mm below the surface. The assist gas was flown into the laser interaction zone at a pressure less than 7 kPa (1 psig). Both single and multiple scans of laser processing were performed using a computer numerically controlled (CNC) worktable. The overlap in multiple scans ranged from 10% to 30%.

Laser Glazing (LG)

In this process, the laser beam was used to melt the surface of H-13 samples by a raster-scanning procedure to achieve the rapid solidification that, in turn, facilitates production of fine and homogeneous microstructures. A number of combinations of laser parameters including power (500 W, 1000 W, and 1500 W), focus position (surface and below surface), beam profile (circle and line), and traverse speed (from 17 mm/sec to 254 mm/sec) were attempted. Experiments were repeated four to six times for each set of conditions. The objective is to determine the optimum settings to produce smooth (R_a <5 μm) and crack-free layers. Table 3.3 lists such optimum parameters for laser glazing.

Table 3.3. Optimum parameters for laser glazing of H13 steel

Power (W)	500
Beam geometry	Circle
Focus	Surface
Spot size (mm)	0.2
Traverse speed (mm/sec)	127
Overlap (%)	10~30
Assist gas	Argon

Laser Surface Alloying (LSA)

LSA is a coating process that changes the chemical composition and microstructure of the surface layers. In this process, the coating material is pre-placed (or injected into the molten pool) on the substrate, and the laser is then used to melt the coating and a portion of the substrate to form an alloyed zone. In this work, slurry of TiC was prepared for the 30 μm and 2 μm powders, with a solution of agar and water used as the bonding agent. First, 1.5 grams of agar was added to 1000 ml of distilled water. The mixture was then heated to 85 °C (accompanied by proper stirring) to obtain a homogeneous solution. Second, the TiC powder was mixed with the agar solution to form the slurry. For the 300 nm powder, alcohol was used to form the slurry because of its easy dissolution. The slurry was applied to the substrate surface uniformly to a specific thickness and then dried by use of an electric heater. The thickness was built up by adding more slurry. During the drying process, the baking temperature was held at 40°C for a few minutes. If the baking temperature was too high or baking time was too long, then a "boiling" phenomenon occurred, resulting in a disrupted layer.

The powder was pre-placed to four thickness values: 0.01 mm, 0.02 mm, 0.1 mm and 0.4 mm. The thickness of the coating layer was determined using a weighing method. First, the exact dimensions and initial weight of a sample were measured, using a dial caliper of 0.025 mm in accuracy and an electronic balance of 0.001 gram in accuracy. The coating was applied, then dried and weighed. By using the density of TiC carbide, the coating thickness was estimated. LSA was performed using a range of laser parameters similar to those used for LG. The optimum parameters (Table 3.4) were selected based on the criteria of surface smoothness (R_a <15 μm) and absence of flaws. Experiments were repeated four to six times

for each set of conditions. It should be pointed out that the circular beam did not provide satisfactory results.

Table 3.4. Optimum parameters for LSA of TiC powder on H13 steel

Power (W)	500
Beam geometry	Line
Focus	Surface
Spot size (mm)	0.1×1
Traverse speed (mm/sec)	42.3
Overlap (%)	10~30
Assist gas	Argon

Tempering Process

A few samples of LSA with 2 μm TiC powder were tempered at 206 °C (400 °F) to reduce the residual stresses generated by the laser processing. The samples were kept at this temperature for 2 hours and then left in the furnace to cool to ambient temperature.

Characterization and Testing

Surface roughness

A surface profilometer with a 0.025 mm diamond probe was used to measure the surface roughness (arithmetic average, R_a) of laser-glazed and alloyed samples in both the longitudinal and transverse directions. Differences in surface roughness between the two

directions were insignificant. The surface roughness of as-received samples was also measured for comparison purposes.

Metallography

The laser-processed samples were observed under an optical microscope to detect flaws, including porosity and microcracks. The width of the single-pass laser treated zone was measured and used to determine the overlap distance for multiple passes. After that, the samples were sectioned using a cut-off wheel flooded with water to prevent tempering. The samples were ground using 80-grit sandpaper and mounted in Bakelite, polished sequentially with 240, 320, 400, and 600-grit emery papers, and then polished with a cloth using 6 μm diamond paste. The samples were etched in a solution of 5% nitric acid in methanol. Etching time was about 1.5~2 minutes. Scanning electron microscopy was then used to characterize the depth, profile, flaws, and microstructure of laser treated layers.

Vickers microhardness test

The mounted samples were placed in a Tukon® microhardness-testing machine and were subjected to a load, P, of 1.0 Kgf. A diamond pyramid indenter was used to generate square indentations. Vickers microhardness was calculated by measuring the diagonal length, d_1, of square indentations and using the formula:

$$VHN = \frac{1.854P}{d_1^2} \qquad (1)$$

The hardness gradient along the depth of laser-treated layers was also determined.

X-ray diffraction measurements

X-ray diffraction (XRD) using copper K_α radiation was performed on selected samples to determine the effect of glazing and alloying on the microstructural phases.

Corrosion and erosion test

For the coatings to be used successfully in the industry, they must be tested for their resistance to erosion, corrosion, and heat checking. In this work, corrosion and erosion tests were performed using aluminum alloy A390 with high silicon content (16%) because A390 causes more wear to the die surface than other aluminum melts. An accelerated corrosion test was set up to evaluate the dissolution rate of as-received H13 steel, LSA (2 μm and 300 nm powders), and LG specimens in both static and agitated melts. Figure 3.4 is a schematic diagram of the corrosion/erosion test setup that initially held only one sample but was later modified to hold up to four samples. Samples were held symmetrically in a rotating arm, which was driven by an electric motor. The input voltage was controlled to obtain a speed of 50 rev./min of the rotating arm. The rotation speed allows the effects of melt flow on the sample erosion behavior to be studied. The A390 melt was covered with equal parts of potassium chloride and sodium chloride with 5~10% of additional sodium fluoride. The salt solution was used to reduce oxidation, and to prevent gas absorption and metal loss of the molten A390. Samples were quenched in water after the desired corrosion/erosion time and then cleaned with 5% NaOH solution. The weights of the test samples were measured before and after each test. The data from samples that were placed in the melt without any rotation represented a measure of corrosion resistance, whereas the data from the samples that were rotated at different speeds was taken as a measure of erosion resistance. For each test, four data points were collected and the scatter was analyzed.

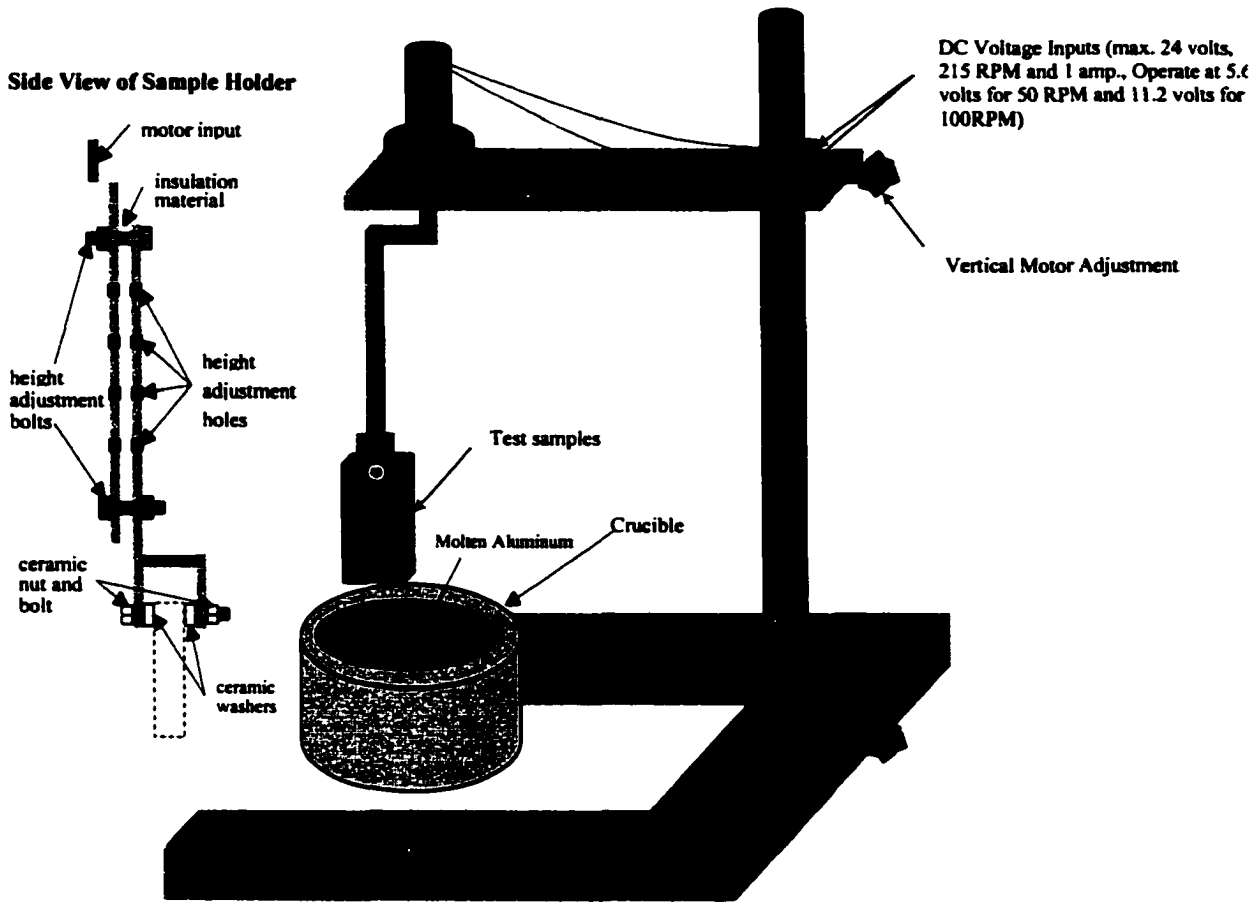

Figure 3.4. Experimental set-up for evaluating the corrosion/erosion properties of laser-processed and as-received samples of H13 steel

The tests were performed at temperatures of 670 °C and 800 °C, slightly higher than the practical temperature for use of H13 dies. In corrosion tests, the samples were left in the melt for up to 20 hours. After each test cycle, the samples were examined by use of optical microscopy and SEM for cracks, porosity, and other surface defects.

RESULTS AND DISCUSSION

Laser Glazing

For a given laser power, an increase in traverse speed produced more uniform, continuous glazed zones with fewer defects (microcracks, porosity, etc.). Similarly, for a given traverse speed, relatively low power (500 W) produced better quality. Of all the parametric combinations, a laser power of 500 W and a traverse speed of 127 mm/sec produced the best surface finish with the least defect. The surface roughness was 4 μm (R_a) for laser-glazed samples and 0.7 μm (R_a) for heat-treated and ground samples. These data are reproducible within an error bar of ± 5 %.

Figure 3.5 shows a schematic of the transverse profile of laser-glazed samples labeled with various dimensions. The penetration depth, H, was 0.65 mm (X = 0.3 mm) for the optimum parameters. The bottom zone, represented by Y, was not covered in the overlapping. The width, Z, was 0.37 mm, which provided an overlap of 30%. Overlapping in terms of width, Z, and distance of adjacent pass, A, is expressed as:

$$Overlapping = [(Z-A)/Z]*100\% \qquad (2)$$

Figure 3.6 is a scanning electron micrograph of the actual transverse section of a laser-glazed sample processed with the optimum conditions. Some inclusions are observed near the top surface. Figures 3.7(A) and (B) show the microstructures of the laser-glazed region and the substrate, respectively. It can be seen that the secondary carbides and grain structure in the glazed region are much finer and more uniform than in the substrate. Figure 3.8 shows the variation of microhardness (Vickers hardness indentations can be seen at the left end of Figure 3.6) with the distance from the surface. The surface layer was 30% harder than the substrate. This is attributed to the fine grains and fine secondary carbides that

increase hardening effects. The decrease in hardness with distance is believed to reflect the change in fineness of microstructures due to the lower cooling rates.

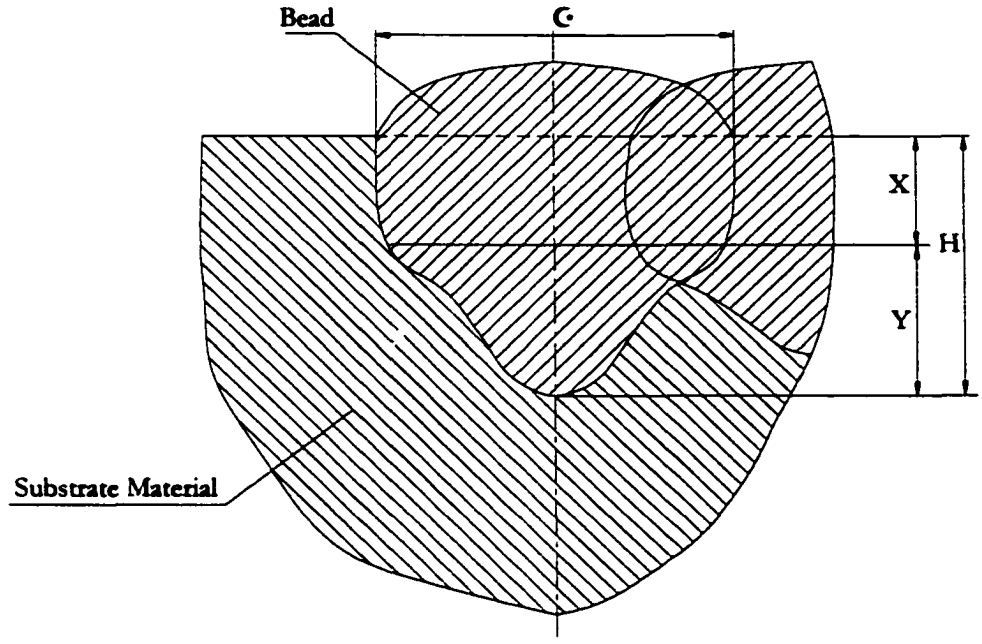

Figure 3.5. Schematic of the traverse section of laser glazed layers

Figure 3.6. SEM showing the transverse section of laser-glazed layers (laser power: 500 W, traverse speed: 127 mm/sec)

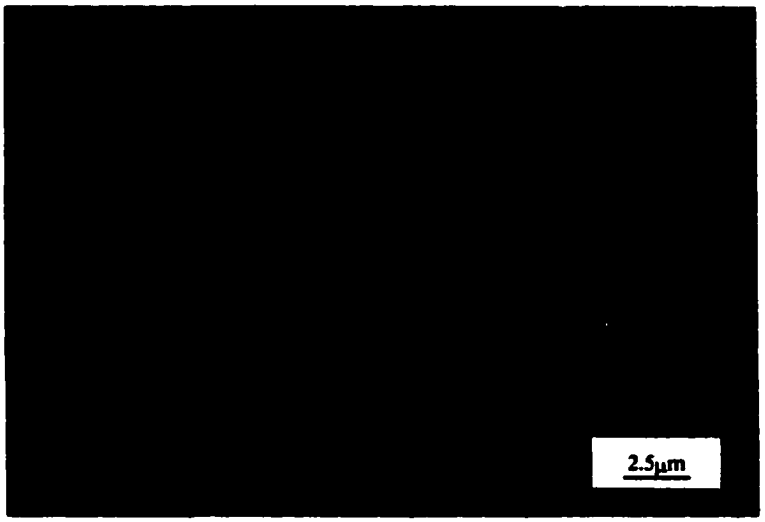

(A)

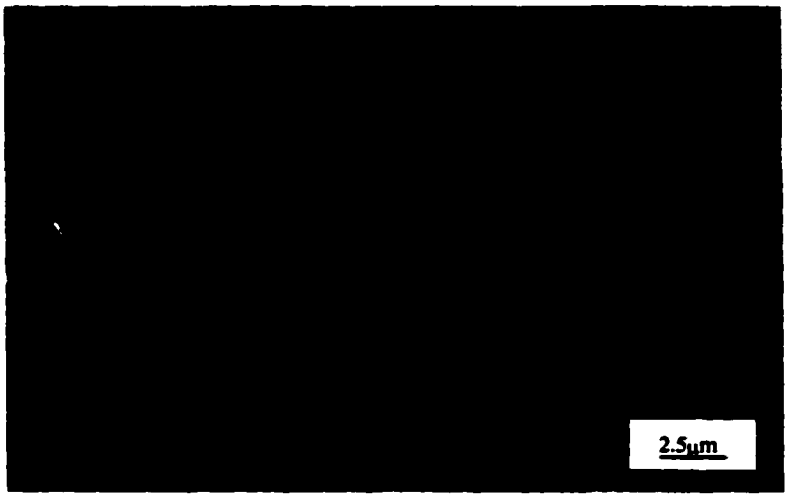

(B)

Figure 3.7. SEM showing microstructures of: (A) the laser-glazed zone; and (B) the substrate

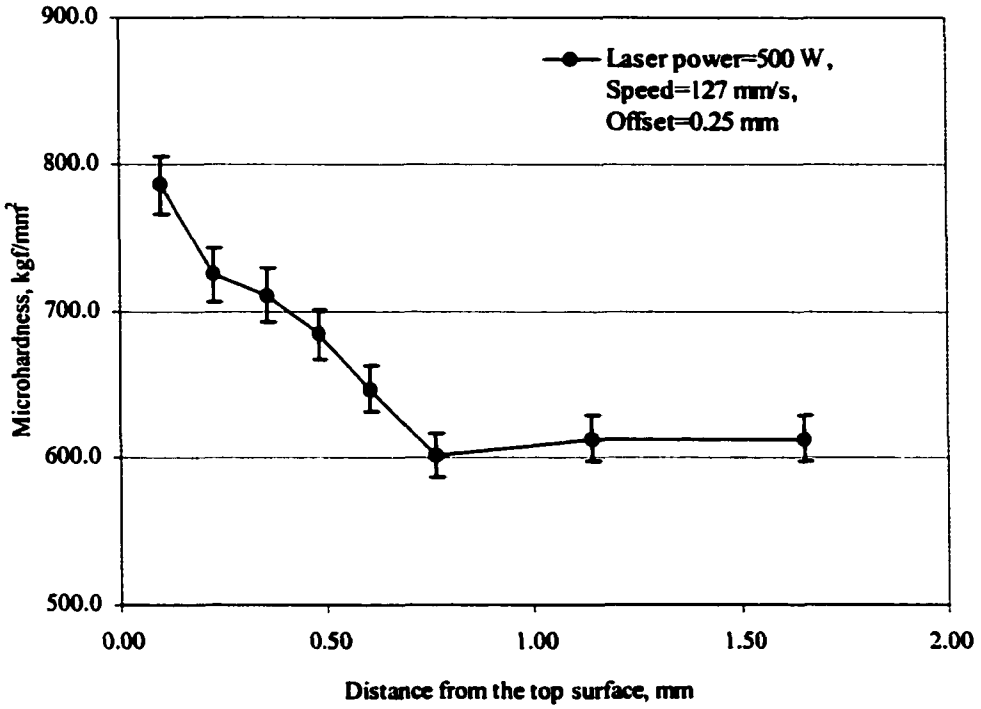

Figure 3.8. Vickers microhardness variation with the distance from the top surface

Laser Surface Alloying

Figure 3.9 shows the size (depth and width) of laser-alloyed zones produced in single-pass as a function of laser power for circular and linear beam profiles. The data represent the average value of six measurements. The variation was ±4%. As expected, there is an increase in size with laser power. However, the line beam, because of lower power density, produced thinner and narrower zones. In addition, the increase in depth and width with laser power are less pronounced for the line beam than for the round beam. The benefit of the line beam is its capability to produce superior surface quality (surface smoothness, absence of porosity/cracks, etc.) in laser-alloyed samples. Because the line beam is rectangular, with its long axis along its scanning direction, it preheats the substrate material and post-heats the

melted zone; both processes are effective in homogenizing the melt pool. In addition, the line beam results in a more uniform temperature distribution than the round beam along the scanning direction, leading to less thermal distortion.

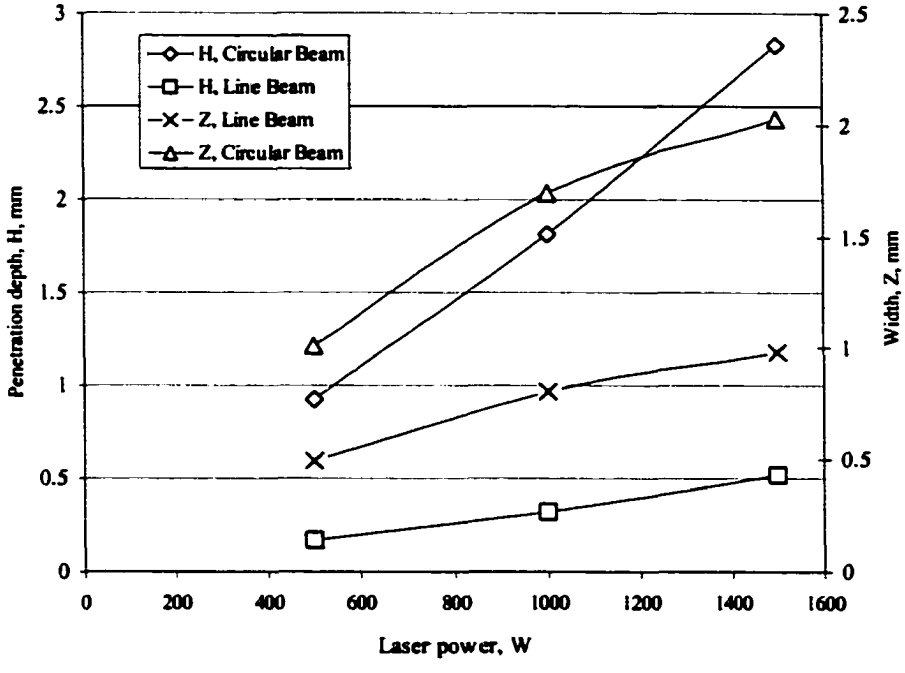

Figure 3.9. Penetration depth and width of alloyed zones at traverse speed of 21.2 mm/sec

The powder size had a strong influence on the surface quality of the pre-placed slurry layer and the laser-alloyed zone. Experiments indicated that 2 μm and 300 nm powders produced smooth pre-placed slurry surfaces because the fine powders are readily dissolvable in agar solution or alcohol to form the slurry. Table 3.5 shows the effect of powder size on the surface quality of laser-alloyed zones, demonstrating that fine powders are required to produce smooth surfaces. Table 3.6 shows the effect of traverse speed on the surface

roughness. The reason for the increased surface roughness at high speed (64 mm/sec) is that only the pre-placed layer was melted, with little bonding to the substrate.

Table 3.5. Effect of powder size on surface quality of laser-alloyed zones

Powder size (μm)	Surface roughness, R_a (μm)	Surface quality
30	15.6	Porosity and cracks.
2	8.9	Less porosity and fewer cracks.
0.3	5.7	Minimal porosity and cracks.

Table 3.6. Effect of transverse speed on surface roughness*

Traverse speed (mm/sec)	21	42.3	64
Surface roughness (μm)	11.8	8.9	16.5

* Laser power=500 W, powder size=2 μm, coating thickness=0.02 mm.

Dilution, defined as the change in composition of the surfaces by alloying of pre-placed coating, was estimated at 90% and above, using the following equation for the conditions used in this work.

Dilution = Area of melted substrate/(Area of coating layer + Area of melted substrate) (3)

Figures 3.10 and 3.11 are scanning electron micrographs that show the transverse sections of LSA for 2 μm and 300 nm powders, respectively. The penetration depth was about 13% larger for the powder of 300 nm because of its better absorption of laser energy.

The alloyed zone of the powder of 300 nm is nearly free from defects. Fine, uniform grain structures were observed in both cases. X-ray diffraction was performed to identify the phases formed during laser processing. Figure 3.12 shows the diffraction patterns of laser-glazed and laser-alloyed samples with TiC of particle sizes 2 μm and 300 nm. The laser-glazed sample exhibited a relatively strong α-Fe peak indicative of martensite. Laser-alloyed samples showed a strong presence of α-Fe and TiC. However, the intensity of the TiC peak is less for the sample alloyed with 300 nm particles, suggesting some dissolution of TiC.

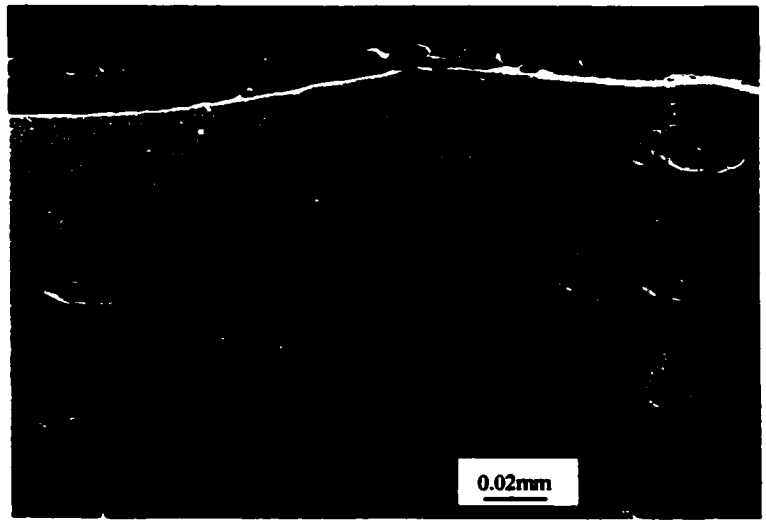

Figure 3.10. Scanning electron micrograph showing the transverse section of 2 μm powder alloyed zone

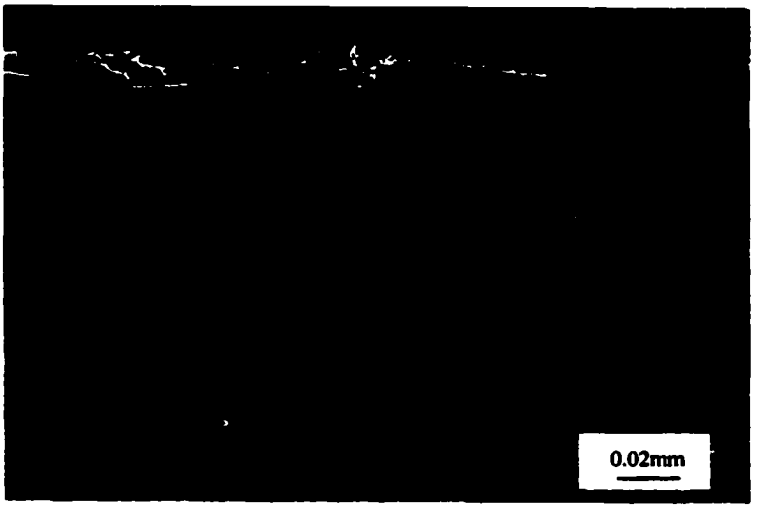

Figure 3.11. SEM showing the transverse section of 300 nm powder alloyed zone

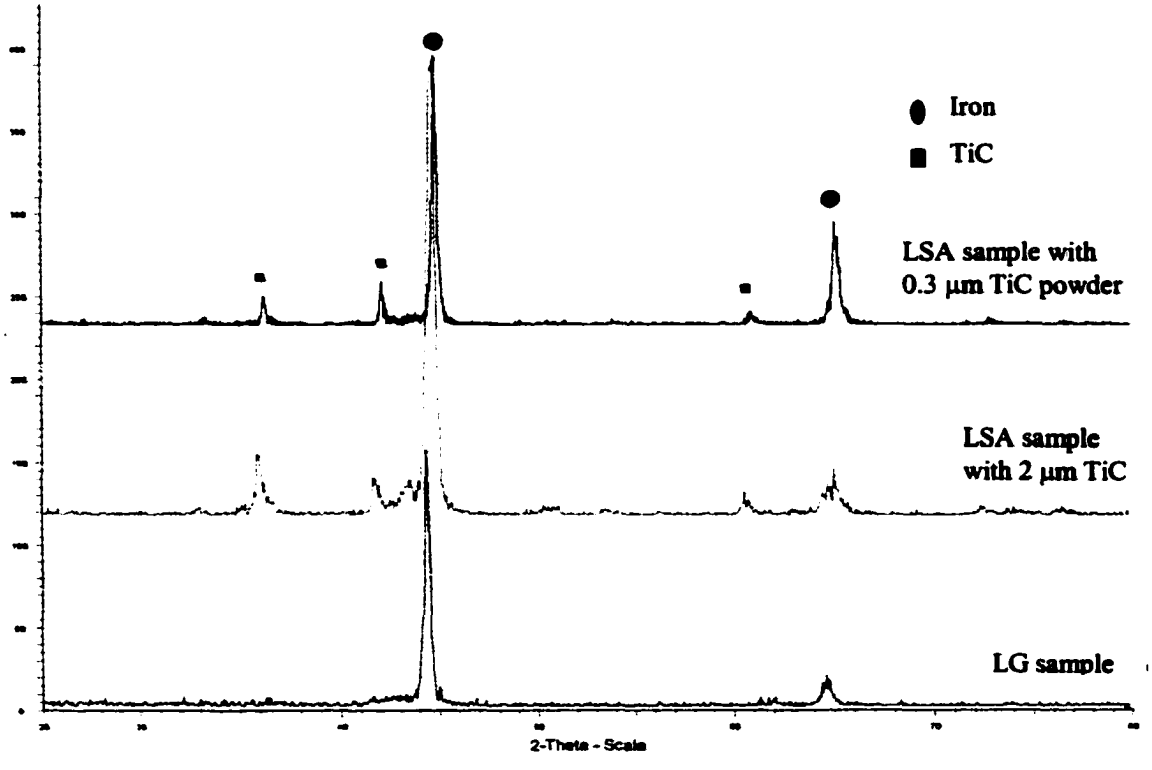

Figure 3.12. X-ray diffraction patterns of laser-glazed and -alloyed zones

Figure 3.13 displays the Vickers microhardness measurements in the laser-alloyed zones. The scatter in the data is less than 2%. For the 2-μm powder, the hardness of the surface layer was increased by more than 100% than that of the substrate and there is a decrease in hardness with distance from the surface. For the 300 nm powder alloyed zones, the hardness depth profile is reversed. Opposite to the hardness increase normally expected in the laser-alloyed zones, the hardness was reduced to 50% of the substrate for the 300 nm powder alloyed zone. This striking anomaly could not readily be explained from the microstructural information obtained in this work. Nevertheless, we believe that some amount of 300 nm powder might have dissolved in Fe during laser processing. Because titanium is a strong ferrite-former and prevents the formation of austenite, the phase transformation of austentie to martensite could not have occurred. Thus, the microstructure of 300 nm powder alloyed zones may consist of ferrite and TiC, whereas the 2 μm powder alloyed zones may contain martensite and TiC, which may explain the differences in hardness for these two cases.

Corrosion/Erosion Resistance

The corrosion/erosion resistance of laser glazed and alloyed samples were evaluated in simulated metal casting conditions. Figure 3.14 illustrates the corrosion resistance in terms of weight loss per unit area as a function of time in static melts for samples of as-received, laser glazed, LSA with 2 μm TiC powder, LSA with 2 μm TiC powder and tempered at 205 °C, and LSA with 300 nm TiC powder. The as-received specimens (blank) had much lower corrosion resistance because H13 steel can dissolve in aluminum melt to form multilayer intermetallic compounds Al_4FeSi [21]. Laser glazing had only a small

beneficial effect that could be attributed to the uniform dispersion of secondary carbides. A change in surface composition is certainly needed to obtain substantial improvements.

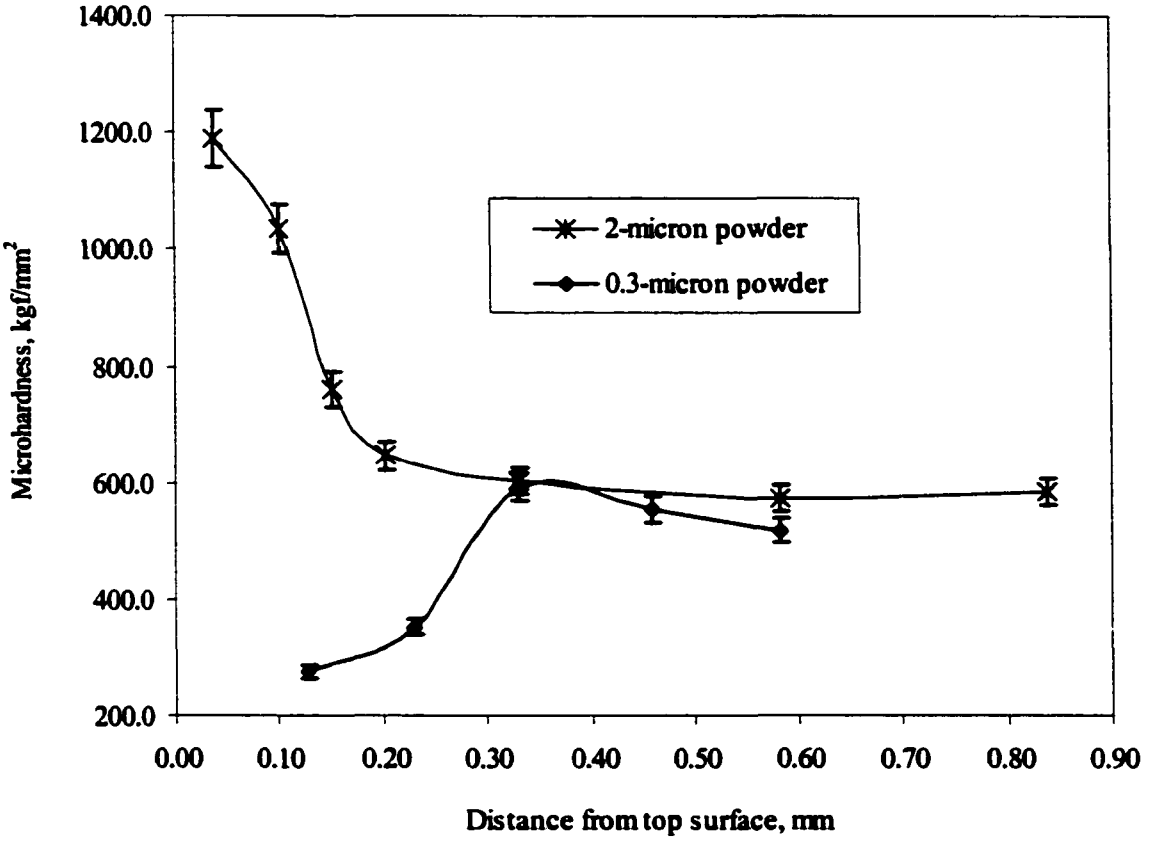

Figure 3.13. Vickers microhardness variation with the distance from top surface of LSA samples

Laser-alloyed samples with powder of 300 nm, and with powder of 2 μm followed by tempering provided the best corrosion resistance. The weight loss was decreased from 3500 mg/cm^2 to 500 mg/cm^2 by alloying the steel with nanocrystalline powder. This decrease in weight loss corresponds to an increase in corrosion resistance of about 85% for the laser-

alloyed samples. It is interesting to note that the samples laser-alloyed with 2 μm powder (without tempering) exhibited inferior corrosion resistance compared to samples alloyed with 300 nm powder. The improved corrosion resistance is attributed to the smooth surface, low porosity, and possibly ferrite microstructure achieved with the use of powders of nanocrystalline TiC. For the laser-alloyed samples with 2 μm powder and with tempering, their improved corrosion resistance may also be explained by the stress reduction and uniform morphology from the tempering process.

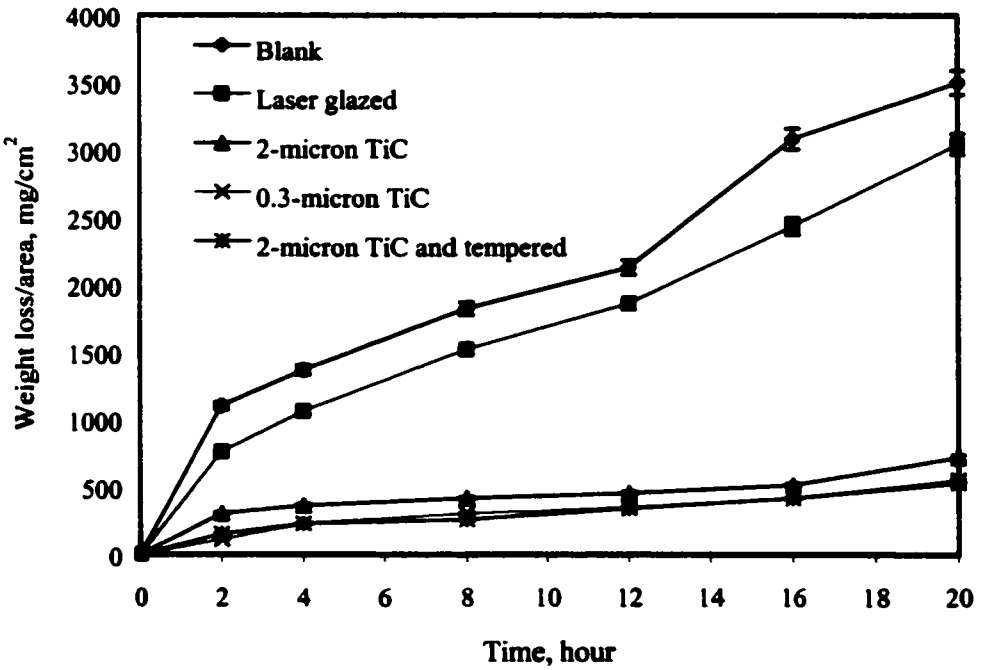

Figure 3.14. Weight loss of samples versus immersion time in static A390 melt (weight loss of untreated H13 steel: 3500 mg/cm^2)

The effect of melt flow on the die surface (erosion) was investigated by mechanically rotating the test sample, and evaluating the change in sample weight after a desired test time interval. Experiments were performed at temperatures of 670 °C and 800 °C at a rotation speed of 50 rev./min. The samples were tested for 3 hours; the results are shown in Figure 3.15. This plot indicates that under identical conditions, the alloyed samples with nano-sized particles exhibited improved erosion resistance, which could be attributed to the improved toughness associated with ferrite microstructure.

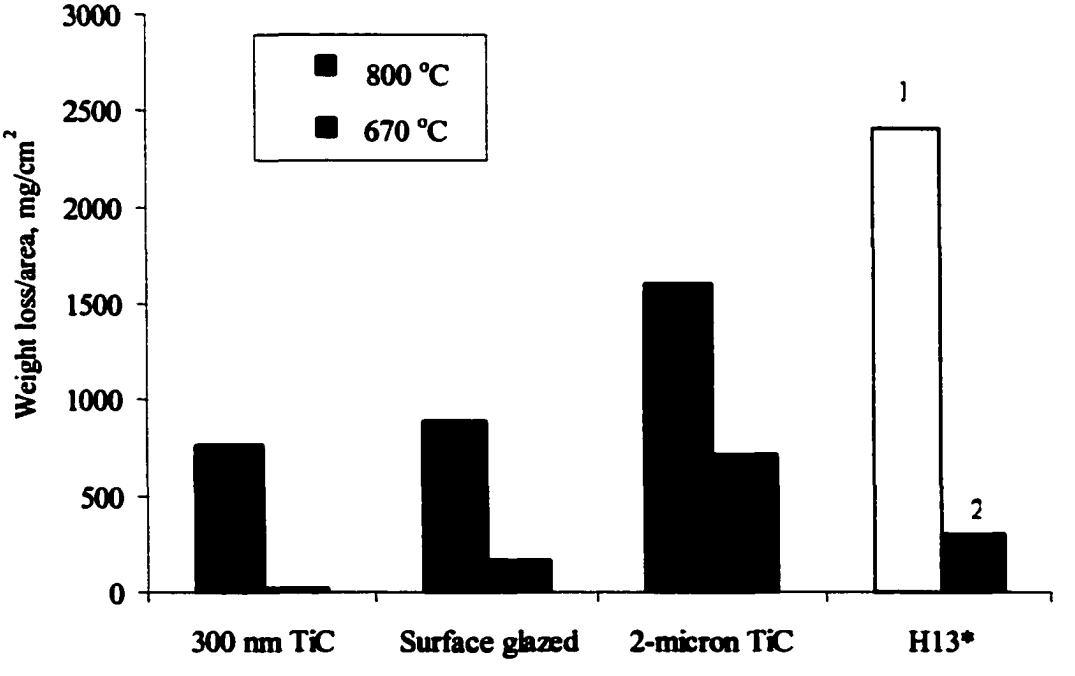

Figure 3.15. Weight loss due to erosion of samples at two different temperatures (* test temperatures: 670 °C and 735 °C for 1 and 2, respectively; test time: 4 hours; rotation speed: 50 rev./min; aluminum alloy of 10% Al and 10% Si [22])

A comparison of erosion rates at 670 °C and 800 °C shows that erosion rate increases with a rise in temperature. This can be attributed to the increased melt flow velocity at

higher temperatures, leading to rapid dissolution of intermetallic layers into the turbulent melt. The higher temperature also enhances the diffusion rate of Al, Si and Fe as well as the formation of intermetallic compounds such as τ_6, τ_5, and τ_2.

It is known that erosion is a progressive loss of material from a solid surface due to the mechanical interaction between that surface and an impinging metal fluid stream [20]. Erosion results in washout of the die surface. Damage due to erosion could be limited by using materials with higher toughness. Experiments performed in this research have demonstrated that laser alloying with nanocrystalline powders significantly improved erosion resistance.

CONCLUSIONS

Laser glazing and alloying of micro-and nano-particles of TiC on H-13 steel was performed to improve the performance and extend the life of die-casting dies subject to the harsh environment of repeated heating and cooling cycles. A 1.5 kW CO_2 laser was used to conduct the experiments. The criteria for optimum laser parameters were a smooth, flaw-free surface and surface integrity. The principal results and conclusions are:

1. For the glazing process, the optimum laser parameters were a focused circular beam with a laser power of 500 W and a traverse speed of 127 mm/sec. The penetration depth was 0.65 mm and the hardness was 30% higher than that of the heat-treated substrate.
2. For surface alloying, the optimum laser parameters were dependent upon the pre-placed powder thickness and size of the powders. High-quality surface layers were obtained when thinner coatings (0.02 mm) and finer powders (300 nm) were used.

3. For surface alloying, the optimum parameters were a laser power of 500 W, a line beam of 0.1 mm x 1 mm, and a traverse speed of 42.3 mm/sec. The penetration depth was 0.2 mm.
4. Hardness of laser-alloyed zones is dependent on the particle size. Micron-sized particles provided a hardness increase of more than 100%, but nano-sized particles reduced the hardness by 50%.
5. Nanocrystalline powder alloying caused a pronounced improvement in surface finish of alloyed layer and in resistance to corrosion and erosion.

ACKNOWLEDGEMENTS

Many thanks are due to Dr. Govindaraju, Karta Technologies Inc., for providing the steel samples, and Dr. Baburaj, the University of Idaho, for providing the nanocrystalline powder.

REFERENCES

1. North American Die Casting Association, Research and Development Report, 1995.
2. B. Pullen and V. Merchant, Industrial Laser Review, pp13-16, April 1996.
3. S. Chellapilla, R. Shivpuri, and S. Balasubramaniam, NADCA Sponsored Research; Coatings for Die Casting: A Comprehensive Review of Performance Evaluation including Current and Future Research, Paper T97-101, Transactions, NADCA 21st International Die Casting Congress, 1997.
4. K.R. Standford, The American Ceramic Society Bulletin, 74(9), pp 112-115, 1995.

5. H.M. Glaser, Thermal diffusion (TD) process, SME Technical Paper (Series), MF, SME, pp 1-6, 1993.

6. P.J. Blau (Ed.), Proceedings of the 11th International Conference On Wear of Materials, Wear, 203/204, pp 57-64, March 1997.

7. D.E. Semones and W.H. Safranek, Die Casting Engineer, 17(6), pp 12-18, 1973.

8. F.H. Loeffler, Surface and Coatings Technology, 68/69, pp 729-740, 1994.

9. Y. Wang, Surface and Coatings Technology, 94/95, pp 60-63, 1997.

10. U.K. Wiila, S.O.J. Kivivuori, J.M. Molarius, and M.S. Sulonen, Proeceedings of the 14th International Conference on Metallurgical Coatings, San Diego, CA, pp 213-220, March 1987.

11. J. Singh, Journal of Material Science, 29, pp 5232-5258, 1994.

12. J.W. Dini, Metal Finishing, pp 10-14, October 1997.

13. W.M. Steen and J.N. Kamalu, in: M. Bass (Ed.), Laser Materials Processing, North-Holland, Amersterdam, pp 83, 1983.

14. R. Dekumbis, Chemical Engineering Progress, December 1987, pp 25-30.

15. T. Oki, Corrosion Engineering, 39, pp 229-243, 1990.

16. M. Govindaraju and P.A. Molian, J. Material Science, 29, pp3274-3280, 1994.

17. R. Subramanian, S. Sircar, and J. Mazumder, Journal of Material Science, 26, pp 951-956, 1991.

18. J. D. Ayers, R. J. Schaefer and W. P. Robey, Journal of Metals, pp 19-23, August, 1981.

19. P.A. Molian, Material Science and Engineering, 58, pp 175-182, 1983.

20. E. G. Baburaj and F. H. Froes, Synthesis of metal, metalloid and mixed carbides by mechanochemical processing, Patent pending, 1998.

21. M. Yu, R. Shivpuri, and R. A. Rapp, Journal of Materials Engineering and Performance, 4(2), pp 175-181, April, 1995.

22. Staffan Malm, Jan Tidlund, Proceedings of the10th SDCE International Die casting Exposition & Congress, paper No.G-T79-051, 1979.

CHAPTER 4. LASER BASED FLEXIBLE FABRICATION OF FUNCTIONALLY GRADED MOLD INSERTS

A paper to be published in the International Journal of Advanced Manufacturing and Technology (in press)

Wenping Jiang and Pal Molian

ABSTRACT

A CO_2 laser-based freeform fabrication process with emphasis on difficult-to-shape and functionally effective materials was investigated with regard to fabrication of dies and molds. Square and circular molds were built by use of a material additive process of layers of TiC and Ni-alloy composite. The effects of laser processing on the quality, microstructures, and hardness of the molds were determined. Additionally, the molds' performance was evaluated in die-casting, injection molding, and in a thermal fatigue environment. The TiC core-Ni-alloy shell mold outperformed molds made of hardened H13 die steel, 304 stainless steel, and TiC-coated stainless steel in withstanding stresses and in retaining dimensional stability at elevated temperatures.

INTRODUCTION

The global market for dies and molds is estimated at 65 billion US dollars [1]. For die and mold makers to maintain their leading edge in this fiercely competitive market, they must utilize modern materials and fabrication technologies. Feasibility, cost, productivity and quality are important criteria that have to be considered when methods are chosen for manufacturing moulds and dies. Conventional processing of moulds and dies typically involves multiple steps ranging from CNC machining and heat treatment to surface coating.

Final shaping often relies on electrical-discharge machining (EDM) due to the requirements of highly dimensional accuracy and extremely good surface quality for moulds and dies [2]. However, EDM is a costly and time-consuming process. High on the die and mould makers' wish list are to produce functional parts of good quality directly from computer geometric data (CGD) and to shorten lead-time by near-net-shape processing. Lasers have emerged as superb tools in cutting, joining, and various rapid prototyping technologies [3]. Using lasers can be an efficient mean of realizing flexible manufacturing processes for moulds and dies due to its flexibility of integration with computers and robots. A laser-based flexible fabrication process, designated as LBFF, could make functionally graded metallic parts and facilitate the reduction of process time. The LBFF is a computer integrated, numerical-controller guided, beam-shaped laser cladding (LC) process that uses a high power CO_2 laser to melt and solidify powders fully from the ground up in thin horizontal layers and to build free-standing structures. It is different from other LC-based rapid prototyping processes (Table 4.1) in that the LBFF process uses shaped laser beams that can produce layers of improved surface finish, dimensional tolerance and reduced dilution among the functional layers. The shaped laser beam has a reduced temperature gradient in both laser scanning direction and its transverse direction, and reduced heat conduction losses significantly; it preheats the powder at the leading edge, facilitating even melting and smoother flow of molten puddle. Although studies on the fabrication of metal parts using LC-based rapid prototyping technologies have been reported [4-9], few results have been published on use of a laser-based process to fabricate mold inserts from functionally graded materials.

Table 4.1. LC-based rapid prototyping processes

Name	Process characteristics
Laser Engineered Net Shaping (LENS, Sandia National Laboratory) [3]	– Nd:YAD laser; – Powders delivered through a concentric nozzle with laser beam; – Enclosed envelop for fabrication.
Direct Metal Deposition (DMD, University of Michigan) [4]; Precision Optical Manufacturing (POM, Precision Optical Manufacturing Co. Inc) * [5]	– CO_2 laser; – Powders delivered through a concentric nozzle with laser beam; – Height sensor control.
Laser Direct Casting (LDC, University of Liverpool) [5]	– CO_2 laser; – Powder delivered through a nozzle from one side.
Direct Light Fabrication (DLF, Las Alamos National Laboratory) [6,7]	– Nd:YAG laser; – Powder delivered a concentric nozzle with laser beam.
Shaped Deposition Manufacturing (SDM, Stanford University) [8]	– Nd:YAG laser; – CNC milling (a hybrid process).

Table 4.1. (continued)

High-power Laser Based Fabrication Procress (The Pennsylvania State University) [5]; Lasform™ (AeroMet Corp.) [5, 9]	– CO_2 laser; – Powder delivered through a concentric nozzle with laser beam.

*The equipment is based on DMD, University of Michigan [5].

Die and mold inserts are generally made of hardened steels, cast irons, and superalloys. The properties required for mold and die materials are 1) high strength; 2) high wear resistance; 3) moderate to high toughness; 4) low friction; 5) chemical inertness; 6) thermal shock resistance; and 7) corrosion resistance. Because all these properties are seldom realized in a single material, it is essential that new strategies, other than application of a coating on die surfaces be developed to meet those functional requirements. This work utilized an approach that involved functionally graded materials (FGMs) to improve the performance and life of dies and molds. A functionally graded material is a combination of two or more materials in which a gradual transition exists at their interface. With a gradual transition, combinations of properties on opposing surfaces can be obtained without any "weak link". Some examples of FGMs are ZrO_2/Ni-Cr, stainless steel/zirconia, and Inconel/steel [10]. In the present work, TiC/Ni-Cr-Al-Co-Y_2O_3 was selected as the combination that meets most of the property requirements.

The LBFF processing, characterization, and functional testing of FGM mold inserts were investigated in detail to demonstrate the benefits of the process and material for enhancing performance in die-casting dies and injection molds. Because the LBFF is a

material additive process, it could also be used effectively in mold and die repair, surface modification, and coatings.

MATERIALS AND EXPERIMENTAL PROCEDURES

Material Selection

Powder materials used in making functionally graded parts, must have the desired mechanical and thermal properties. In addition, they must be thermally compatible to prevent initiation of cracks. Based on these criteria and the application requirements for dies in die-casting and molds in injection molding, TiC powder with a nominal size of 2 μm and Ni-Cr-Al-Co-Y_2O_3 (Ni-alloy composite) with a nominal size of 100 μm were selected. TiC, one of most commonly used materials for coatings, has excellent physical properties. It has a thermal expansion coefficient (TEC) of 7.0×10^{-6} $^{\circ}C^{-1}$ [11] and has superior resistance to abrasive wear and corrosion when used as coating [12,13]. Ni-alloy composite powder is a high-temperature material that has very good corrosion resistance and moderate wear resistance [14]. Its thermal expansion coefficient of 14.5×10^{-6} $^{\circ}C^{-1}$ is close to that of H13 die steel [11]. However, it has much higher thermal conductivity than H13 die steel. The TiC was procured from Alfa Aesar® and the Ni-alloy composite powder was obtained from Sulzer Metco®. Table 4.2 gives the nominal composition of the Ni-alloy composite powder. AISI 304 stainless steel was used both as the supporting material and as material for injection molds for comparison. Hardened H13 die steel was chosen as the baseline for comparison in die-casting and thermal fatigue tests, because it is widely used as the die steel in aluminum

die casting. It has a hardness of 46-48 HRC after heat treatment. The temperature and time used for hardening H13 die steel are provided in Table 4.3.

Table 4.2. Nominal chemical composition of the Ni-alloy composite powder

Element	Ni	Cr	Al	Co	Y_2O_3
Weight (%)	Balanced.	17.5	5.5	2.5	0.5

Table 4.3. Temperature and time used for hardening H-13 die steel

Procedures	Stress relief	Vacuum air hardening	Tempering I	Tempering II
Temperature (°C)	537	1024	537	537
Time (h)	0.5	1.5	3	3

The LBFF Process

The LBFF process uses a high-power CO_2 laser to melt the powder delivered by inert gas in the laser-material interaction zone and builds rapidly solidified structures in near fully dense and near-net-shape layer by layer. A schematic of this process is shown in Figure 4.1. It starts with a 3D solid model, a geometric representation of designed molds or dies. CAD/CAM software is then used to slice the 3D model at Z direction and to transfer the 3D model into 2D "blocks" of typical thickness 0.2 mm~0.3 mm. From these, CNC codes, such as those used in the pocket milling process, are created. The codes are then used to direct the laser beam scanning in a raster pattern within the boundaries defined by the slices. The

motion of the substrate in the X- and Y- directions, in combination with the motion of the optics in the Z direction, allows the generation of arbitrary 3D structures. The feedstock could be wire or powder. Wire is relatively easy to feed but often difficult to obtain in the required chemical composition. Powder is much easier to procure and can be fed into the interaction zone either by pre-placing it or delivering it directly. However, control of the delivery rate of the powder is critical. The detailed powder calibration is listed in Appendix A. The powder not melted by the laser beam can be collected and reused, reducing the waste of material and reducing damage to the environment. A continuous wave (CW) CO_2 laser with power output up to 2000 W was used in this work because of its high power and its Gaussian beam profile, which can focus the beam to a small spot size.

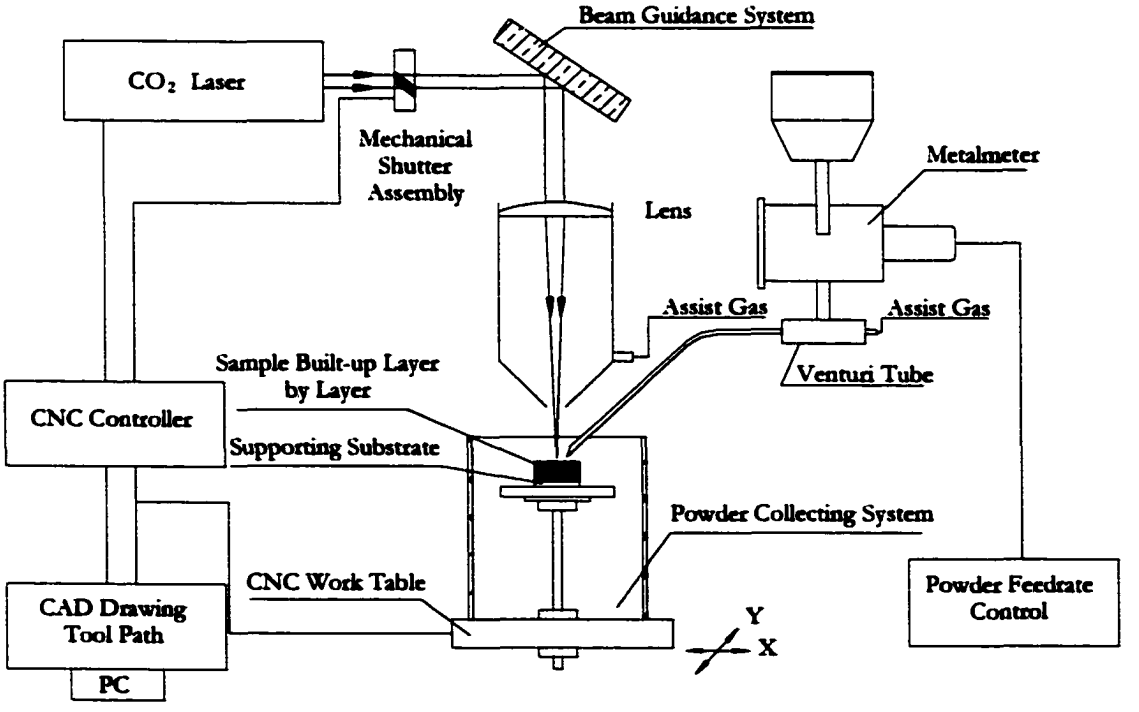

Figure 4.1. Schematic diagram showing the setup for the LBFF process

Deposition of the Ni-alloy composite powder

In this fabrication process, the laser beam was directed to the 304 stainless steel surface by means of a lens with a focal length of 190 mm. The beam was defocused by 6.4 mm below its focal point to avoid laser-cutting mode. The beam diameter at the sample surface was 0.5 mm. Power density was about 4.1×10^5 W/cm^2, which is close to the value recommended for metal melting [15]. The Ni-alloy composite powder was transported to the interaction zone by a nozzle with argon, which was also used as a shielding gas, from the side. The deposition thickness for each Ni-alloy powder layer was approximately 0.25 mm. The powder feed rate was adjusted by the powder delivery motor speed. The laser beam scanned the substrate according to the profiles and tool paths obtained by use of CAD/CAM software. Table 4.4 lists the laser parameters and processing variables for the process that creates layers of good surface finish and high quality.

Deposition of the TiC powder

Because TiC powder readily 'boils" at elevated temperatures, thus producing a rough surface during the deposition process, a diffused rectangular beam generated by a cylindrical-spherical lens with a focal length of 127 mm was used. The beam was focused on the substrate surface and had a spot size of 0.1 mm ×1 mm. A rectangular beam, which generates temperature gradient profiles that different from those of a circular beam for a given power, is beneficial in forming a uniform and smooth TiC layer. The power density for this process was 5×10^5 W/cm^2. Because of its cubic crystal structure and fine particle size, the TiC powder was difficult to deliver through a nozzle with the existing setup. Hence, it was placed on the substrate before being subjected to laser melting. The incremental layer thickness of

TiC, 0.1 mm, was controlled by use of a weighing device with an accuracy of 1/1000 gram. Argon was used as a shielding gas to prevent the TiC from decarburization. The laser parameters and processing variables for the TiC powder are given in Table 4.5.

Table 4.4. Laser parameters and processing variables for deposition of the Ni-alloy powder

Laser power (W)	800
Beam geometry	Circle
Beam mode	TEM_{00}
Focal position	6.4 mm above
Scanning speed (mm/sec)	5.0
Powder feed rate (g/min)	17.5
Stand-off distance (mm)	13.0
Assisting gas flow (l/s)	0.078
Distance between adjacent passes (mm)	0.25

Characterization and Hardness Testing

A surface profilometer with a 0.025 mm diamond probe was used to measure the surface roughness (arithmetic average, R_a) of the fabricated parts in both the longitudinal and transverse directions. This value was then used to determine the need for post-processing. The fabricated parts were polished, etched in a solution of nitric acid, acetic acid, hydrochloric aid and glycerin, and then examined under an optical microscope. Scanning

electron microscopy (JEOL JSM35, 10 kV) was also used to characterize the profile, flaws, and microstructures of the graded layers. Parts were evaluated by means of Vickers microhardness test with a diamond pyramid indenter at a load of 1 kgf.

Table 4.5. Laser parameters and processing variables for deposition of the TiC powder

Laser power (W)	500
Beam Geometry	Rectangle
Beam mode	TEM_{00}
Focal position	Surface
Scanning speed (mm/sec)	50.8
Stand-off distance (mm)	2~3
Assisting gas flow (l/s)	0.12

CNC Machining

A CNC mill was used to remove the supporting material (304 stainless steel) on the fabricated parts and to cut pockets on as-received 304 stainless steel, hardened H13 die steel, so that the molds could be used for casting and injection molding tests. Because of the high hardness at the interface between the 304 stainless steel support and the fabricated layers, carbide-milling bits and CAP® magic cutting fluids were used. All parts were cut using the same cutting parameters.

Functional Testing

Die casting of aluminum alloy

Shell molds cut from the fabricated FGM (Ni-Cr-Al-Co-Y_2O_3+TiC), laser coated 304 stainless steel (TiC as coating), as-received 304 stainless steel, and the hardened H13 die steel blocks were used as dies for pouring 319 aluminum alloy. More than 100 castings with pouring temperatures above 1033 K were produced in the dies.

Injection molding

The FGM and the laser-coated, as-received 304 stainless steel mold inserts of zero taper angle were used for injection molding to determine mold relief ability, presence of macro-defects, ability to resist stress deformation. A Boy 30M injection molder was used for the injection process. Polystyrene was the injection material. The inserts were so configured that each insert was the same distance from the sprue hole, to negate the effect of pressure differences along the distance on stress deformation (Figure 4.2). Moreover, the bottoms of the inserts were supported only on their edges so that the deformation could be produced under injection pressure because of a wall thickness of 1 mm for all three inserts. Details on the design of the connecting blocks for this process can be found in Appendix B. A Brown & Sharpe coordinate measurement machine (CMM) was then used to measure the extent of deformation. Injections were restricted to only 25 due to the difficulty in relieving the injected blocks from the inserts. The injection temperature and pressure were set to 210 °C and 100 bars, respectively.

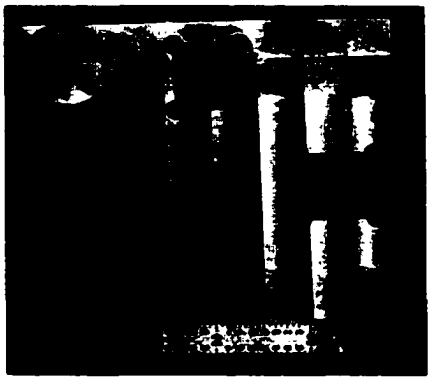

Figure 4.2. Mold inserts configuration for injection molding process

Low-cycle thermal stress fatigue tests

Thermal fatigue tests on the FGM mold insert, laser-coated 304 stainless steel and the hardened H13 tool steel mold inserts were performed by alternately immersing them into a heated furnace for a preset time and then dropping them into a water sink. The furnace was set to temperatures of approximately 650 °C and 960 °C. All the mold inserts had the same geometry and were tested under the same conditions. Before being tested, the inserts were visually examined for any cracks by use of a microscope with ×20 magnification. The inserts were then checked for crack initiation with cycle intervals of 5, 10, 15, 20, 25, 35 and 50. The cycle at which crack initiation occurred was the governing criterion for thermal fatigue.

RESULTS AND DISCUSSION

Analysis of Molds Fabricated with Ni-Alloy Composite Powder

Figure 4.3 shows a circular mold and a square mold fabricated by use of the LBFF process in 10 and 15 passes respectively. The circular mold has a diameter (D) of 25.4 mm.

The square mold has a side length (L) of 19 mm. Both have a wall thickness of 1.2~1.5 mm. The wall thickness, which is affected by beam diameter, laser power and pressure of shielding gas, can vary from about 1.0 mm to 3.0 mm in the LBFF process. The ratio of height to width for a single pass is about 0.2, which results in good bonding and minimum dilution. The surface roughness (R_a value) is about 200 μm. Visual examination revealed some partially melted powder particles "suspended" on the walls; the thickness was greater at the beginning and ending regions of laser irradiation than elsewhere. The partially melted particles result in the rough surfaces and possibly the non-uniformity of the wall thickness of the parts as well. The thickness buildup could be remedied by leaving a gap half as wide as the scanning width between the starting and ending point [16]. A post surface finishing process is recommended for the LBFF process. Optical microscopy did not reveal any porosity and confirmed near fully dense parts.

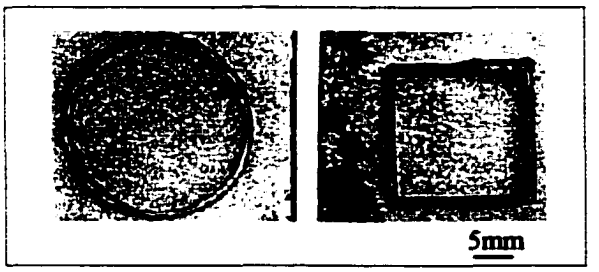

Figure 4.3. Circular (D=25.4 mm, h=2.4 mm) and square (L=19.0 mm, h=3.5 mm) molds made by the LBFF process (laser power=800 W, speed=5 mm/s)

Analysis of Layers Fabricated with TiC Powder

The crucial aspect of deposition of TiC powder is its surface roughness, which greatly affects the later addition of the Ni-alloy composite powder layer. If the surface roughness of

the built TiC layer exceeds 50 μm, the added Ni-alloy composite powder layer will create significant surface waviness. For powder processing, the surface roughness of one layer could be propagated to another layer and even amplified [10]. Experiments indicated that a thin layer of TiC powder (<0.1 mm) built up each time produced a smooth surface. Surface roughness (R_a value) measurements on the TiC layer along the longitudinal and the transverse directions did not differ significantly. The built-up layers had a surface roughness (R_a value) less than 20 μm. Optical microscopy results showed that the built TiC layer was fully melted and there were only minor inclusions in the solidified layer (Figure 4.4). Scanning electron microscopy (SEM) analysis revealed the presence of some micro-cracks in the layer (Figure 4.5). The micro-cracks could have been produced by stresses during the rapid cooling that followed solidification. Crack initiation sites could be reduced or even eliminated by improved processing together with use of fine and spheroidized carbide particle [17]. Vickers microhardness measurements on the deposited layer provided an average hardness value of 1475 HV, almost 20% higher than the reported microhardness value for TiC layers. The increase in hardness may be explained by TiC particle size differences and the possible formation of titanium nitride during the deposition process. The layers exhibited the light golden color characteristic of TiN.

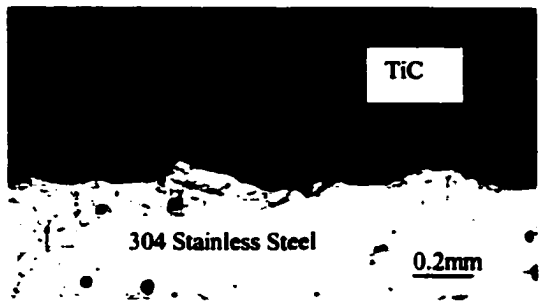

Figure 4.4. Optical microscopy showing the transverse section of fully melted TiC layer (thickness: 0.5 mm)

Figure 4.5. SEM showing the microcracks and solidification fronts (×1000) in the TiC layer

Analysis of Block Fabricated with Ni-Alloy Composite Powder Layer onto TiC Powder Layer

Figure 4.6 shows the fabricated FGM block with multiple layers, outer layers of Ni-Cr-Al-Co-Y_2O_3 and inner layers TiC. Four passes per side produced a layer thickness of

approximately 1mm. Some inclusions in the fabricated layers were observed. Surface roughness (average value, R_a) was 10 μm. A difference of approximately 25% existed between R_a values for the laser beam scanning direction and those for the perpendicular direction, due to solidification front effects. Optical microscopy indicated good bonding between the TiC powder layer and the Ni-alloy powder layer. Higher power and lower scanning speed were used for deposition of Ni-alloy composite powder than for deposition of TiC powder. Re-melting of some TiC due to the deposition of Ni-alloy composite powder eliminated the inclusions observed in TiC (Figure 4.7). SEM showed that dendrite structures were present in both Ni-alloy and TiC layers. In the Ni-alloy layer, the dendrites were well formed and oriented (Figure 4.8), which indicated that cooling of the molten pool had proceeded non-uniformly. The dendrites in the TiC layer were not fully developed (Figure 4.9). The average arm spacing between secondary dendrites in the TiC layer is about 3.5 μm, while spacing for the Ni-alloy composite layer is 7.0 μm. Based on the secondary dendrite arm spacing, the cooling rates for the Ni-alloy layer and TiC layer are found to be on the order of 10^2 K/s ~10^3 K/s. These cooling rates are pretty high in comparison to the cooling rates obtained from conventional methods, but they are typical in laser material processing. Figure 4.10 shows Vickers microhardness values vary with the distance from the FGM block surface. The Ni-alloy layer had an average hardness value of 583 HV, which was close to the hardness of the hardened H13 die steel, while the TiC layer had an average hardness value of only 260 HV, almost the same as that of the supporting material. The average microhardness value in the interface region was between those of the two layers. This type of hardness profile is desired for most mold parts, especially for mold cores, because high surface hardness and acceptable toughness are desired mechanical properties. The large reduction in

microhardness of the TiC layer in the FGM part was attributed to its decarburization during the re-melting process during deposition of the Ni-alloy layer. This conclusion was based on the elemental analysis of energy by the energy dispersive spectrum (EDS), which indicated diffusion of carbon into the Ni-alloy layer from the TiC layer (Figure 4.11).

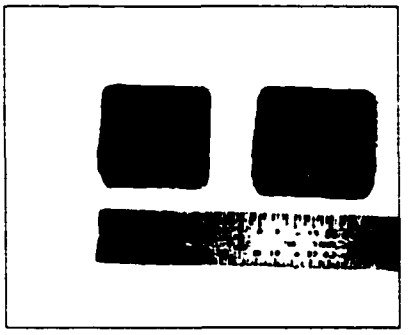

Figure 4.6. Photograph showing the fabricated blocks by the LBFF process

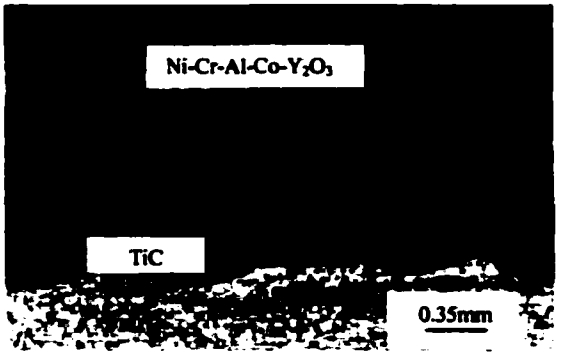

Figure 4.7. Optical micrograph shows the structures of the layers of TiC and Ni-alloy

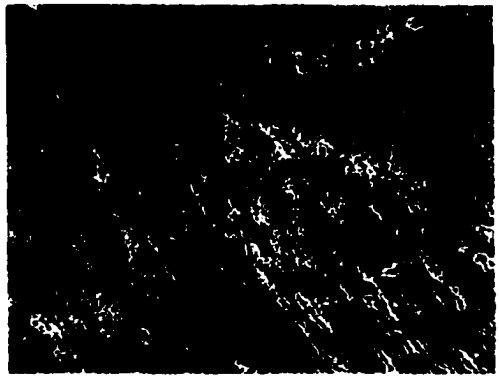

Figure 4.8. SEM showing the formation of dendrites in the Ni-alloy layer

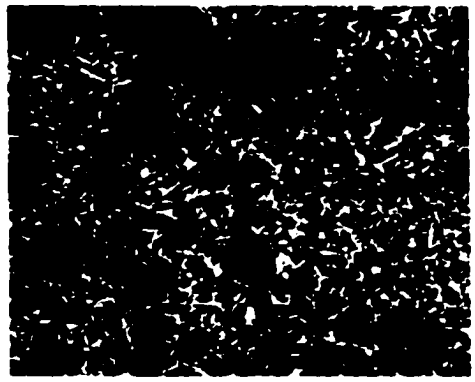

Figure 4.9. SEM micrograph showing the formation of dendrites in TiC layer

Performance Evaluation

The performance of mold inserts was evaluated in die-casting, injection molding, and a low-cycle thermal fatigue environment. For the purpose of discussion, all the mold inserts are classified as shown in Table 4.6. Their surface roughness (R_a value) and surface microhardness (Vickers, with a load of 1 kgf) are also given in the table. The FGM mold

inert has a microhardness close to the hardened H13 die steel, however, it has a much rough surface, indicating the necessity of some post processing.

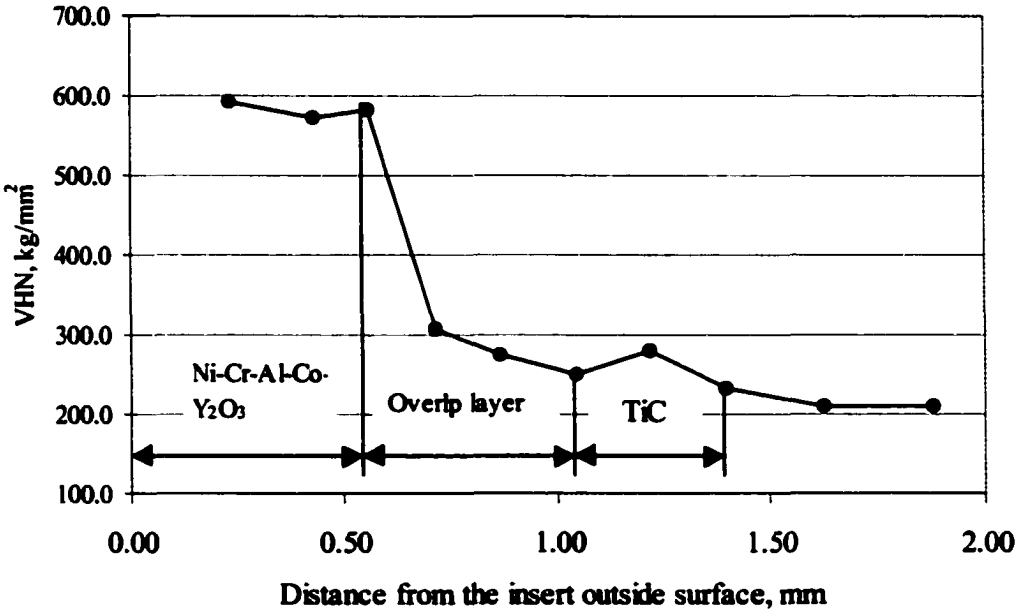

Figure 4.10. Vickers microhradness variation with the distance from the insert surface

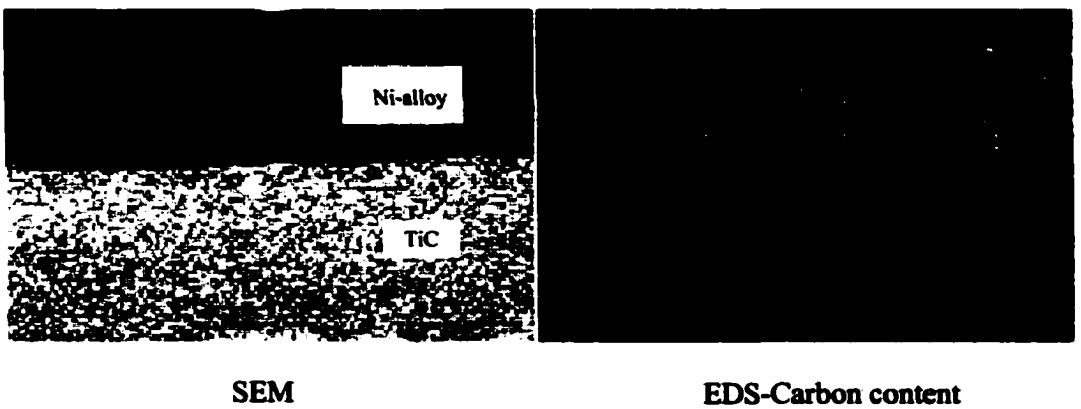

Figure 4.11. SEM micrograph and carbon content variation

Table 4.6. Classification of mold Inserts for performance evaluation

Mold insert	Materials	Surface microhardness (kg/mm^2)	Surface roughness (μm)	Evaluation tests
A	As-received 304 stainless steel	220	4.5	Injection molding
B	Hardened H-13 die steel	570	1.0	Die casting, thermal fatigue
C	Laser-coated (TiC) 304 stainless steel	1400	20.0	Die casting, injection molding, thermal fatigue
D	FGM (TiC+Ni-Cr-Al-Co-Y_2O_3)	583	10.0	Die casting, injection molding, thermal fatigue

Aluminum alloy casting

Inserts B, C and D were used as shell molds for aluminum alloy casting. Over 100 pieces of 319 aluminum alloy blocks were cast. There was no difficulty in removing the castings from the molds, although the cavities had zero draft angles. There were no significant differences among the cast 319 aluminum alloy blocks poured in these molds. Repeated expansion and contraction during the casting process due to thermal cycles did not cause the cavities to deteriorate, suggesting that a more severe test was needed for

comparison purposes. This test was intended as a functionality check rather than as a means comparison between parts.

Injection molding

Injection molding test to examine easiness of mold relief and the inserts' ability against stress deformation was performed on mold inserts A, C and D. Test showed that the injected polystyrene blocks were not easily removed from the cavities because of zero relief angles of the cavities. In total 25 shots were made. CMM measurements on the deformation at the inserts' bottom displayed that, up to 25 shots, the plastic deformation at the mold inserts A, C, and D was not discernible. The negligible deformation happened on these three inserts indicated that insert D, made by the LBFF, had at least as much ability to resist deformation under pressure with 25 shots as did insert A, which was made of as-received 304 stainless steel. If the injected blocks are relieved easily from the inserts, injection molding could be an effective way to examine the wear resistance of the mold inserts of different materials under given test conditions. In this study, there was no discernible effect on the mold inserts from the injected material due to the low abrasive characteristics of polystyrene used in injection and the small number of shots.

Low-cycle thermal fatigue test

For molds used in injection and die-casting processes, thermal fatigue is the most common failure mode due to exposure of such parts to varying temperatures and stresses. Because thermal fatigue is related not only to the material and test conditions, but also to the specimen geometry, a temperature cycle may produce different stress cycles. For

comparison, inserts B, C, and D were tested under the same test conditions and with the same geometry. The inserts were first subjected to temperature cycles ranging from 20 °C to 650 °C. Insert C had cracks on the TiC coating side when the number of cycles was 10, whereas inserts B and D did not show any crack initiation up to 35 cycles. The early occurrence of cracks on insert C was expected because of pre-existing defects and possible residual stresses related to the processing of TiC and the lower fatigue strength of stainless steel 304. Inserts B and D were then tested at temperature cycles ranging from 20 °C to 960 °C. At this elevated temperature, the onset of deformation of insert B was unexpectedly observed when the number of cycles was five; the deformation became more severe as the number of cycles increased (Figure 4.12). Crack initiation occurred on insert B after 30 cycles. Although insert D had cracks in the TiC layer when the number of cycles was 17, it did not show any evidence of deformation (Figure 4.12). In addition, more oxide scale was observed on insert B than on insert D, indicating that insert B was more susceptible to cyclic oxidation. Table 4.7 gives the results of low-cycle thermal fatigue tests. The significant differences in deformation behavior between inserts B and D indicate that insert D has higher strength at elevated temperatures. The greater strength may be attributed to the presence of 0.5% Y_2O_3 in the Ni-alloy composite and to the laser processing. The existence of Y_2O_3 in the metal matrix acts to pin down the dislocation motion and extends the performance of the Ni-alloy. Laser processing can maintain the fine size of the dispersoids without agglomeration because of its ability to purify the Y_2O_3 particles and redistribute them more uniformly because such particles absorb more laser energy than the surrounding matrix does [18]. The content of nickel and chromium, and the adhesion of the chromium oxide (Cr_2O_3) scale due to the homogeneous distribution of the Y_2O_3 dispersoids, may explain that insert D is low

susceptibility to cyclic oxidation [19]. Differences in crack patterns and thermal cycles between inserts B and D could be attributed to the differences in sensitivity to stresses and ductility of the materials. The extended performance of insert D at elevated temperature can be useful in aluminum die-casting and plastic injection molding.

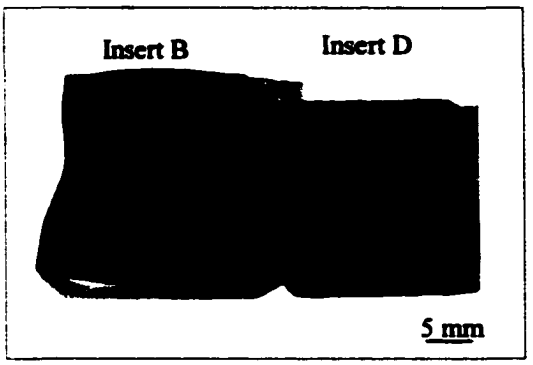

Figure 4.12. Photograph showing the deformation of mold inserts after the thermal fatigue test

Table 4.7. Thermal fatigue test results for mold inserts B, C, and D

Mold Insert	Stage I[1]	Stage II[2]
B	35 cycles without any deformation and crack initiation	Deformation started at cycle 5 and cracks occurred at cycle 30
C	10 cycles with crack initiation	N/A
D	35 cycles without any deformation and crack initiation	No evidence of deformation. Crack initiation at cycle 17

(1) The inserts were alternatively immersed in a heated furnace of 650 °C for 3 minutes and dropped in water of room temperature to finish one cycle.

(2) The inserts were alternatively immersed in a heated furnace of 960 °C for 2 minutes and dropped in water of room temperature to finish one cycle.

CONCLUSIONS

A LBFF process was successfully developed to build up overlap layers, using TiC powder and Ni-Cr-Al-Co-Y_2O_3 composite powder. Based on the investigation of the fabricated inserts, the principal conclusions are as follows:

(1) The process can be used to fabricate functional parts with any materials suitable for laser cladding.

(2) The insets have high surface hardness and expected toughness, which are suitable for mold and die applications.

(3) The fabricated inserts have been tested functionally with the 319 aluminum casting process and the polystyrene injection molding process; tests indicated that the inserts made by the LBFF process could be used for functional purposes with minimum post-processing.

(4) Low-cycle thermal fatigue tests indicate that the laser-fabricated FGM insert has higher strength and improved dimensional stability at elevated temperatures than the hardened H13 die steel insert. However, the thermal fatigue resistance of the hardened H13 die steel insert is slightly better than that of the laser-fabricated FGM insert. The high strength and dimensional stability of the FGM insert at elevated temperatures could be explained by the presence of 0.5% Y_2O_3 in the Ni-alloy composite and by the benefits of laser processing.

ACKNOWLEDGMENTS

Many thanks are due to Larry Couture for providing the CNC machine and assisting in conducting the experiments.

REFERENCES

1. http://www.modernmachineshop.com/articles/hsm9801.html. (date accessed: May 20, 2000)
2. K. Stoeckhert (ed), Mold-Making Handbook for the Plastic Engineer, Hanser Publishers, Munich Vienna New York, 1983.
3. N.B. Dahotre (ed), Laser in Surface Engineering, ASM International®, pp xiii-xvi, 1998.
4. J. Mazumder, J. Choi, K. Nagarathnam, J. Koch, and D. Hetzner, The Direct Metal Deposition of H13 Tool Steel for 3-D Components, Journal of Metals, pp. 55-60, May 1997.
5. R. Irving, Taking a Powder- Metallurgy and Lasers Are Cooking up New Methods for Manufacturing, Mechanical Engineering, pp. 55-59, September 1999.
6. G.K. Lewis, Direct Laser Metal Deposition Process fabrication Near-Net-Shape Components Rapidly, Materials Technology, 10, pp. 51-54, 1995.
7. J.O. Milewski, G.K. Lewis, D.J. Thoma, G.I. Keel, R.B. Nemec, and R.A. Reinert, Direct Light Fabrication of a Solid Metal Hemisphere Using 5-axis Powder Deposition, Journal of Materials Processing Technology, 75, pp.165-172, 1998.
8. M. Binnard, Design by Composition for Rapid Prototyping, Kluwer Academic Publishers, Boston, 1999.
9. D.H. Abbott and F.G. Arcella, AeroMet Implementing Novel Ti Process, Metal Powder Report, 53(2), pp. 24-26, 1998.
10. A. Ghosh, Y. Miyamoto, I. Reimanis, and J.J. Lannutti (ed), Functionally Graded Materials: Manufacture, Properties, and Application, The American Ceramic Society, 76, pp 171-174, 1997.

11. http://www.handyharmancanada.com/TheBrazingBook/comparis.htm. (date accessed: May 20, 2000)

12. J.D. Ayers, Wear Behavior of Carbide-Injected Titanium and Aluminum Alloys, Wear, 97, pp. 249-266, 1984.

13. A.G. Grigoryants, Basics of Laser Material Processing, Mir Publishers, Moscow, 1994.

14. http://www.sulzermetco.com/products/material/mt_nick.html. (date accessed: December 15, 2000)

15. J. Mazumder and O. Conde, R. Villar, and W. Steen (Ed.), Laser Processing: Surface Treatment and Film Deposition, Kluwer Academic Publishers, 1996.

16. E.W. Kreutz, G. Backes, A. Gasser, and K. Wissenbach, Rapid Prototyping with CO_2 Laser Radiation, Applied Surface Science, 86, pp 310-316,1995.

17. J.D. Ayers and T.R. Tucker, Particulate-TiC-Hardened Steel Surfaces by Laser Melt Injection, Thin Solid Films, 73, pp. 210-207, 1980.

18. P.A. Molian, Y.M. Yang, and P.C. Patnaik, Laser Welding of Oxide Dispersion-Strengthened Alloy MA 754, Journal of Materials Science, 27, pp. 2687-2694, 1992.

19. G.H. Gessinger, Powder Metallurgy of Superalloys, Butterworth & Co. (Publishers), 1984.

CHAPTER 5. PRODUCTION OF ALUMINUM EXTRUSION DIES USING A LASER- BASED FLEXIBLE FABRICATION TECHNIQUE

A paper to be published in the Transactions of North American Manufacturing Research Conference 2002 (in press)

Wenping Jiang, Michael Stock, and Pal Molian

ABSTRACT

Laser-Based Flexible Fabrication (LBFF), a solid freeform fabrication (SFF) method based on laser cladding process, was investigated with regard to production of aluminum extruding dies. Laser melting the powder materials, delivered by a quasi-axial nozzle, and building the solidified material layer-by-layer directionally, generated the die. The design of the nozzle and the die is discussed, as well as problems of processing. The effects of laser processing on hardness and microstructure of die material are determined. Using the surface roughness along the peripheral direction and the roundness of the extruded bars as criteria, the functionality of the die was evaluated in an aluminum cold-extrusion process. The die was found to have nearly theoretical density, acceptable surface roughness, and hardness being close to that of wrought and heat-treated (as-quenched) H-13 steel. The directional effect associated with lateral powder delivery on nonuniformity of thickness was eliminated. Results of extrusion tests suggest that post-finishing be essential for preparing industrial tools by use of LBFF.

INTRODUCTION

Demand for extruded aluminum is increasing because the extruded aluminum offers designers and manufacturers the choices and combinations of useful characteristics unmatched by many other materials [The Aluminum Association, 1995]. Extruded aluminum often has the "product" advantages of varied surface finishes and precise tolerances that are determined by the design of tooling and the selection of die materials. Hardened medium alloy steel (AISI grade A) and chromium-based steel (AISI grade H) are the preferred die materials for cold extrusion and hot extrusion, respectively [Kalpakjian and Schmid, 2001]. Despite recent advancements in die design and in the fabrication process, dies of great complexity usually could not be perfected in one design iteration. Products often have to go through several trail-and-error procedures to introduce the necessary corrections into the die's geometry [Misiolek *et al.*, 1999]. Because the corrections are manually finished, it is difficult to trace the modifications to the original designs of the dies as well as to update the die design for future applications. In addition, the high hardness (above 55 HRC) of the dies restricts the fabrication process to sink EDM or high speed machining (CNC with diamond tooling), which is costly and time consuming.

The freedom to create complex geometry by use of the solid freeform fabrication process allows for production and modification of the dies with updated data for future designs and with no special requirements as to tools. Case studies demonstrate that SFF could save time and cost (as much as 50%) compared to conventional fabrication methods [CAD/CAM Publishing, 1991-1996].

LBFF is a solid freeform fabrication process, based on the principle of laser cladding of metals, for rapid production of three-dimensional parts directly from computer models

[Jiang and Molian, 2001]. Laser scanning a series of two-dimensional slices or layers sequentially creates a solid object. The fabrication of each layer includes introduction of powder materials continuously and uniformly to the top of the built-part and directional scanning of the part. As a rapid prototyping technique, the LBFF offers benefits such as reduced lead-time, improved quality and lower cost.

In this work, material and processing issues of LBFF related to production of aluminum extrusion dies are investigated. In addition, the experimental results of cold-extrusion tests on LBFF dies are presented.

EXPERIMENTAL PROCEDURE

Materials

AISI H13 powder of size 70-100 μm was chosen as the material for production of the dies, for three reasons: 1) Direct metal deposition of H13 powder has been used for producing injection molding dies and other 3D components [Mazumder *et al.*, 1997]; 2) H13 steel powders flow consistently during laser processing and show mechanical properties equal or superior to those of wrought H13; and 3) H13 steel is the material of choice for the die and tooling industries [Budinski, 1996; Smith, 1993]. The H13 steel powder was procured from Crucible Research, a division of Crucible Materials Corporation. Table 5.1 lists the nominal chemical composition of the H13 powder. Hot-rolled AISI 1020 steel was used as the substrate on which successive layers of H13 steel were built. The powder delivery rate was calibrated before and after the fabrication process to ensure quantitative consistence of powder flow (Appendix A).

Table 5.1. Nominal chemical composition of AISI H13 steel powder

Cr	V	Mo	Si	Mn	C	Fe
5.23	0.96	1.43	1.01	0.39	0.39	Bal.

The LBFF Process

Figure 5.1 shows the schematic setup for the LBFF process, which uses a continuous wave CO_2 laser with a rated power of 1500 W to melt the powder on the substrate, with little dilution. The laser beam was defocused at 16 mm (5/8 in.) above its focal point. Argon was used as a carrier gas and as a shielding gas. The laser beam was made to scan the substrate in the *XY* plane to form a layer, and then moved up in the *Z* direction to a distance of the layer thickness, so as to start another new layer.

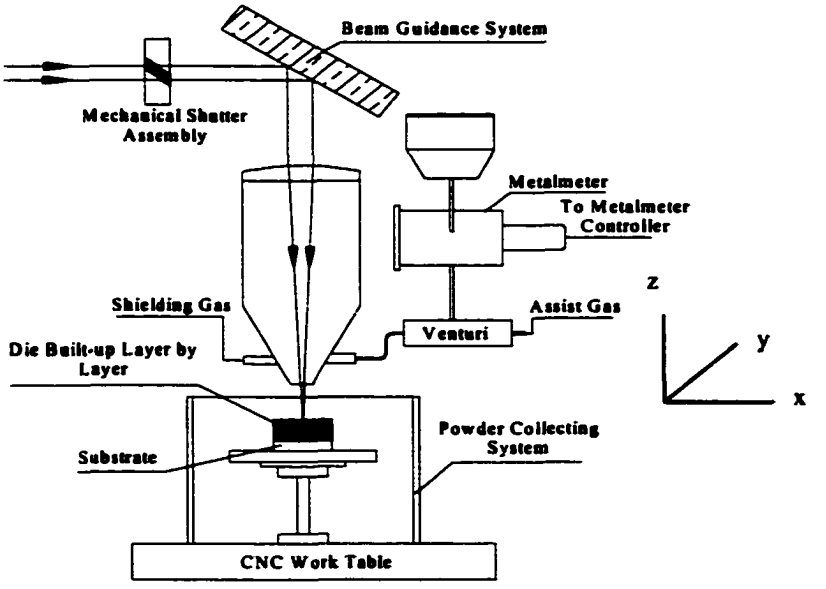

Figure 5.1. A schematic setup for the LBFF process

Design of the Nozzle

Lateral powder-delivery systems have been widely used in laser surface alloying and laser cladding [Kawasaki *et al.*, 1992; Yellup, 1995]. For linear tracks, a lateral powder-delivery system can usually provide depositions of high quality (smooth surface, uniform thickness, and few defects). However, it is often not easy to achieve complex geometry and thicker sections by use of a lateral powder-delivery system, because of the directional effect of the carrier gas used in powder delivery. In addition, the critical requirement of the alignment of the side-delivered powder and the laser beam suffers. Furthermore, utilization of powder was inefficient. Consequently, a new nozzle (Figure 5.2) for quasi-coaxial powder delivery was designed in an effort to improve the fabrication process.

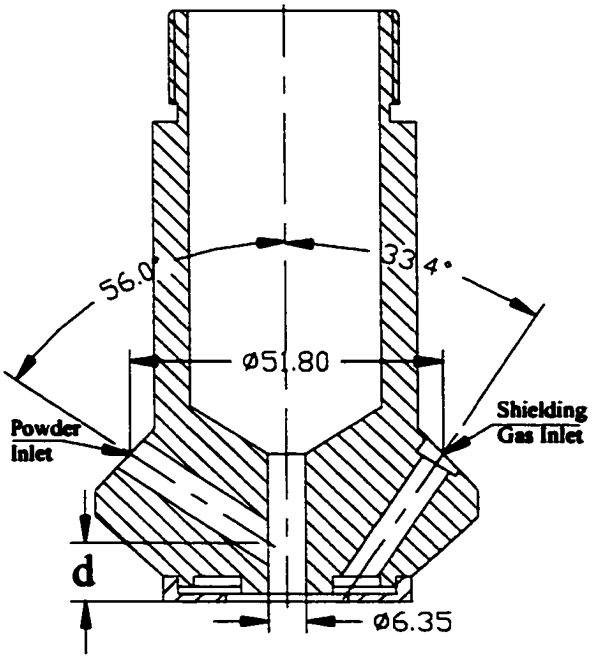

Figure 5.2. A quasi-coaxial nozzle design for the LBFF (all the dimensions are in mm)

The new nozzle has the advantage of delivering the powder uniformly and in a quasi-coaxial manner with a laser beam, so that preheating of powder is better achieved. Preheating the powder is known to assist in forming smooth melt track [Hu *et al.*, 1998]. The assist gas, entering from the hole configured opposite to the hole for powders, can form a circular shield that effectively protects the preheated powder and molten pool from the oxidizing environment. This also helps prevent contamination of the powder materials.

Die Design

A ring-shaped geometry was chosen for the aluminum extrusion die design. An inside taper of 11.78° (relief angle) was designed to facilitate removal of the extruded part. The large taper imposes a stringent requirement for the die to withstand compressive and shearing forces during the extrusion process. The ring geometry (Figure 5.3) consists of a cylindrical block with a circumscribing circle diameter (CCD) of 12.5 mm, outside diameter of 31.8 mm, and height of 10.0 mm. The die was designed for a low extrusion ratio, A_0/A_f, of 4.0.

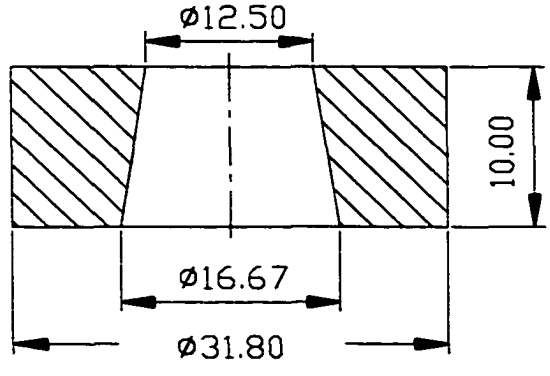

Figure 5.3. A schematic of die geometry (all the dimensions are in mm)

Characterization and Hardness Testing

A surface profilometer with a 0.025 mm diameter diamond stylus was used to measure the arithmetic average value, R_a, of the surface roughness. Metallography characterization of the top and transverse sections was performed by sectioning, polishing and etching the dies in a 4% nitric acid solution. Scanning electron microscopy (JEOL JSM35, 10kV) was then used to investigate the microstructures of the dies. Hardness along the periphery of the die was measured by use of the Rockwell C scale and a Wilson/Rockwell Series 500 tester. Certified calibration blocks verified the hardness measurements.

Cold Extrusion of Aluminum

Cold extrusion was chosen for study of the performance of LBFF dies because it often is a combined operation of indirect extrusion and forging, and exerts large stresses on the tooling. In addition, it has offers good control of surface finish and dimensional tolerances. Tests of aluminum cold extrusion to check the functionality and accuracy of the extruding dies were executed on a SATEC material testing machine using dies fabricated by the LBFF technique, as shown schematically in Figure 5.4. The billet, 25.4 mm in diameter, was made of 1100 aluminum alloy. Molybdenum disulfide was used as lubricant. The surface finish and dimensional accuracy of the extruded bars were then compared to those of extruded bars from machined die (CCD=12.5 mm) made of AISI 4340 steel because of unavailability of H-13 steel.

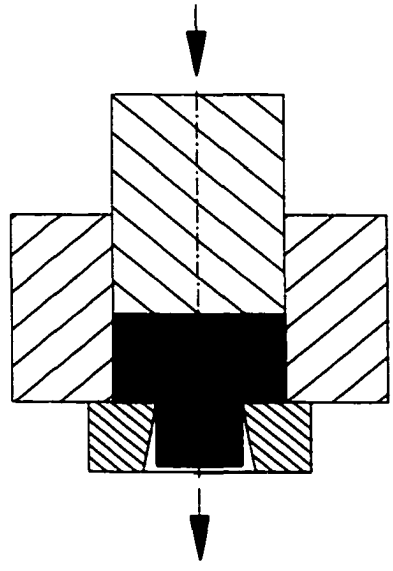

Figure 5.4. A schematic showing the cold extrusion process

RESULTS AND DISCUSSION

Energy Balance Analysis

The process parameters such as laser power, scanning speed, powder flow rate, etc., have major effects on the quality of fabricated parts [Mazumder *et al.*, 1999]. For example, the thickness and quality of the deposited layer in each laser pass can be controlled by tuning the laser power and by changing the scanning speed (or dwell time of the beam on the material). Another set of variables that can significantly affect the microstructure and properties are powder size, flow rate and composition. Sophisticated models based on the solutions of heat conduction and mass transport equations are available for laser cladding [Chande and Mazumder, 1985; Yevko *et al.*, 1998]. Simplified theoretical models for laser cladding and laser surface alloying with direct powder injection have also been developed

and successfully applied in optimizing of process parameters [Picasso *et al.*, 1994; Bamberger *et al.*, 1998].

In this work, we have applied an energy balance model to estimate the laser power necessary for providing smooth surfaces and minimal dilution among layers. The laser power is more important than other parameters because it must be high enough to melt the delivered powder fully but low enough to minimize dilution, improve bond strength, and obtain the best possible surface finish. According to published work [Steen *et al.*, 1986], scanning speed has little effect on the dilution between layers. It must be realized that the LBFF technique is a layer-by-layer technique of building parts; integral bonding among layers is essential to secure the strength of parts for which a suitable laser power is most appropriate.

The basic energy balance for laser melting a powder layer is:

$$Q_S \leq Q_R \tag{1}$$

where Q_S is the energy supplied per unit time, W, and Q_R is the required energy to melt the powder, W.

Energy supplied is calculated as:

$$Q_S = P(1-r)\phi \tag{2}$$

where P is incident laser power, W; r is reflectivity of the metal (r=0.9) [Steen, 1998]; and ϕ is a coefficient covering the effect of the powder stream, which can be calculated as 0.81 [Bamberger, 1998].

Energy required is calculated as:

$$Q_R = M(C_p \Delta T + L_f) + Q_L \tag{3}$$

where M is mass rate of the deposition material, kg/s; C_P is specific heat of the material, J/kg.K; ΔT is temperature rise from initial temperature to melting point, K; L_f is latent heat of fusion of the metal, J/kg; and Q_L is heat losses due to conduction, convection and radiation, W. Introducing powder catchment efficiency, η_{Cat}; energy utilization efficiency, $\eta=(Q_R-Q_L)/Q_R$; and powder feed rate, m, and rearranging equation (3), we have:

$$\eta Q_R = m\eta_{Cat}(C_P\Delta T + L_f) \tag{4}$$

Powder catchment efficiency, determined experimentally, is defined as the mass ratio of powder entrapped by the molten zone to total powder delivered. Considering a powder feed rate of 0.128 g/s and powder catchment efficiency of 5%, and using the thermophysical properties of carbon steel (0.4% carbon) as an approximation to those of H-13 powder material, an incident laser power of 485.4 W was calculated. This corresponds to a power of 540 W at the laser head, which theoretically ensures that zero dilution occurs among layers.

To produce scanning tracks of acceptable surface quality, thermal evaporation from the surface must be prevented. Thermal diffusion modeling of laser cladding process showed that the depth of melting is given by following equation [Bamberger *et al.*, 1998]:

$$\Delta Z = 2\sqrt{\frac{\alpha d}{V}\ln(\frac{T}{T_m})} \tag{5}$$

where α is thermal diffusivity, m^2/s; d is beam diameter, m; V is scanning speed, m/s; $T_m < T < T_b$; T_b is the boiling temperature, K; and T_m is melting temperature, K. T is controlled by the laser power. For the beam diameter and scanning speed chosen for this work, the maximum melt depth allowed based on equation (5) would be 0.75 mm for H13 steel. Within this thickness limit, the surface roughness is approximately linear to the thickness of the deposited layer [Mazumder *et al.*, 1999].

The actual melt depth in this study was only 0.2 mm (because the laser power was low), which suggests that the surface temperature during laser melting was well below the boiling temperature. Smaller melt depth guarantees a good surface finish.

Overlap also affects surface roughness. Its determination is associated with the dimensions of molten pool, which can be computed by a solution to an analytical model based on the superposition of moving Gaussian beams (Appendix C). Table 5.2 gives the process parameters chosen for the die fabrication process.

Table 5.2. Process parameters for the die fabrication

Laser power (W)	550
Scanning speed (mm/sec)	8.5
Powder Feed Rate (g/min)	7.69
Overlap (%)	25
Layer Thickness (mm)	0.2
Carrier Gas (l/min)	2.36 (5 CFH)
Shielding Gas, P_g (kPa)	280

Die Geometry, Surface Finish and Solidification Structure

Figure 5.5 shows a photograph of an extruding die fabricated on a substrate without any post-processing. It has tapers both inside and outside. The inside taper was intentionally made for ease of removal of the extruded part. However, the outside taper was generated as

the result of shrinkage in the solidification process. Introducing a "compensation" offset in CNC programming can eliminate the outside taper.

Figure 5.5. Photograph showing a die fabricated on AISI 1020 substrate

More success was obtained in the present work than in previous works with respect to uniformity of wall thickness. This is a direct effect of the quasi-coaxial nozzle specially designed for this fabrication process. The wall thickness variations in previous work are due to the directional effect associated with the lateral powder delivery practice.

Visual examination of the die revealed excessive material deposition at the program starting point. This was attributed to the intrinsic nature of CNC processing, in which the beam was programmed to move inward or outward for an increment after it finished a circle at a given position. The sudden change in moving direction made the beam dwelling longer than at other points, which produced thicker layers. Two techniques can be used to correct this unevenness: shifting the point to different peripheral positions and surface grinding.

Surface roughness measurements showed an arithmetic mean value, R_a, ranging from 12.5 μm to 50 μm (commercial dies of 25 mm in CCD, R_a, 0.8~1.0 μm) [Matsushita, 1990;

Kalpakjian and Schmid, 2001]. It was observed that when the height of the die was less than 5.0 mm, the process gave a surface roughness less than 10.0 μm.

Optical and scanning electron microscopy/energy dispersive X-ray examination of the die did not reveal defects such as porosity, inclusions, and unmelted powder, which implied that the LBFF process produced a die with near-theoretical density. Fig. 5-6 shows the microstructures observed on both circular sections (top surface) and axial cross sections (transverse to the wall thickness). The average grain size is 10 μm (equivalent to ASTM Grain Size # 10) as shown in Figure 5.6 (A). Development of very fine grains in LBFF is an expected result of rapid solidification. The axial cross section of the entire die thickness exhibited three zones: deposited zone, re-melting or interface zone, and heat-affected zone (HAZ). The deposited zone, shown in Figure 5.6 (B), constituting more than 90% of height, has a higher rate of cooling than the other two zones, and so has much finer microstructures. Equiaxed dendrites dominated this region. A transition from equiaxed grains to columnar grains (Figure 5.6 (C)) was observed in the re-melting zone. The columnar structures have coarse grains due to repeated heating from the deposited layers, and consequent growth of the existing grains. The columnar structures are aligned in the die built-up direction, which corresponds to the direction of maximum temperature gradient during cooling.

(A)

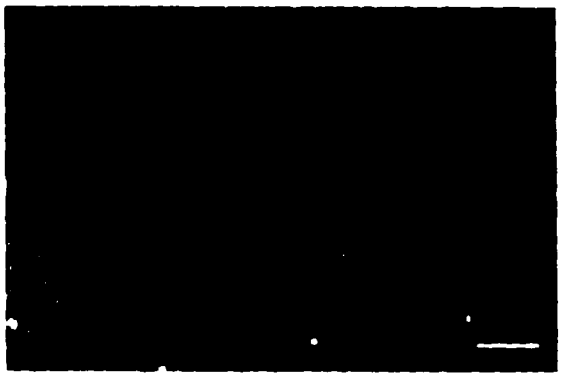

(B)

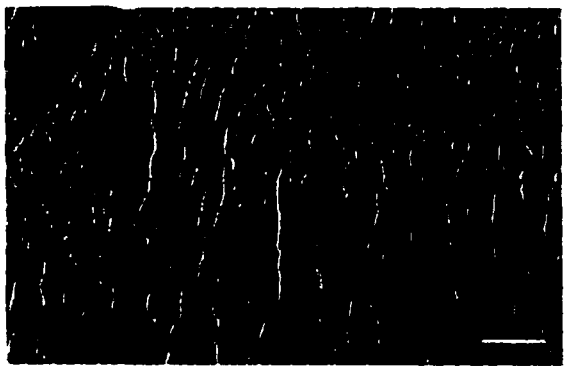

(C)

Figure 5.6. SEM micrographs showing the microstructures of the die: (A) grains on the circular section (top); (B) equiaxed dendrites in the top and middle regions of the axial cross section; (C) microstructure transition zone close to the substrate of the axial cross section. (etchant: 4% nital)

Hardness Profile and Microstructure

As shown in Figure 5.7, the hardness in the peripheral direction ranged from 45 R_c to 56 R_c, which is close to the typical hardness values of wrought H-13 tool steel (40~53 R_c) and as-quenched H-13 tool steel (50~54 R_c) [Davis *et al.*, 1990]. Hardness measurements on the top and bottom surfaces revealed no discernible differences, consistent with the uniformity of microstructure along the axial direction.

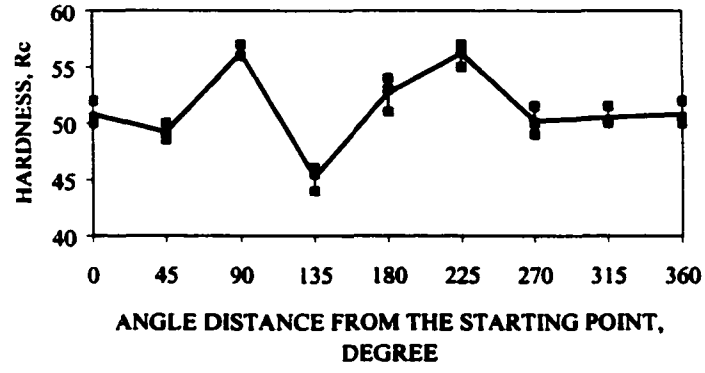

Figure 5.7. Hardness profile along peripheral direction of the die

An SEM micrograph of representative microstructure is shown in Figure 5.8 (A), in which the structure consists of fine spheroidal carbides (white spots) uniformly distributed in a matrix of martensite. The precipitation hardening effect caused by tempering of martensite can be clearly seen.

The lower hardness of 45 R_c (Figure 5.7) is an exception (designated as a soft region) that corresponds to the position where the laser beam dwelled longer than at other positions because of CNC programming. The microstructure in the soft region consists of mostly

tempered martensite with little evidence of fine carbide precipitation (Figure 5.8 (B)). The absence of carbide precipitation is attributed to the dissolution of molybdenum and chromium carbides in solid solution. Only the vanadium carbide (V_4C_3) can remain undissolved [Smith, 1993]. Both tempered martensite and dissolution of the carbides led to the loss of hardness.

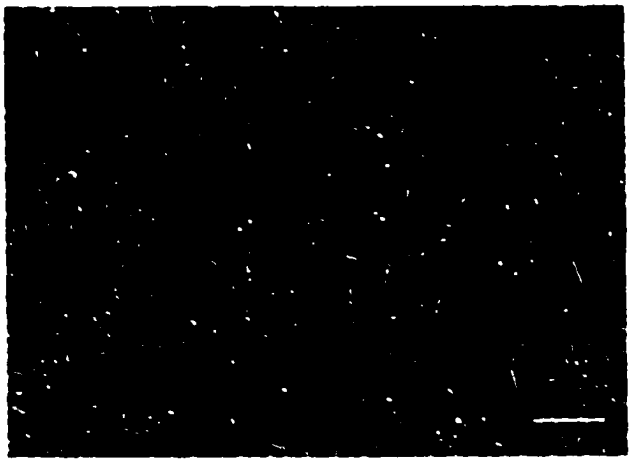

(A)

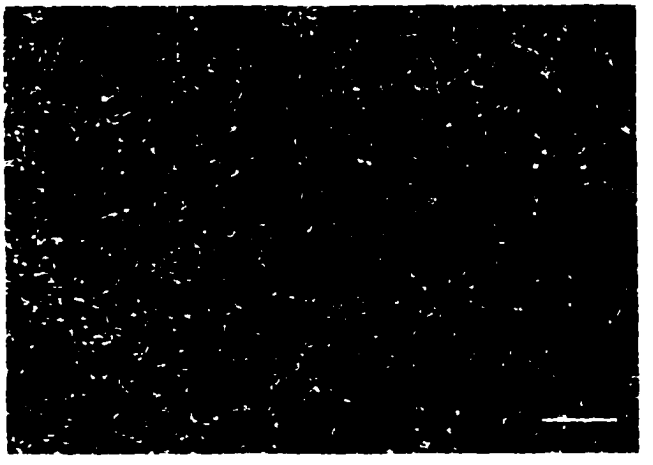

(B)

Figure 5.8. SEM micrographs of (A) a typical region and (B) a soft region (etchant: 4% nital)

Evaluation of the Extruded Aluminum

Figure 5.9 shows the two pieces of cold-extruded aluminum bars, 11.3 mm in diameter, which underwent 56% reduction in diameter. A maximum compressive load of 260,000 N was applied in the extrusion process. The extruded aluminum bar from the die fabricated with use of the LBFF is designated as A, and the bar from the as-machined die as B. The roundness of both A and B was examined by means of a Brown & Sharpe coordinate measurement machine (CMM). Surface roughness along the peripheral direction of A and B was measured by use of a surface profilometer that featured a 0.025 mm diamond stylus. Table 5.3 gives the measurement results.

Table 5.3. Roundness and surface roughness on A and B

	A	B
Roundness (mm)	0.0753	0.0027
Surface roughness (μm)	20	1.6

Figure 5.9. Samples of cold-extruded aluminum bars using the die made by the LBFF (A)

Although the surface roughness of B is within the limits of average industrial application of extrusion, the surface roughness of A exceeded the allowable values. In addition, the roundness is 26 times higher in A than in B, suggesting the need for post-finishing for industrial use of LBFF dies. The relatively poor accuracy and tolerance of extruded bars with LBFF die is attributed to the presence of recast layer on the walls (Figure 5.10).

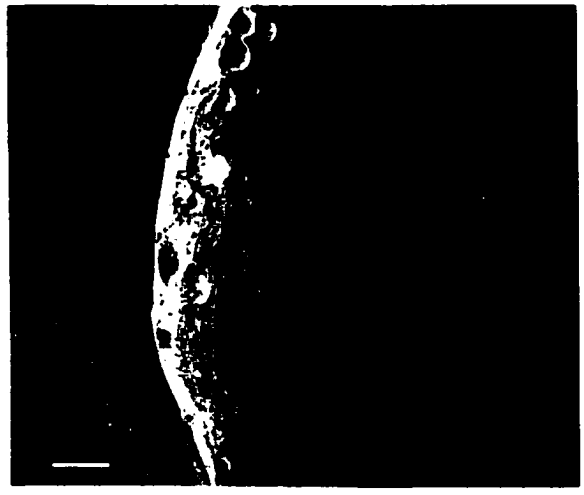

Figure 5.10. Axial section of the LBFF die showing presence of recast layer on the wall

CONCLUSION

The following conclusions are based on the experimental results obtained when LBFF was applied to the fabrication of aluminum extruding dies:

(1) The design of the quasi-axial nozzle has successfully eliminated the directional effect of lateral powder delivery system on the uniformity of dies.

(2) The laser power calculation ensured production of tooling of near-theoretical density and acceptable surface roughness.

(3) The die exhibited hardness close to that of wrought and as-quenched H13 tool steel.

(4) Extrusion tests indicate the need for post-processing in preparation of an industrial tooling by use of LBFF.

ACKNOWLEDGMENTS

The authors would like to acknowledge the assistance provided by Larry Couture and Larry Hanft of the machine shop.

REFERENCES

The Aluminum Association, (1995), *The Aluminum Extrusion Manual*, The Aluminum Association, Inc., Washington, DC 20006.

Bamberger, M., W.D. Kaplan, B. Medres, and L. Shepeleva, (1998), "Calculation of Process Parameters for Laser Alloying and Cladding," *Journal of Laser Applications*, Vol.10 (1), pp. 29-33.

Budinski, K.G., (1996), *Engineering Materials: Properties and Selection*, Prentice Hall Inc., NJ 07632.

Chande, T., and J. Mazumder, (1985), " Two-dimensional, Transient Model for Mass Transport in Laser Surface Alloying," *Journal of Applied Physics*, Vol.57 (6), pp. 2226-2232.

Davis, J.R., et al., (1990), *Metal Handbook: Properties and Selection: Iron, Steels, and High Performance Alloys*, Vol. 1, ASM International, OH 44073.

Hu, Y-P., C.W. Chen, and K. Mukherjee, (1998), " Development of a New Laser Cladding Process for Manufacturing Cutting and Stamping Dies," *Journal of Material Science*, Vol. 33 (5), pp. 1287-1292.

Jiang, Wenping, and Pal Molian, (2001), " Laser-Based Flexible Fabrication of Functionally Gradient Mold Inserts," Accepted for publication by *the International Journal of Advanced Manufacturing.*

Kalpakjian, S., and S.R. Schmid, (2001), *Manufacturing Engineering and Technology*, Prentice Hall Inc., Upper Saddle River, NJ 07458.

Kawasaki, M., K. Takase, S. Kato, M. Nakagawa, and K. Mori, (1992), " Development of Engine Valve Seats Directly Deposited onto Aluminum Cylinder Head by Laser Cladding Process," *SAE Technical Paper Series*, SAE Paper No. 9205712, pp. 1-15.

Matsushita, T., (1990), " Improvement of Equipment for Close-Tolerance Forging and Extrusion in Japan," *Journal of Materials Processing Technology*, Vol. 22(3), pp. 223-238.

Mazumder, J., A. Schifferer, and J. Choi, (1999), " Direct Materials Deposition: Designed Macro and Microstructure," *Mat. Res. Soc. Symp. Proc.*, Vol. 542, pp. 51-63.

Mazumder, J., J. Choi, K. Nagarathnam, J. Koch, and D. Hetzner, (1997), " The Direct Metal Deposition of H-13 Tool Steel for 3-D Components," *Journal of Metals*, (5), pp. 56-60.

Misiolek, W.Z., K.T. Winther, and S.J. Rock, (1999), " Rapid Prototyping of Extrusion Dies Using Layer-Based Techniques," *Journal of Materials Engineering and Performance*, Vol. 8(1), pp. 23-30.

Picasso, M., C.F. Marsden, J. –D. Wagniere, A. Frank, and M. Rappaz, (1994), " A Simple but Realistic Model for Laser Cladding," *Metallurgical and Materials Transactions* B, Vol. 25B, pp. 281-291.

"*Rapid Prototyping Report*", (1991-1996), published monthly, CAD/CAM Publishing Inc., CA 92109.

Smith, W.F., (1993), *Structure and Properties of Engineering Alloys*, McGraw-Hill, Inc., New York.

Steen, W., (1998), *Laser Materials Processing*, Springer-Verlag Limited, London.

Steen, W.M., V.M. Weerasinghe, and P. Monson, (1986), " Some Aspects of the Formation of Laser Clad Tracks," *SPIE, High Power Lasers and Their Industrial Applications*, Vol. 650, pp. 226-233.

Yellup, J.M., (1995), " Laser Cladding Using the Powder Blowing Technique," *Surface and Coatings Technology*, Vol. 71 (3), pp. 121-128.

Yevko, V., C.B. Park, G. Zak, T.W. Coyle, and B. Benhabib, (1998), " Cladding Formation in Laser-beam Fusion of Metal Powder," *Rapid Prototyping Journal*, Vol.4 (4), pp. 68-184.

CHAPTER 6. FUNCTIONALLY GRADED MOLD INSERTS BY LASER-BASED FLEXIBLE FABRICATION: PROCESSING MODELING AND STRUCTURE

A paper to be submitted to ASME Journal of Manufacturing Science and Engineering

Wenping Jiang and Pal Molian

ABSTRACT

Laser-based flexible fabrication (LBFF), a novel solid freeform fabrication method based on the principles of laser cladding, was developed to produce functionally graded mold inserts. Unlike similar methods such as laser engineered net shaping (LENS^{TM}), LBFF uses shaped beams, quasi-coaxial nozzle for powder delivery, and functionally graded materials. The additive layering of H13 steel, Ni/Cr alloy and TiC using circular and rectangular beam profiles built a 30-mm hollow square, 8 mm wall thick mold insert. Finite element analysis using ANSYS program was applied to determine temperature fields and thermal gradients associated with circular and rectangular beams. The microstructures and interfaces were examined using scanning electron microscope and related to the temperature gradients. Microhardness measurements were performed on the FGM and compared with the benchmark H13 steel molds. Results show nearly full-density molds with excellent integrity, beneficial microstructures, strong interfaces, and high hardness.

INTRODUCTION

Solid Freeform Fabrication (SFF) is an advanced manufacturing technology designed to build solid physical models directly from 3D-CAD data representation without special tooling. SFF uses material addition technology to produce concept models, prototypes, and

tooling for manufacturing dies and molds [1]. It offers benefits such as reduction in lead-time, ability to make complex components, and cost savings [2]. However, fabrication of functional metallic and ceramic components through SFF still remains elusive. Initially, selective laser sintering (SLS) of powder materials seemed to have the potential to produce functional prototypes, even for direct tooling fabrication. However, SLS required polymer binders and low-melting compounds. Shrinkage, porosity, and low density of parts are the chief drawbacks of SLS that prevent it from competing against machining and EDM for mold fabrication. Laser cladding (LC) based freeform fabrication technology has emerged as a promising approach to correct the deficiencies in SLS. LC consists of pneumatically injecting powders through a nozzle into a laser-created molten pool of substrate or laser melting pre-placed powders. Subsequent solidification forms strongly bonded layers of fully dense and possibly homogeneous microstructures. LC offers several advantages including flexibility in processing structural materials, fine grain structure, low dilution, minimal thermal degradation, formation of non-equilibrium crystalline and amorphous structures, and extension of solid solubility of alloying elements [3].

LC was applied in multiple, overlapping layers to create functional 3D objects [4-6]. Several LC-based SFF processes with minor variations were developed [7-11]. These include: 1) directed light fabrication (DLF) from Los Alamos National Laboratory; 2) direct metal deposition (DMD) from the University of Michigan; 3) laser engineered net shaping (LENS) from Sandia National Laboratory; and 4) shape deposition manufacturing (SDM) from Stanford University. Despite such significant developments, the LC-based SFF processes suffer from drawbacks including rough surface, residual stresses, low dimensional accuracy, porosity, and crack formation [12]. As a result, this technology could not be

implemented in industry. A number of experimental and numerical studies were conducted to understand the LC-based SFF processes. Kobryn et al. [13] investigated the effect of laser power and traverse speed on the formation of built height and porosity in laser deposition of Ti-6Al-4V using a factorial experiment. Vasinonta et al. [14] developed process maps for fabricating thin-walled sections with AISI 304 stainless steel with emphasis on stress-induced warping. Kaplan and Groboth [15] analyzed laser beam cladding of Stellite-6 powder process using simplified energy and mass balance equations.

In this paper, a LC based SFF technique, namely, laser-based flexible fabrication (LBFF), has been developed to manufacture functional components such as molds and dies, the objective being to produce high-performance parts that are free of defects mentioned above. LBFF is different from others such as LENS in these aspects: 1) use of materials to make parts with functionally graded composition and microstructure; 2) application of shaped laser beams to produce desired surface finish and dimensional tolerance, and to reduce residual stresses and dilution in the functional layers; and 3) use of a quasi-coaxial nozzle for powder delivery [16].

Since LBFF involves direct interactions between moving heat source and powder materials, the phenomena of mass transport (powder), heat transfer, and fluid flow make it rather complex. Like any other SFF process, it is important to understand the underlying physical mechanism so that the processing conditions will be chosen to produce parts with high integrity (in terms of surface roughness, crack and porosity) and mechanical properties, such as hardness and toughness, which are primarily dependent upon microstructures. Hence, the solutions to heat flow analytical models are developed using ANSYS package to determine the temperature distribution and temperature gradients which enabled to predict

the molten pool dimensions, layer depth, type of microstructure and thermal distortion. Thus, the work presented in this paper describes production, process model, characterization, and evaluation of the FGM mold inserts by a novel SFF process.

EXPERIMENTAL MATERIALS AND METHODS

Figure 6.1 shows a schematic of LBFF where shaped beams are used to make functional objects from CAD files and CNC programming by controlled laser melting of the localized powders of different materials in a functionally graded fashion. Micro-sized powders of TiC, Ni/Cr alloy, and H13 were used as construction materials in this work because they exhibit the desired mechanical and physical properties of die and mold materials. TiC, a ceramic coating material with low thermal conductivity, is capable of increasing die- and mold-operative temperature, while maintaining a low temperature at the surface. Ni/Cr alloy serves as the intermediate layer (mainly because of diffusion) between TiC and H13 layers. Its major function is to further reduce oxidation and high-temperature corrosion of the H13 layer as well as to improve the adhesion between these layers [17, 18]. H13 is a benchmark material for dies and molds. In addition, these materials also have closely matching thermal expansion coefficients [18], preventing crack formation and improving adhesion during processing. The addition of materials in creating the inserts was configured in such a way that each side was composed of TiC, Ni/Cr alloy, and H13 powder, respectively, from outside to inside. Through these combinations, high surface hardness and core toughness were expected (Figure 6.2).

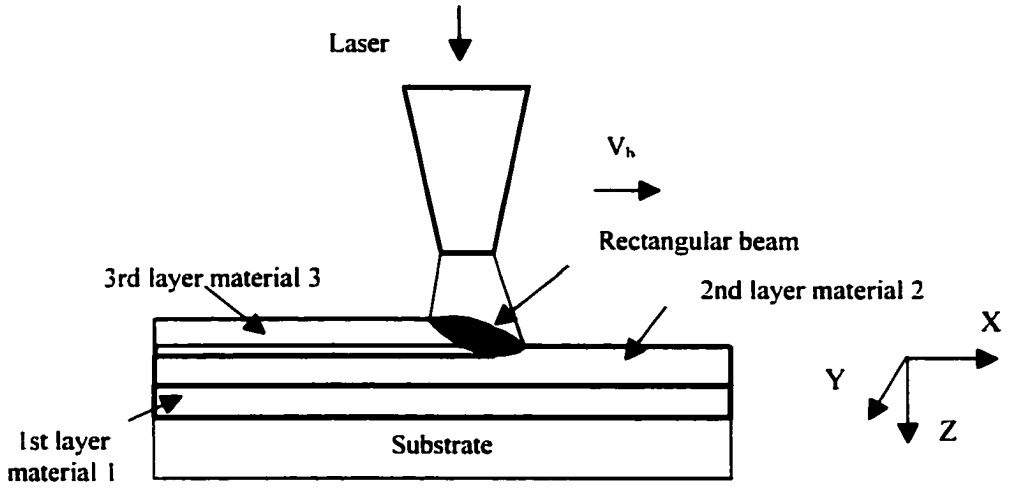

Figure 6.1. Schematic showing the LBFF process

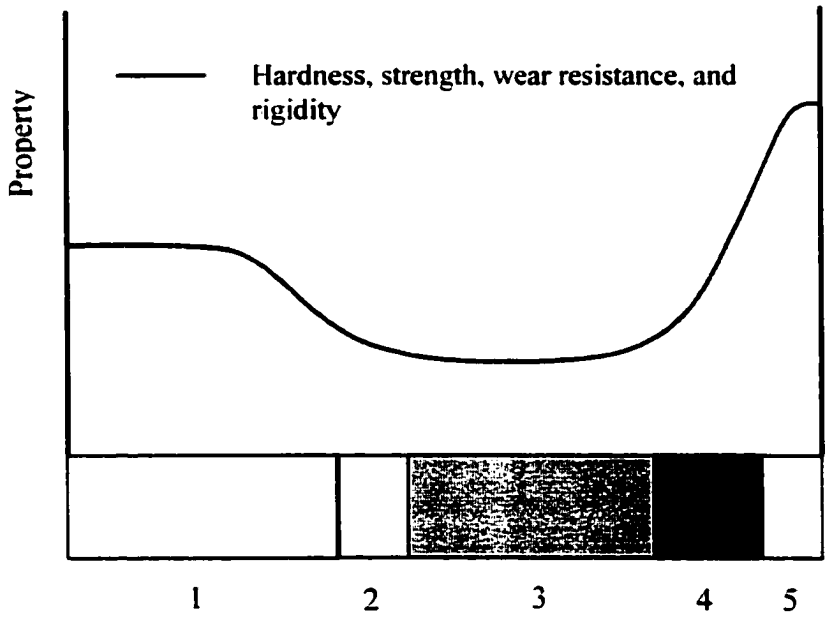

Figure 6.2. Expected mechanical behavior of FGM mold insert (1: 70~100 μm H13 powder; 2: transition zone between H13 powder and Ni/Cr alloy powder; 3: 100 μm Ni/Cr alloy powder; 4: transition zone between Ni/Cr alloy and TiC powder; 5: 2 μm TiC powder)

A 30 mm square-shaped geometry was chosen as die insert design, with a wall thickness of 8 mm. The maximum building height of parts was varied depending on the width of overlapped track, thickness of single layer, and number of layers deposited. A high-power, continuous wave CO_2 laser with beam configurations of circle and rectangle was used to melt the powders, introduced through a powder delivery system on H13 steel substrate. First, H13 powders were laser melted and solidified to a thickness of 6.2 mm. Second, Ni/Cr alloy was deposited for a thickness of 1.5 mm. Defocused circular beams (15 mm below focal plane) with a diameter of 0.8 mm were used in both cases. Third, TiC was formed to a thickness of 0.3 mm using a focused rectangular beam of size of 0.1 mm × 1 mm. The rectangular beam offered a high degree of surface integrity compared to the circular beam.

In this fabrication process, the laser power was between 500~600 W as powers greater than these tend to produce layers with poor surface integrity. Scanning speeds were 5, 8.5, to 42 mm/s for Ni/Cr alloy, H13, and TiC powder, respectively. Under these processing conditions, energy density ($\frac{P}{VD}$) for metal powders (73.5 for H13 and 150 J/mm^2 for Ni/Cr powder) was much higher that for TiC powder (33 J/mm^2). The deposition layer thickness for H13 and Ni/Cr alloy powder per each laser scan was 0.13 mm, while it was only 0.008 mm for TiC. Figure 6.3 shows a photograph of the functionally graded die insert in which visual and scanning electron microscope (SEM) examination revealed few defects such as porosity, indicating nearly full density. The fabricated inserts were cleaned up, sectioned, polished and etched for characterization of microstructure and composition by SEM. Vickers microhardness (1.0 kgf) test was used to determine the hardness distribution across the mold and compared with the benchmark H13 mold.

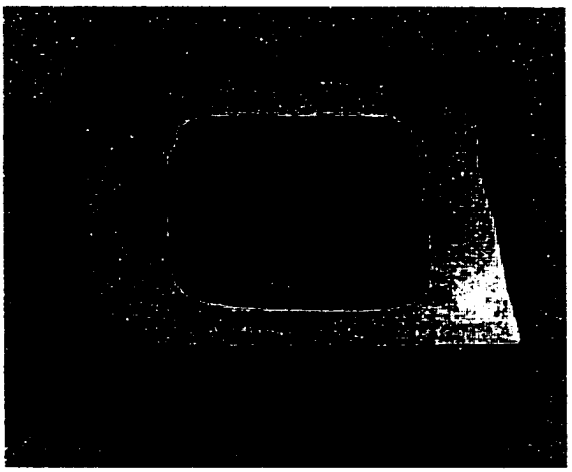

Figure 6.3. Photo illustrating a square functionally graded die insert fabricated using LBFF

PROCESS MODELING

Formulation

The first law of thermodynamics states that thermal energy is conserved. For a differential control volume, if heat losses from convection and radiation are negligible, and latent heat is not considered, then heat transfer problem associated with laser beam melting of pre-placed H13 powder can be mathematically described as:

$$\rho C \frac{\partial T}{\partial t} + \{L\}^T \{q\} = 0 \qquad (6\text{-}1)$$

where: ρ is temperature dependent density; C is specific heat; T is temperature; and t is time. L represents the divergence operator. q is the heat flux related to the thermal gradients by Fourier's law:

$$\{q\} = -[D]\{L\}T \qquad (6\text{-}2)$$

where: $[D] = \begin{bmatrix} k_x & 0 & 0 \\ 0 & k_y & 0 \\ 0 & 0 & k_z \end{bmatrix}$ is conductivity matrix. If material is homogeneous, then there is $k_x = k_y = k_z = k$. Combining equations (6-1) and (6-2), we have:

$$\rho(T)C(T)\frac{\partial T}{\partial t} = \frac{\partial}{\partial x}\left(k(T)\frac{\partial T}{\partial x}\right) + \frac{\partial}{\partial y}\left(k(T)\frac{\partial T}{\partial y}\right) + \frac{\partial}{\partial z}\left(k(T)\frac{\partial T}{\partial z}\right) \qquad (6\text{-}3)$$

This equation, based on the global Cartesian system, is used for solving the surface thermal gradients of circular and rectangular beams. Since we are only interested in surface thermal gradients, equation (6-3) can be reduced to:

$$\rho(T)C(T)\frac{\partial T}{\partial t} = \frac{\partial}{\partial x}\left(k(T)\frac{\partial T}{\partial x}\right) + \frac{\partial}{\partial y}\left(k(T)\frac{\partial T}{\partial y}\right) \qquad (6\text{-}4)$$

with initial condition: $T(\pm\infty, y, t) = T(x, \pm\infty, t) = T(x, y, 0) = 293$ K; and boundary condition: $x^2 + y^2 \le R_b^2$, $\frac{\alpha P}{\pi R_b^2}$ = constant; in other areas, heat flux=0.0.

The solution of non-linear equation (6-4) is dependent upon temperature-dependent density, specific heat, and thermal conductivity. The powder material, H13, used in this computation is assumed to have the physical properties of bulk material. Since the temperature-dependent properties of H13 are only available up to a temperature of 600°C (873 K), properties at any temperature, higher than 600°C and lower than its melting point, are taken as the values at 600°C. Table 6.1 lists the variation of thermal properties with temperature for H13 steel.

Table 6.1. Density, specific heat, and thermal conductivity of H13 steel [19]

Temperature (K)	293	773	873
Density (kg/m^3)	7800	7640	7600
Specific heat (J/kg.K)	460	550	590
Thermal conductivity (W/m.K)	25.0	28.5	29.3

ANSYS, a package of finite element analysis software, is widely used to solve steady, non-steady, linear, and non-linear problems. In this study, ANSYS was applied to the non-linear heat conduction problem of laser melting the pre-placed H13 powder. Plan elements of 6 nodes and 4 nodes were chosen for meshing the computation domains of circular and rectangular beams, respectively. The domain was a rectangle of 60 mm in length and 30 mm in width. Only a quarter of the rectangle was considered due to the symmetrical characteristics of the domain geometry and load. Element edge length was set to 6.25×10^{-5} m within the beam, 2×10^{-3} m for all other regions. In the regions adjacent to the beam, elements were refined. The meshes for surface thermal gradient computation corresponding to circular beam and rectangular beam are illustrated in Figure 6.4. Laser energy is assumed to be uniform over the beam profiles. The related basic load settings for the computations related to ANSYS are listed in Table 6.2.

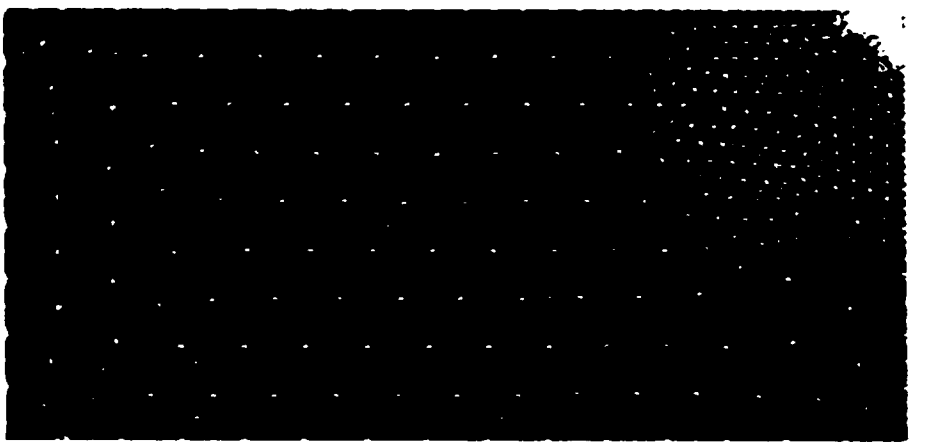

(A)

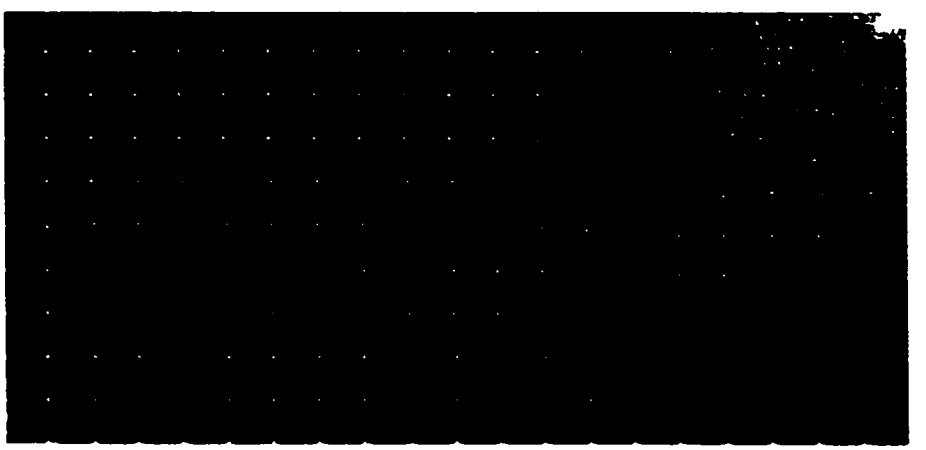

(B)

Figure 6.4. The meshes used for surface thermal gradient computations for: (A) circular beam; and (B) rectangular beam

Table 6.2. Load settings of ANSYS for surface thermal gradient computation

Heat flux (W/m^2)	3.75×10^8
Interaction time (sec)	0.0235
Time at the end of load step (sec)	0.0235
Time step size (sec)	0.00235
Initial temperatures (K)	293
Automatic time stepping	ON
Use previous size	YES

Solution

As heating sources, laser beams of the same intensity but of shaped geometry can produce thermal gradients of different magnitude and distribution (Figure 6.5). At a typical power density of 9.4×10^7 W/m^2 (corresponding to laser power of 500 W on rectangular beam) and an interaction time of 0.0235 s, numerical analysis shows that rectangular beam (RB) produces a more uniform thermal gradient profile than circular beam (CB). RB has a maximum thermal gradient of 4.94×10^6 K/m, 10% lower than CB. In addition, the highest thermal gradient position of RB is farther away from the beam center than CB. The differences in thermal gradients affect surface tension gradient, a controlling factor for the formation of cross flow in a molten pool [20]. Cross flow plays a decisive role in the uniformity of alloy distribution and surface roughness. Steep thermal gradient variations result in severe cross flow, and possibly rough surfaces. Depositions of TiC powder using

rectangular beam produced layers with surface roughness (*Ra*) value less than 20 μm, while using circular beam did not produce acceptable surface roughness.

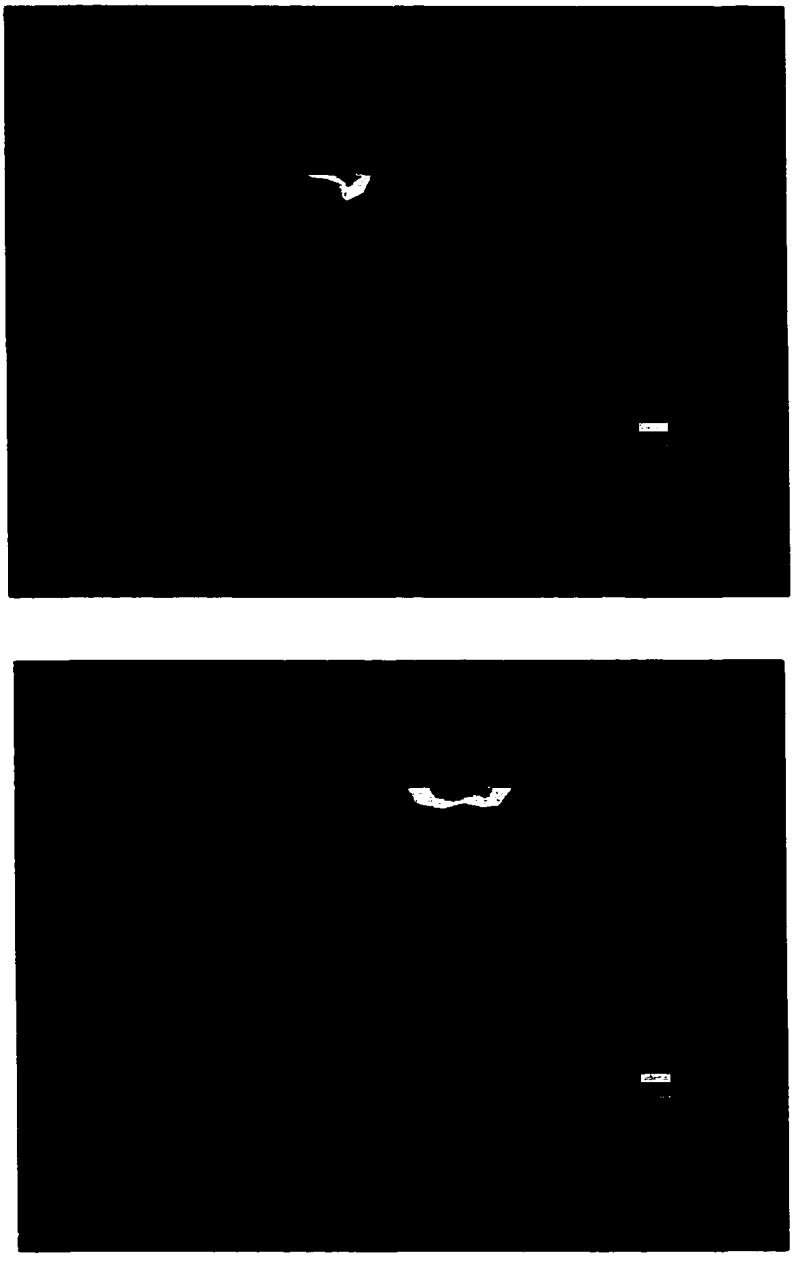

(A)

(B)

Figure 6.5. Surface thermal gradient profile of: (A) rectangular beam; and (B) circular beam (laser power: 500 W; and interaction time: 0.0235 s)

Cooling rate

Normally, cooling rate is related to thermal gradient and beam velocity given by $R = |V \times G|$. Variations of cooling rate along the beam-moving direction follow the same trend as shown by surface thermal gradients. The cooling rate is computed in the order of 10^4 K/s (corresponding to a laser power 500 W and a scanning speed, 8.5 mm/s), which is similar to the results from a point source analytical model (Appendix C). This cooling rate is very high in comparison to those obtainable in conventional material processing, however, it is somewhat lower than laser glazing and alloying.

SOLIDIFICATION MICROSTRUCTURES

For a given composition, the formation of specific microstructure depends mainly on solidification parameters such as thermal gradient ($G = \frac{dT}{dx}$), cooling rate ($R_c = \frac{dT}{dt}$), solidification-front moving velocity, and the degree of undercooling [21]. SEM micrographs (Figure 6.6) show a variety of dendrite structures, typical of the high cooling rate and larger undercoolings. In the H13 layer, the average secondary dentrite arm spacing, λ_2, is 2.5 μm, and the cooling rate can be estimated as 2.5 × 10^4 K/s ($\dot{T} = \frac{1}{\lambda_2^3}(3.87 \times 10^{-13})$ [22]), which is very close to the cooling rate obtained from simulation. Columnar dendrites, segmented by the interfaces of individual deposition layer and aligned in the direction of maximum thermal gradients, are observed in H13 and Ni/Cr alloy layers. This could be explained by the epitaxial growth of the layer on the substrate where the grains are favorably situated as well as steeper temperature gradients are provided by the laser parameters. In contrast, equiaxed

dendritic structures were observed in TiC layers. Here, new dendrites form and grow in the mushy zone with random orientation. The equiaxed dendrites arise from a heterogeneous nucleation mechanism in which Ni/Cr layer diffuses to provide sites for nucleation. Additionally, the reduced thermal gradients and high growth rates made possible by the laser parameters reduced the G/R ratio, resulting in equiaxed dendrites.

Formation of these microstructures is favorable to the expected mechanical properties. The segmented columnar microstructures observed in both H13 and Ni/Cr layers could increase strain tolerance [23], yielding improved ability to resist thermal shock and spallation caused by cyclic thermal loadings in service. The equiaxed layer of TiC produced by LBFF would likely exhibit reduced thermal conductivity [24], which is beneficial to reduced oxidation of the underlying H13.

(A)

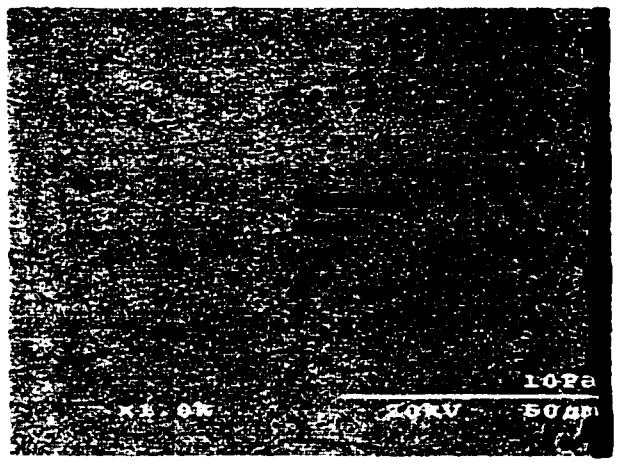

(B)

(C)

Figure 6.6. Typical microstructures in: (A) H13 layer; (B) Ni/Cr alloy layer; and (C) TiC layer

Final grain sizes depend, to a large extent, on the rate of cooling and have a direct effect on the mechanical properties [25]. The maximum grain dimension of all regions was measured less than 25 μm. However, those grains in the regions closer to surface were much

smaller. Re-heating of the previous layers during layer processing caused the growth of grains in zones away from the surface.

Figure 6.7 displays sharp interfaces among distinct layers. Defects were not identified at the interfacial zones. H13 layer was "interlocked" with Ni/Cr layer possibly due to the disturbance of the moving substrate to slowly solidifying molten pool because of the high density (150 J/mm^2) and the thick deposition layer (0.13 mm) used, while no "interlock" occurrence was observed at the interface between Ni/Cr layer and TiC layer because of the quick solidification resulted from low energy density (33 J/mm^2) and thin deposition layer (0.008 mm). Elemental analysis of energy by the energy dispersive spectrum (EDS) shows that more than two-third of TiC layer was diluted by Ni/Cr powder. Furthermore, it did not show any abrupt change in the constituents across those interfaces (Figure 6.8). The observation was in agreement with the definition of functionally graded materials.

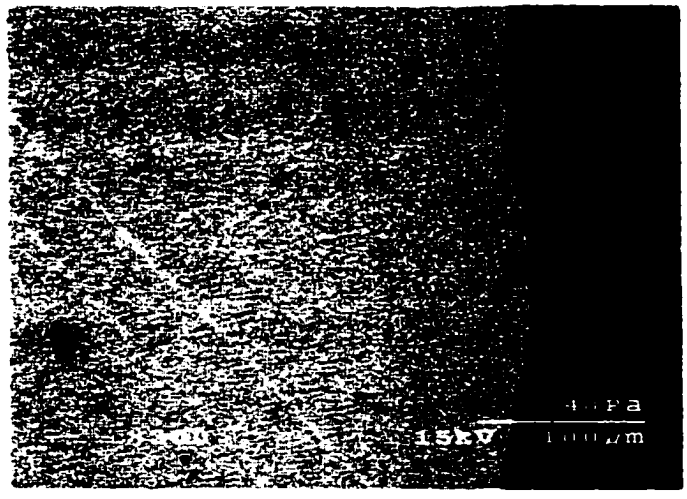

(A)

Figure 6.7. SEM showing the interfaces of: (A) H13 and Ni/Cr alloy; and (B) TiC and Ni/Cr alloy

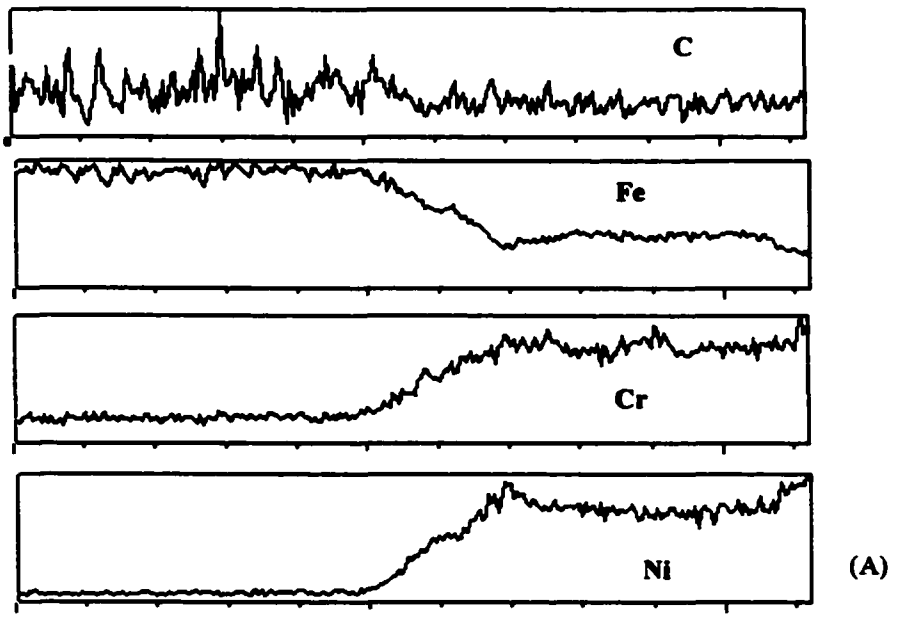

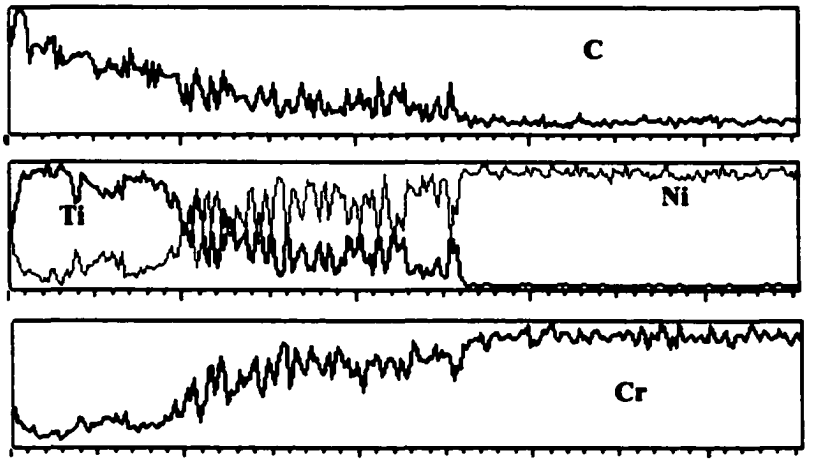

Figure 6.8. SEM of compositional distribution of the FGM interface of: (A) H13 and Ni/ Cr alloy; and (B) TiC and Ni/Cr alloy

Figure 6.9 shows the Vicker's microhardness variation with the distance from outside to inside surface. The data scatter was ± 4%. Compared to the hardness of heat- treated H13 steel, the hardness in the H13 layer of this functionally graded die insert was 15% higher. The FGM insert is likely to enhance corrosion/erosion resistance to aluminum melt, to improve oxidation resistance, and to reduce deformation at elevated temperature based on previous studies [18,26].

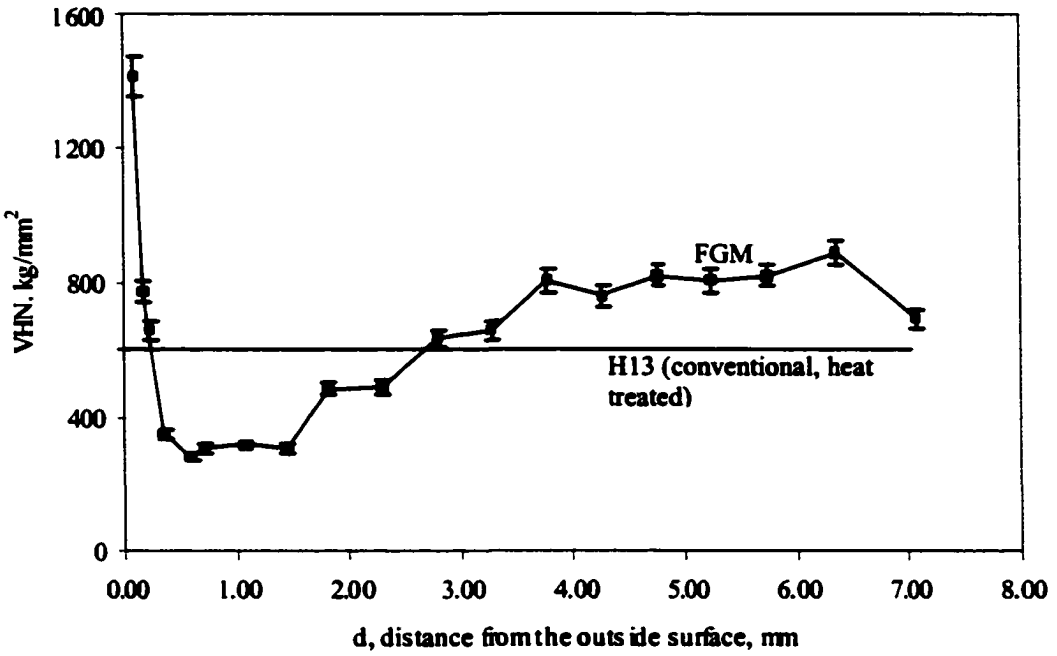

Figure 6.9. Vickers microhardness (1.0 kgf) profile along the die insert wall thickness starting from outside

CONCLUSIONS

(1) A square die insert of functionally graded compositions of H13, Ni/Cr alloy and TiC was designed and fabricated using shaped beam profiles with LBFF. Evaluations showed full density of the insert, and gradual change of the composition in the transitional regions between distinct layers.

(2) Surface thermal gradients of circular beam and rectangular beam were modeled using ANSYS and compared. The cooling rates were estimated and correlated with secondary dentrite arm spacing.

(3) Maximal grain size was found to be approximately 25 μm. The coarse grains were resulted from repeated heating by the layer addition process.

(4) Microhardness of FGM was higher than that of conventional H13 steel. Improvements in strain tolerance, and in resistance to thermal shock are expected due to the peculiar arrangement of microstructures in this functionally graded mold insert. In addition, the insert is likely to show improved corrosion/erosion resistance, and reduced deformation and oxidation at elevated temperatures.

ACKNOWLEDGEMENTS

Thanks are due to Mr. Larry Couture, Mechanical Engineering department, for his assistance in grinding the die insert; Dr. W. Wang and Mr. Y. Tian, Materials Science and Engineering department, for their help in sample preparation and etching.

REFERENCES

1. Hull, C., Feygin, M., Baron, Y., Sanders, R., Sachs, E., Lightman, A., and Wohlers, T., 1995, "Rapid Prototyping: Current Technology and Future Potential," Rapid Prototyping Journal, 1, No.1, pp11-19.
2. Hopkinson, N., and Dickens, P., 2001, "Rapid Prototyping for Direct Manufacture," Rapid Prototyping Journal, 7, No. 4, pp.197-202.
3. Vilar, Rui, 2001, "Laser Cladding," The international Journal of Powder Metallurgy, 37, No. 2, pp. 31-47.
4. Kruth, G.B., 1991, " Material Ingress Manufacturing by Rapid Prototype Techniques, Manufacturing Technology," Annals of the CIRP, 40, No. 2, pp. 603-614.

5. Gerken, J., Haferkamp, H., and Schmidt, H., 1994, " Rapid Prototyping/Manufacturing of Metal Components by Laser Cladding," Proceedings of the 27th ISATA on Rapid Prototyping and Laser Applications for Automotive Industries, Aachen, Germany, October 31-November 4, 1994, pp. 85-90.

6. Peng, S.C., Chou, C.J., and Jeng, J.Y., 1994, " Application of Selective Laser Cladding in Rapid Prototype," Proceedings of the 27th ISATA on Rapid Prototyping and Laser Applications for Automotive Industries, Aachen, Germany, October 31-November 4, pp. 273-279.

7. Milewski, J., Lewis, G.K., Fonseca, J., and Nemec, R.B., 2000, "Laser Powder Deposition of a Near Net Shape Injection Mold Core-A Case Study," Materials and Manufacturing Processes, 15, No.2, pp. 247-258.

8. Keicher, D.M., Miller, W.D., 1998, " LENS™ moves beyond RP to Direct Fabrication," Metal Powder Report, 53, No.12, pp26-28.

9. Mazumder, J., Choi, J., Nagarathnam, K., Koch, J., and Hetzner, D., 1997, " The Direct Metal Deposition of H13 Tool Steel for 3-D Components," Journal of Metals, May, pp. 55-60.

10. Link, G.R., Fessler, J., Nickel, A., and Prinz, F., 1998, " Rapid Tooling Die Cast Inserts Using Shape Deposition Manufacturing," Materials and Manufacturing Processes, 13, No.2, pp. 263-274.

11. Irving, R., 1999, "Taking a Powder," Mechanical Engineering, September, pp. 55-59.

12. Kathuria, Y.P., 2000, "Some Aspects of Laser Surface Cladding in the Turbine Industry," Surface and Coatings Technology, 132, pp. 262-269.

13. Kobryn, P.A., Moore, E.H., and Semiatin, S.L., 2000, " The Effect of Laser Power and Traverse Speed on Microstructure, Porosity, and Build Height in Laser-Deposited Ti-6Al-4V,"Scripta Materialia, 43, pp. 299-305.

14. Vasinonta, A., Beuth, J.L., and Griffith, M.L., 2001 "A Process Map for Consistent Build Conditions in the Solid Freeform Fabrication of Thin-Walled Structures," Journal of Manufacturing Science and Engineering, 123, pp. 615-622.

15. Kaplan, A.F.H., and Groboth, G., 2001, "Process Analysis of Laser Beam Cladding," Journal of Manufacturing Science and Engineering, 123, pp. 609-614.

16. Jiang, W., Stock, M., and Molian, P., 2002, " Production of Aluminum Extrusion Dies Using a Laser-Based Flexible Fabrication Technique," The Thirtieth Annual North American Manufacturing Research Conference, West Lafayette, Indiana (in press).

17. Mattox, M., 1994, " Growth and Growth-Related Properties of Thin Films Formed by Physical Vapor Deposition," ASM Metal Handbook, 5, ASM International, Metals Park, OH, pp 538-555.

18. Jiang, W., and Molian, P., 2002, "Laser-Based Flexible Fabrication of Functionally Graded Mold Inserts," The International Journal of Advanced Manufacturing Technology (in press).

19. Http://www.sz-metal.si/products/steels/UTOPMO2.htm. (date accessed: April 2, 2002)

20. Mazumder, J., and Chande, T., 1985, "Two Dimensional, Transient Model for Mass Transport in Laser Surface Alloying," Journal of Applied Physics, 57, No. 6, pp. 2226-2232.

21. Simchi, A., Petzoldt, F., and Pohl, H., 2001, "Direct Metal Laser Sintering: Material Considerations and Mechanisms of Particle Bonding," The International Journal of Powder Metallurgy, 37, No. 2, pp. 49-60.

22. Mazumder, J., Schifferer, A., and Choi, J., 1999, " Direct Materials Deposition: Designed Macro and Microstructure," Symposium Proceedings of Material Research Society, 542, pp. 51-63.

23. Steffens, H.D., Bablak, Z., and Brandl, W., 1991, "Thermal Barrier Coatings: Some Aspect of Properties Design," Proceedings of Fourth National Spray Conference, ASM International, Material Park, OH, pp. 289-294.

24. An, K., Ravichandran, K.S., Dutton, R.E., and Semiatin, S.L., 1999, " Microstructure, Texture, and Thermal Conductivity of Single-Layer and Multilayer Thermal Barrier Coatings of Y_2O_3-Stablized ZrO_2 and Al_2O_3 Made by Physical Vapor Deposition," Journal of the American Society, 82, Vol. 2, pp. 399-406.

25. Hurst, S., 1996, " Metal Casting," Intermediate Technology Publications, London.

26. Jiang, W., and Molian, P., 2001, "Nanocrystalline TiC Powder Alloying and Glazing of H13 Steel Using a CO_2 Laser for Improved Life of Die-Casting Dies," Surface and Coatings Technology, 135, pp. 139-149.

CHAPTER 7. GENERAL CONCLUSIONS AND FUTURE WORK

Solid freeform fabrication (SFF) is emerging as a potential competitor for subtractive processes to make dies and molds. Its role in tooling industries begins to change from early concept proof to currently real tools. However, rough surfaces, non-uniformity in deposited tracks, and residual stress impair the further applications of this new technology. In this work, a variation of SFF technologies, laser-based flexible fabrication (LBFF) that uses both circular and rectangular laser beams to deposit powders of varied sizes was investigated for improved surface finish, dimensional tolerance, and reduced dilution. It not only offers the flexibility to design functionally graded dies and molds with tailored materials, but also provides the feasibility to build up functional tools with geometry such as embedded structures that would be difficult to fabricate in conventional machining methods.

In the experiments conducted on laser-based coating process, criteria of smooth and flaw-free surface were set to optimize the processing parameters. It was determined that laser glazing, laser surface alloying with TiC powder of varied sizes (0.3, 2, and 30 μm), as well as furnace tempering affected the microhardness, and the ability of die steel, H13, to resist corrosion and erosion in simulated metal casting conditions differently. Laser glazing melted a thin layer (< 0.5mm) of material and solidified quickly to refine structure, resulting in a hardness increase of about 30%. It enhanced the ability to resist erosion significantly, however, it only improved corrosion resistance marginally. Laser surface alloying with TiC powder showed that, under the same processing conditions, powder particle size had a marked effect both on surface roughness and resistance to corrosion and erosion. Laser alloying with TiC of 2 μm and 0.3 μm produced high quality surfaces. In contrast to these two powders, TiC of 30 μm resulted in rough surfaces. Nano-sized TiC powder of 0.3 μm

improved the ability against both corrosion and erosion significantly, though it reduced the hardness of laser-alloyed samples by approximately 50%. Conclusions drawn from this detailed experimental investigation served as a guide for selecting materials and determining processing parameter for the successive LBFF work.

LBFF included design and fabrication of powder delivery system, shaped beams, and functionally graded materials. The fabrication of circular and square dies by use of this technique showed that LBFF is capable of producing fully dense and functional parts, although their surface roughness was not as low as desired. The concept of functionally graded die and mold inserts was formulated, and prototyping process of the inserts (Ni-Cr alloy/TiC) by use of LBFF was determined. Evaluations were performed in die-casting, injection molding, and in thermal fatigue environment. Results indicated that the functionally graded TiC core- Ni-alloy shell mold was superior in resistance to plastic deformation and in dimensional stability at elevated temperature.

In the work of producing aluminum extrusion dies in H 13 powder using LBFF, a quasi-axial nozzle was deigned and prototyped in replacement of the lateral powder delivery system. A lumped heat capacity model, based on energy balance, was used to determine the major processing parameters such as laser power, transverse speed or deposition layer thickness. Fabrication of circular extrusion dies using the computed parameters yielded satisfactorily results. SEM showed few defects in the sectioned die. Laboratory aluminum extrusion tests showed that dies were strong enough to withstand heavy load, and also indicated the need for post processing of these dies for better shapes.

A 3-D analytical model based on moving Gaussian beam source was used to predict the temperature fields of H13 powder deposition, and further to determine the nominal

dimensions of molten pool. At a laser power of 500 W, the computed temperature was up to 2700 °C, and maximal width of pool was 2.0 mm, and depth at beam center was 0.13 mm. This computation data also helped to decide an offset (overlapping) for LBFF. Computed results were in agreement with experimental data. Also at this power, the cooling rate was estimated in the order of 10^4 K/s. Surface thermal gradients of circular beam and shaped beam with details on beam profiles were simulated by means of ANSYS to understand the mechanism behind using these beams for part building. The non-linear simulation results disclosed that, for the identical energy density and interaction time, shaped beam produced more uniformly distributed thermal gradient profiles than circular beam. The absolute value of thermal gradient from shaped beam was smaller than that from circular beam.

EDX analysis showed gradual changes in elemental composition at the interfaces for the FGM insert. Microhardness profiles followed the EDX observations at the interfaces, suggesting that designed structures can be produced by control of the parameters.

Future work could include an accelerated test on functionally graded inserts for corrosion resistance in static aluminum alloy melt or a thermal fatigue test by alternatively immersing test sample into molten aluminum and water. Immersion of the insert in melts results in dissolution. Weight loss per unit area can be used as evaluation criteria for this test. Thermal fatigue can be justified by the inception of cracks resulted from cycling loads. The deposition of nano-powder by means of LBFF is an area of great interest. Experimental study on this topic may help to explain how laser coating with nano-sized TiC enhanced corrosion and erosion resistance while lowering the microhardness.

APPENDIX A. POWDER DELIVERY SYSTEM DESIGN AND POWDER DELIVERY RATE CALIBRATION

Design of powder delivery system

Power delivery system is critical to the success of building parts from laser-based flexible fabrication method. The goal of designing such a system is to transport required amount of powders continuously and uniformly to the laser-created molten area. The challenge comes from the powder sizes and irregular shapes of powder particles that make powder delivery very difficult even with the assistance of excited vibration. Task of powder delivery becomes even tougher with the powder sizes scaled down to nano-scale because 1) nano-sized particles have much higher ratio of surface-to-volume than micro-sized particles, and 2) nano-sized powders' atomic force are comparable to the mass of individual particles. These sharp changes of physical and dynamic properties further impact the balances among the criteria governing particle movement as they are among micro-sized particles. For example, adhesion force plays much more important role in nano-sized powders than it does with micro powders. Given traditional gas powder delivery practice, a system with a venturi was designed (Figure A.1). Pressure gas (argon, helium or nitrogen) is the driving force to move powder particles from venturi to an intended spot. As shown in Figure A.1, powders are driven down from the hopper by gravity, and are collected by " recesses" evenly distributed around the rotator of a metalmeter. The collected powders are dumped to the outlet side as the rotator runs at a preset speed, which is linearly proportional to the powder mass delivery rate. When pressure gas passes through the venturi, it sucks in the powders and delivers them along the path. Tests have shown this powder delivery setup works well for micro-sized powders.

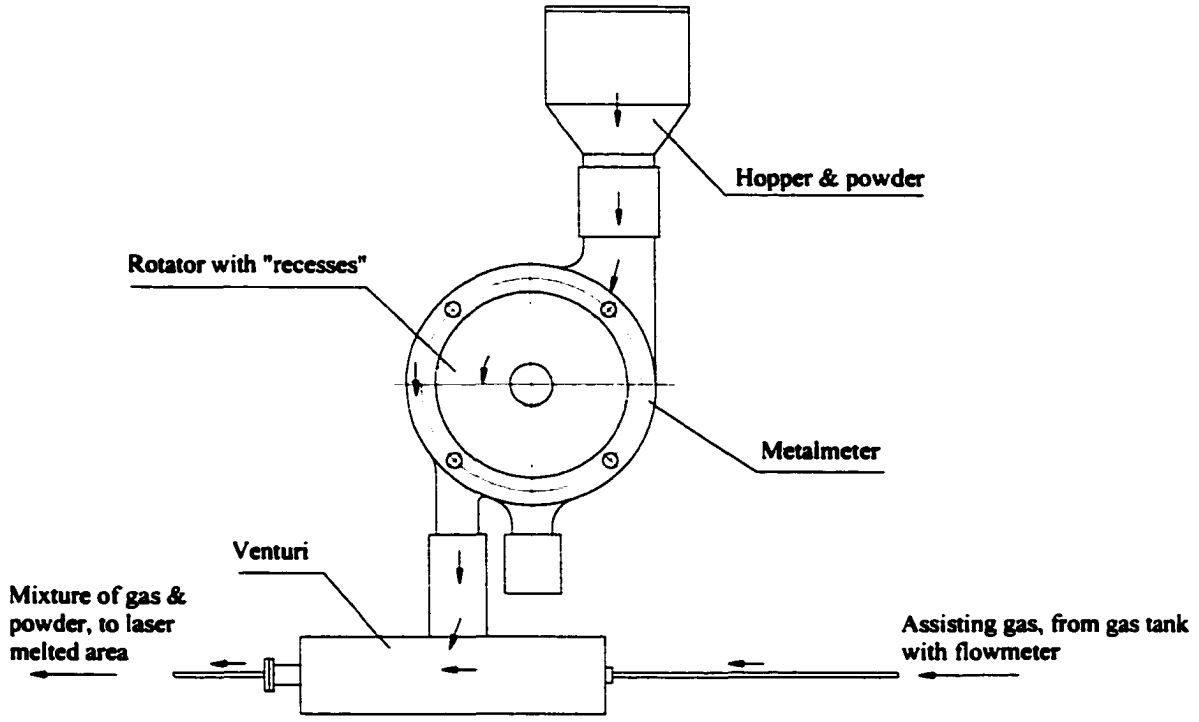

Figure A.1. A schematic showing the design of powder delivery system for laser-based flexible fabrication process

Calibration of powder delivery rate

Powder delivery rate, Q, is defined as the total mass passing across a controlled section in unit time. It is usually represented by grams per minute or per second. Quantitative control of the powder delivered to a laser-melted zone is of great importance to ensure quality. Calibration is an effective way to check the uniformity of powder delivery. A block diagram for powder quantification is shown in Figure A.2. A capped glass vessel was used to collect powder. A stopwatch with an accuracy of 1/100 second was used to measure time, t,

and a scale with an accuracy of 1/1000 gram to quantify the mass of powder, m, corresponding to the time Δt. At a setting (pressure or flowrate) for assisting gas, adjustment on the reading of metalmeter changes the revolution speed of the rotator, and further the powder delivery rate. Powder calibration was performed in such a way that at a pressure setting for assisting gas, at least four to five points were measured to get the relationship between readings of metalmeter and powder delivery rate. To ensure accuracy, three measurements were made for each point.

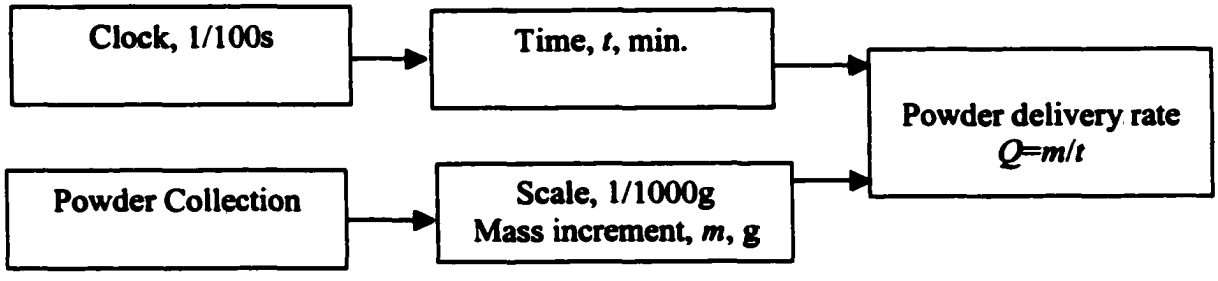

Figure A.2. A block diagram of powder calibration

The calibrated results for powders of H13 and Ni/Cr alloy are showed in Figure A.3 and A.4, respectively. Good linearity was obtained for the most often used readings ranging from 5 to 13 in the powder delivery system for the two powders. An inconsistency between the slopes for these two powders, however, were observed, which can be explained by the differences in powder particle dimensions and shapes. Interestingly, recursive calibrations executed beyond readings 13 gave results of significant discrepancy (Figure A.5). This discrepancy may result from the number of recesses and assist gas pressure settings.

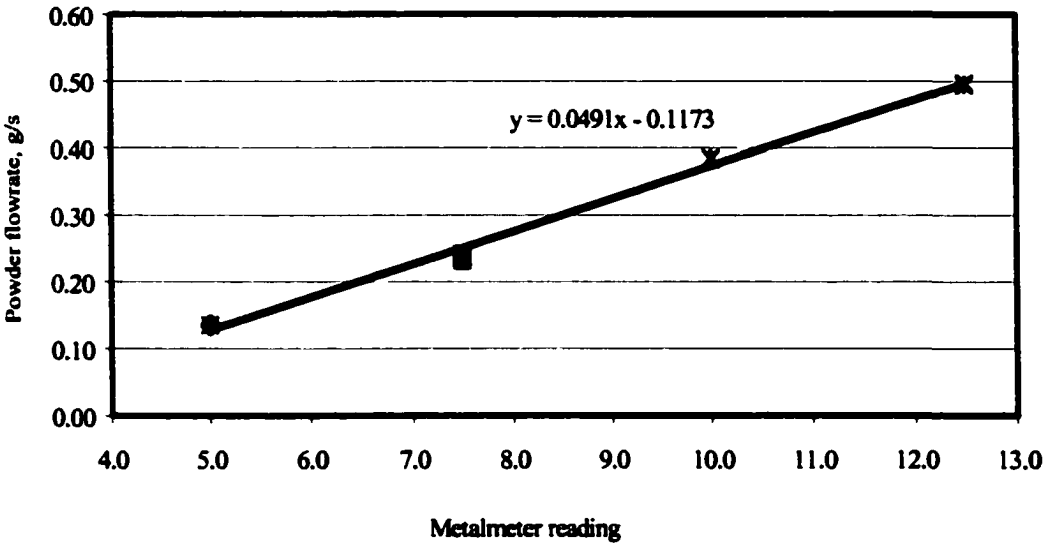

Figure A.3. Calibrated results of H13 powder (Powder size: 70~100 μm; shape: spherical; assisting gas, argon, at flowrate of 10 CFH)

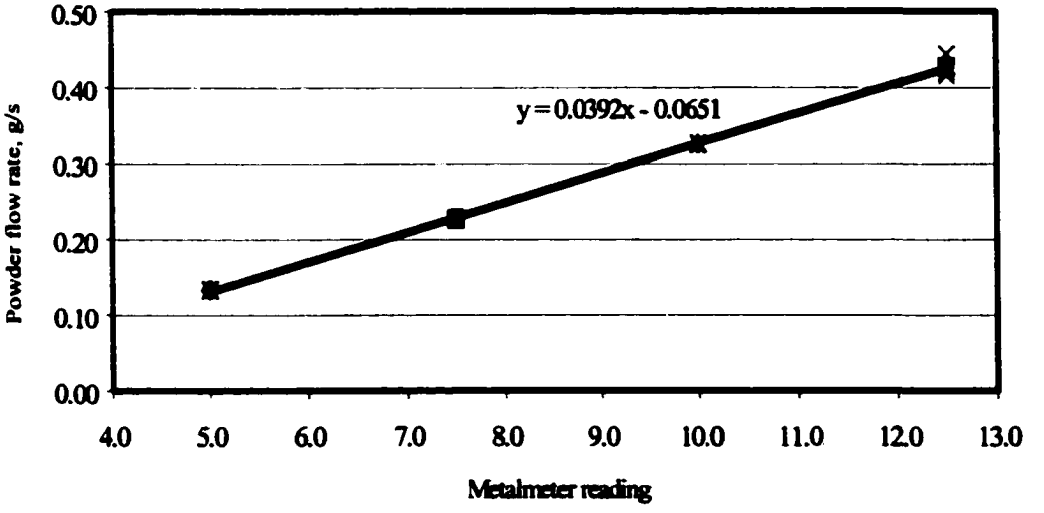

Figure A.4. Calibrated results of Ni/Cr alloy powder (Powder size: 100 μm; shape: spherical; assisting gas, argon, at flowrate of 10CFH)

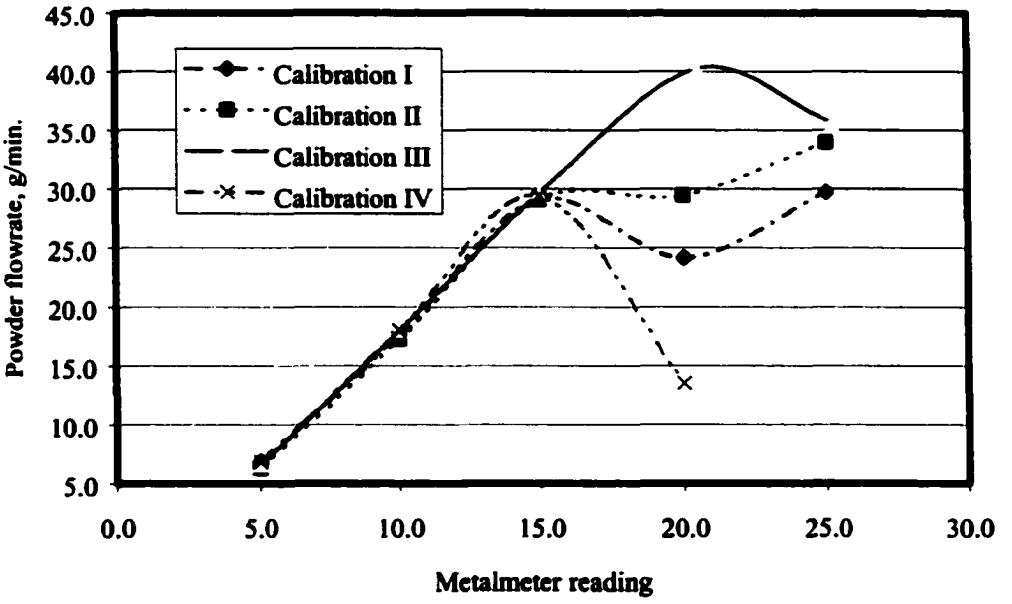

Figure A.5. Calibrated result inconsistency of Ni/Cr alloy powder beyond reading 13 (Assist gas, argon, at flowrate of 10CFH)

The total uncertainty of powder delivery rate at a 95% confidence level can be estimated as less than 2.5% by use of theory of uncertainty propagation, with both bias and precision errors considered. Take H13 powder calibration corresponding to readings of 7.5 for an example, the estimation of uncertainty based on single-sample is summarized as follows.

The powder mass, m, is measured with a scale. Bias uncertainty depends on the scale calibration, and also to some degree on the magnitude of the mass measured relative the scale range. For this scenario, an uncertainty of ±0.5% is justified, with a confidence of 95%. Precision uncertainty in mass measurement is obtained by reading error in the scale and the other factors, and taken as ±0.1%.

The time, t, is measured with a stopwatch. Synchronization between the powder delivery and watch actions will be the main uncertainty, which is essentially precision error. If time standard deviation is simply estimated as ±2s, and a total time period of 200s will be measured, then the standard deviation is ±1%. The bias error can be assumed to be negligible.

Applying the uncertainty propagation theory, we have:

$$\frac{u_Q}{Q} = \left[\left(\frac{u_m}{m}\right)^2 + \left(\frac{u_t}{t}\right)^2\right]^{1/2} \qquad \text{(A.1)}$$

The bias uncertainty is estimated as:

$$\frac{B_Q}{Q} = \left[\left(\frac{B_m}{m}\right)^2 + \left(\frac{B_t}{t}\right)^2\right]^{1/2} = \left[(0.5)^2 + (0)^2\right]^{1/2} = 0.50\% \text{ (at confidence of 95\%)}$$

Likewise, the standard deviation of Q is

$$\frac{\sigma_Q}{Q} = \left[\left(\frac{\sigma_m}{m}\right)^2 + \left(\frac{\sigma_t}{t}\right)^2\right]^{1/2} = \left[(0.1)^2 + (1)^2\right]^{1/2} = 1.00\%$$

The estimate for the single-sample precision uncertainty in Q is

$$\frac{P_Q}{Q} = \frac{1.96\sigma_Q}{Q} = 1.96(0.01) = 1.96\% \text{ (at confidence of 95\%)}$$

So the total uncertainty in Q is

$$\frac{U_Q}{Q} = \left[\left(\frac{B_Q}{Q}\right)^2 + \left(\frac{P_Q}{Q}\right)^2\right]^{1/2} = \left[(0.005)^2 + (0.0196)^2\right]^{1/2} = 2.02\% \text{ (at confidence of 95\%).}$$

APPENDIX B. CONNECTION BLOCKS FOR INJECTION MOLDING

Injection molding in this study was designed to test the functionality of dies and molds fabricated by means of LBFF. If properly executed, it could also be an efficient method to test the wear resistance of dies and molds under practical operating conditions. A 30M-BOY injection molding machines was used for these purposes. Because the die and mold blocks produced by LBFF were basically cores or inserts, connection blocks were designed to ensure these experiments. As shown in Figure B.1, rear block was configured with three pockets to hold mold inserts or cores. The rear block design allowed to test the deformation of mold inserts being subject to injection pressure.

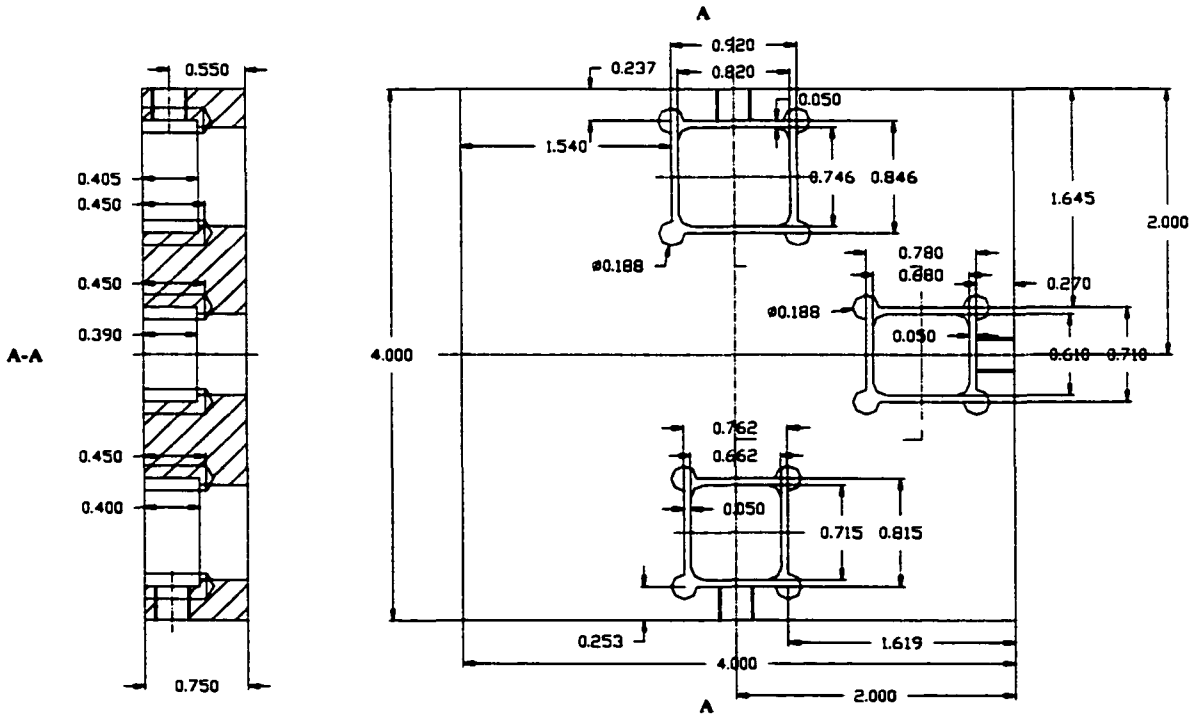

Figure B.1. Design of rear block allowing test of deformation under injection pressure

Front block (Figure B.2) had a T-shaped runner connecting to three sprue holes, respectively. The runner was so deigned that an equal distance was achieved from individual pocket to injection hole, to negate the effect of pressure drop difference along distance when wear resistance are performed.

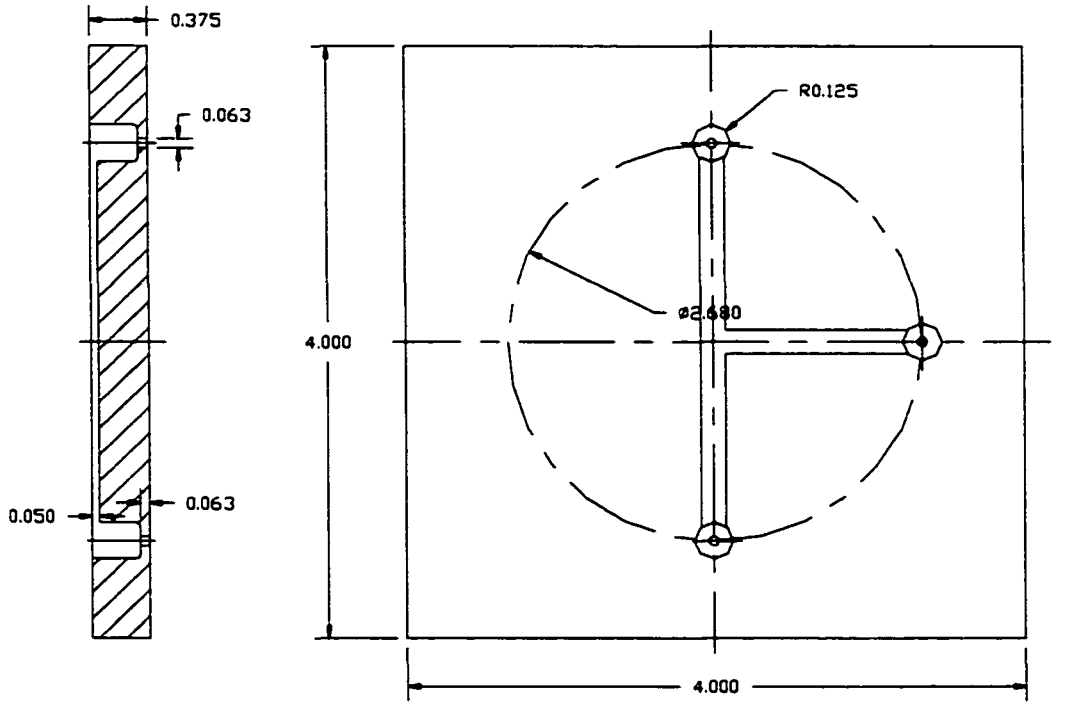

Figure B.2. Design of front block showing T-shaped runner used in injection molding test

APPENDIX C. TEMPERATURE DISTRIBUTION AND MOLTEN POOL SIZE IN LASER CLADDING USING A POINT SOURCE HEAT TRANSFER MODEL

LBFF process involves laser melting of powder materials, so heat transfer is an issue of dominance in this process. Heat flow for a rapidly moving laser source is often modeled by heat conduction [1], although convection and radiation also affect laser material processing, to some degree. Lumped heat capacity model based on heat balance has been successfully used to estimate laser power required or average temperature created in a defined process. However, this simplified model could not provide temperature distribution details around the beam. The temperature distribution is necessary to compute nominal dimensions of molten pool and thermal gradient, G. Therefore, models other than lumped heat balance have to be used. Since LC-based SFF is usually conducted at much lower scanning speeds than laser cutting and melting, the convection effect on the heat transfer process is negligible. In addition, the following assumptions were made: 1) laser beam is a point source with Gaussian energy distribution; 2) pre-placed powder layer has uniform thickness; 3) latent heat of melting is neglected; 4) heat losses due to radiation are not considered; and 5) physical properties of the material are independent of temperature.

The temperature field, $T(X,Y,Z)$, from a moving beam in a system of pre-placed powder and solid substrate material can be calculated by superposition of discrete Gaussian sources over a semi-infinite solid [1]:

$$T(X,Y,Z) = T_a + \frac{\alpha P}{kR}\int_0^{\infty} \frac{\exp(-H)}{(2\pi^3)^{1/2}(1+\mu^2)} d\mu \qquad \text{(C.1)}$$

with function

$$H(\mu) = \frac{(X + \psi\mu^2/2) + Y^2}{2(1+\mu^2)} + \frac{Z^2}{2\mu^2}$$

Where α is the absorption coefficient of a material; P is laser power, W; k is thermal conductivity, W/(cm.K); R is the radius of beam; ψ is a dimensionless variable with expression $\psi = RV/D$; V is beam scanning speed, cm/sec; D is thermal diffusivity, cm^2/sec; μ is a dimensionless integral variable with expression $\mu^2 = 2Dt/R^2$; t is time, sec; and X, Y, and Z are dimensionless coordinates. Thermal gradients can then be computed by deriving $T(X,Y,Z)$ with respect to X, Y, and Z, respectively.

An internal function based on high order recursive adaptive quadrature in MATLAB was used, and program codes were also made in MATLAB to get the integrals in equation (C.1). Assuming molten pool as circular in shape, the maximum diameter (width) and depth cab be estimated by mapping the temperature field with melting temperature/range of alloy (in this case H13 was used for calculations). With coordinate system fixed, the temperature variations along X and Z were computed from equation (C.1). Figure C.1 (A) shows that the temperature distribution from a moving laser source is asymmetric with respect to X due to the superposition of discrete Gaussian sources. This type of asymmetry is propagated from the top surface to inside the material, with temperature peak shifting further backward. The back-shifted peak re-heats the solidified material and may lead to phase transformations and grain growth in the heat-affected zone. This transformation may not be desired because it could produce a certain portion of retained austenite, which affects not only hardness and dimensional stability, but also wear behavior and occurrence of crack initiation in the post-processing such as grinding and electrospark machining [2]. The maximum width in X

direction was estimated to be 2.0 mm, which was about 10~20% larger than the width of measured single track. The simplifications made on this analytical model are attributed to the dimensional difference.

Temperature variation with the depth of material was also computed (Figure C.1 (B)). An exponential profile was obtained, which has been verified experimentally [3]. Melt layer depth is estimated as 0.128 mm (0.005 in.), which was within the normal range of deposition thickness. Dilution can now be estimated with a known thickness of pre-placed layer.

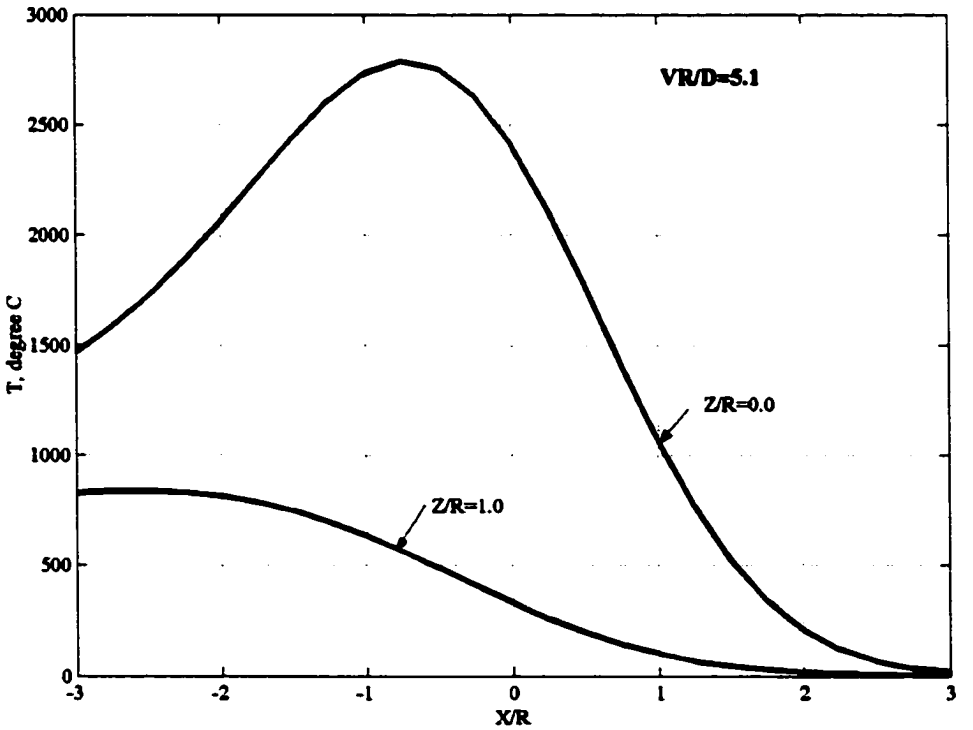

(A)

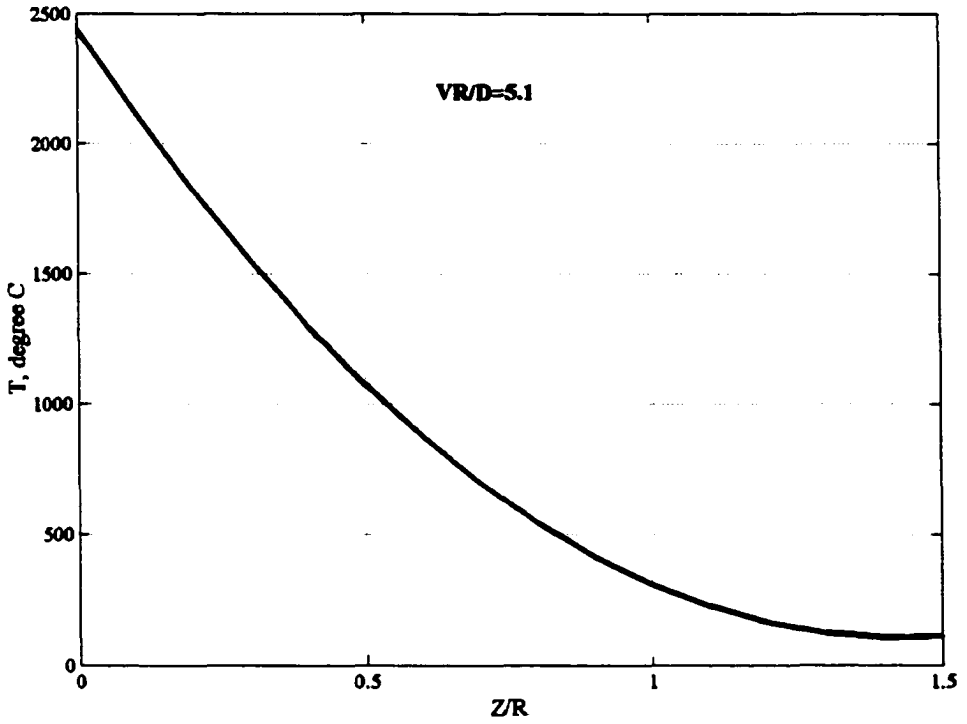

Figure C.1. Temperature distribution: (A) along beam moving direction, X, at different depths, Z/R; (B) along material depth, Z/R, at X/R= 0.0 (pre-placed H13 powder on H13 substrate; laser power P=500 W; scanning speed V= 8.5 cm/s; C_p=3.6 J/(cm^3.°C); D=0.007 cm^2/s)

Further computations based on this model provide thermal gradients. Cooling rate is related to thermal gradient by laser beam moving velocity, V. The cooling rate in this case was computed in the order of 10^4 K/s, which is approximate to result from ANSYS model. Variations of cooling along beam moving direction, X, is illustrated in Figure C.2. It shows a similarity to the temperature distribution profile.

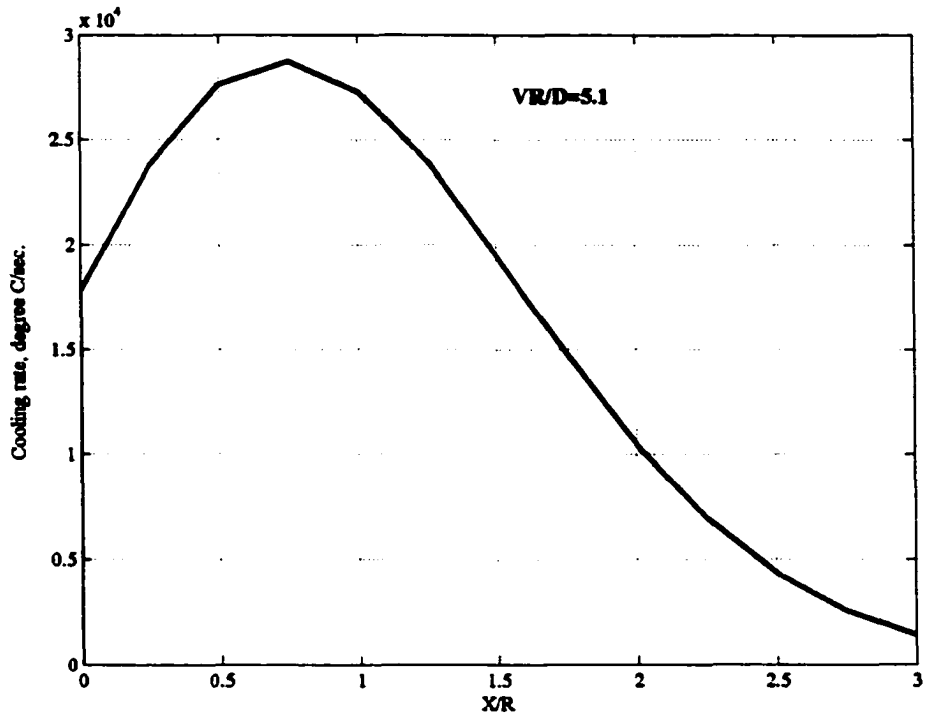

Figure C.2. Cooling rate variation along beam moving direction, X (pre-placed H13 powder on H13 substrate; laser power P=500 W; scanning speed V= 8.5 cm/s; C_p=3.6 J/(cm^3.°C); D=0.007 cm^2/s)

REFERENCES

1. Cline, H.E., and Anthony, T.R., 1977, "Heat Treating and Melting Material with a Scanning Laser or Electron Beam," Journal of Applied Physics, 48, No.9, pp. 3895-3900.
2. Vilar, Rui, 2001, "Laser Cladding," The international Journal of Powder Metallurgy, 37, No. 2, pp. 31-47.
3. Lowry, J.F., Fink, J.H., and Schumacher, B.W., 1976, "Major Advance in High-Power Electron-Beam Welding in Air," Journal of Applied Physics, 47, No. 1, pp. 95-106.